Katrin Unger, BSc

Distributed Bragg Reflectors: Morphology of Cellulose Acetate, Polystyrene and Polyvinylcarbazol Multilayers

MASTER THESIS

For obtaining the academic degree
Diplom-Ingenieurin

Master Programme of
Technical Physics

Graz University of Technology

Supervisor:
Ao.Univ.-Prof. Dipl.-Ing. Dr.techn. Roland Resel
Institute of Solid State Physics

Graz, June 2014

EIDESSTATTLICHE ERKLÄRUNG

AFFIDAVIT

Ich erkläre an Eides statt, dass ich die vorliegende Arbeit selbstständig verfasst, andere als die angegebenen Quellen/Hilfsmittel nicht benutzt, und die den benutzten Quellen wörtlich und inhaltlich entnommenen Stellen als solche kenntlich gemacht habe. Das in TUGRAZonline hochgeladene Textdokument ist mit der vorliegenden Masterarbeit identisch.

I declare that I have authored this thesis independently, that I have not used other than the declared sources/resources, and that I have explicitly indicated all material which has been quoted either literally or by content from the sources used. The text document uploaded to TUGRAZonline is identical to the present master's thesis.

Datum / Date

Unterschrift / Signature

Abstract

The optical quality and photonic properties of all-polymer distributed Bragg reflectors are related to the morphology of the layers and the optical responses of the materials. A combined technique of X-ray reflectivity, atomic force microscopy and spectroscopic ellipsometry was used to characterize the thickness, the interface roughness, the surface roughness and the refractive indices. The layers were made of cellulose acetate, polystyrene and polyvinylcarbazol, which are polymers often used in the domain of spin casted multilayer systems. The shrinkage and the change of interface roughness of cellulose acetate and polystyrene layers were investigated up to temperatures of 200 °C. Up to 170 °C the interface roughness stays constant at about 1 nm while it increases up to 2 nm at 200 °C. The thickness of the polystyrene layer remains constant up to 170 °C, well above its glass transition temperature T_g. For cellulose acetate a monotonic decrease is observed with increasing temperature. It could be shown, that the change in the optical response of a thermally treated distributed Bragg reflector is related to the change of the layer thickness of cellulose acetate. Spectra of $(PS\text{-}CA)_{20}PS$ distributed Bragg reflectors and $(PS\text{-}CA)_{10}P3HT(PS\text{-}CA)_{10}$ cavities are in a good agreement with simulated spectra with parameters obtained from of the X-ray reflectivity measurements. A simulation, which considers a monotone increase of thickness improves the conformance to the experiment rather than a simulation with a Gaussian distributed random thickness variation.

Kurzfassung

Die Qualität von Bragg Spiegeln hängt von der Beschaffenheit der Schichten, sowie der optischen Eigenschaften der Materialien ab. Zur Charakterisierung der Schichtdicke, der Oberflächen- und Grenzflächen-Rauheit sowie des Brechungsindex wurden die Methoden der Röntgenreflektivität, der Rasterkraftmikroskopie und der spektroskopischen Ellipsometrie kombiniert. Die untersuchten Mehrfachschichtsysteme sind mittels Rotationsbeschichtung aufgetragene Polymere aus Celluloseacetat, Polystyrol und Polyvinylcarbazol. Die Änderung der Schichtdicke und der Grenzflächenrauheit wurden bis zu einer Temperaturbehandlung von 200 °C evaluiert. Die Grenzflächenrauheit ist bis zu 170 °C konstant auf 1 nm und steigt von 170 °C bis 200 °C auf 2 nm. Die Schichtdicke von Polystyrol ist konstant bis 170 °C was sich weit über der Glasübergangstemperatur von Polystyrol befindet. Die Schichtdicke von Celluloseacetat zeigt einen konstanten Abfall mit steigender Temperatur. Es konnte gezeigt werden, dass die Änderung der optischen Antwort eines temperaturbehandelten Bragg Spiegels auf die Verschmälerung der Celluloseacetat Schicht zurückzuführen ist. Spektren von $(\text{PS-CA})_{20}\text{PS}$ Bragg Spiegeln und $(\text{PS-CA})_{10}\text{P3HT}(\text{PS-CA})_{10}$ Resonatoren können ausgezeichnet mit simulierten Spektren, die auf den Röntgenreflektivitätsmesswerten basieren, abgebildet werden. Eine Simulation, die einen monotonen Anstieg der Schichtdicke berücksichtigt, gleicht einem experimentell aufgenommenen Spektrum besser, als eine Simulation, die eine gaußverteilte zufällige Schichtdicke annimmt.

Acknowledgment

I am very thankful for my supervisor Roland Resel. With his knowledge and expertise he guided me through my thesis with advice and patience. He supported me and gave me plenty of opportunities to work at different research facilities. I was honored to take part in a synchrotron experiment at the ESRF in Grenoble.

It was a great experience for me to learn under the guidance of Davide Comoretto of the University in Genoa the preparation of distributed Bragg reflectors. In his laboratory group, I want to thank Serena Gazzo for helping me in the chemical laboratory and Ginacarlo Canazza for providing me with the single and double layer samples. I gladly appreciate the collaboration with Caterina Czibula, Christian Ganser and Christian Teichert of the University of Leoben for providing the atomic force microscopy images. It was a pleasure for me to work on spectroscopic ellipsometry under the direction of Georg Jakopic of the Joanneum Research in Weiz.

I am very glad to work in the *k-room* with my colleagues Reinhold Hetzel, Michael Zawodzki, Stefan Pachmajer, Christian Röthel, Michael Pachler and Andrew Jones. We shared enthusiasm to science, a lot of thoughts and we had plenty of fun.

I cordial thank my parents, Ruth and Erwin, my siblings, Lisa and Martin, and my friends, especially Maksida and Eva, for supporting and helping me. Finally, I would like to give special gratitude to my soul-mate Peter Luidolt. You give me courage, love and trust. Life would be so less fun without you.

Contents

1. Motivation

In the year 1887 Lord Rayleigh experimented with stacks of periodic multi-layer dielectric material that had layer thickness within the dimension of the wavelength of visible light [1]. He was the first who measured a photonic bandgap of an one dimensional photonic crystal. 100 years later, in 1987, the pioneer works of E. Yablonovitch and S. John lead to a break through in the domain of three dimensional photonic crystals [2, 3]. The idea of inhibition of spontaneous emission and to mold the flow of light within three dimensional periodic dielectric material is still a research field of huge interests with promising applications [4–6].

Semiconducting and oxide layers have been investigated for over 30 years in optical devices [7]. Although the buildup is simple, the production is time consuming and expensive. The use of organic polymers is an attractive alternative. Polymers offer plenty of feasible mechanical and optical properties. Optical devices have already been demonstrated as responsive sensors [8], in light emitting diodes [9], as distributed Bragg reflectors [10], as distributed feedback lasers [11], as self-assembled block-copolymers [12] and as opals [5, 13]. The manufacturing techniques include ion beam sputtering [14], two photon-initiated polymerization [15], co-extrusion [16] and the already mentioned self-assembling of polymers. The main disadvantages of these methods are a limitation to specific polymers and high process costs. Another way to produce such devices is to deposit the polymers alternating one at a time with dynamical spin casting [17, 18]. Systems of up to 50 layers can be achieved in an easy and fast way. The disadvantages of spin casting is a limitation to one dimensional photonic crystals and the loss in the knowledge of layer thickness and morphology properties. Despite those disadvantages it is possible to reproduce optical devices with the same properties.

Thin film thicknesses can be commonly determined by interferometry, using two waveguide branches [19], or by spectroscopic ellipsometry [20]. It has been tested, that the spin coated samples do not provide sufficient thickness profile for the interferometry method. Spectroscopic ellipsometry data are not easy to fit if the materials are optical active. In this study X-ray reflectivity will be used to investigate the thin film thickness, the surface

roughness and the interface roughness of polymer layers in the domain of optical devices. The results will be compared to spectroscopic ellipsometry and mathematical simulations to verify the quality of X-ray reflectivity method.

2. Fundamentals of One Dimensional Photonic Crystals

2.1. Electromagnetic Waves in Dielectric Materials

Photonic crystals are materials with a periodicity in the dielectric function. The materials used in this study do not carry unpaired charges, have no currents, no magnetization and will be assumed to have no absorption. To investigate the behavior of electromagnetic waves in this kind of material we start with the Maxwell equations:

$$\nabla \cdot \mathbf{D} = 0 \tag{2.1}$$

$$\nabla \cdot \mathbf{B} = 0 \tag{2.2}$$

$$\nabla \times \mathbf{H} = \frac{\partial D}{\partial t} \tag{2.3}$$

$$\nabla \times \mathbf{E} = -\frac{\partial B}{\partial t} \tag{2.4}$$

The relations of the fields in vacuum and in non magnetic materials are:

$$\mathbf{H} = \frac{1}{\mu_0}\mathbf{B} \tag{2.5}$$

$$\mathbf{D} = \epsilon_0 \epsilon(\mathbf{r})\mathbf{E} \tag{2.6}$$

Because of the linearity of the Maxwell equation and the periodicity of the dielectric function, solutions for the fields are of the form of harmonic modes in time:

$$\mathbf{E}(\mathbf{r}, t) = \mathbf{E}(\mathbf{r})e^{-i\omega t} \tag{2.7}$$

$$\mathbf{H}(\mathbf{r}, t) = \mathbf{H}(\mathbf{r})e^{-i\omega t} \tag{2.8}$$

Substitute the harmonic modes into equation 2.3 and equation 2.4 two sets of equations can be derived:

$$\omega^2 \mathbf{E} = \frac{1}{\epsilon(r)} \nabla \times (\nabla \times) \, \mathbf{E} \tag{2.9}$$

$$\nabla \cdot \epsilon(r) \cdot \mathbf{E} = 0 \tag{2.10}$$

$$\omega^2 \mathbf{H} = \overbrace{\nabla \times \left(\frac{1}{\epsilon(\mathbf{r})} \nabla \times \right)}^{\hat{\mathrm{H}}} \mathbf{H} \tag{2.11}$$

$$\nabla \cdot \mathbf{H} = 0 \tag{2.12}$$

The eigenvalue equation 2.11, also called master equation, has many useful orthogonality properties and is therefore easier to solve than equation 2.9. The operator $\hat{\mathrm{H}}$ is called electromagnetic Hamiltonian. The **E**- and the **H**-field can be derived by:

$$\mathbf{E} = \frac{i}{\omega \epsilon(r)} \nabla \times \mathbf{H} \tag{2.13}$$

$$\mathbf{H} = -\frac{i}{\omega} \nabla \times \mathbf{E} \tag{2.14}$$

2.2. Layered Materials

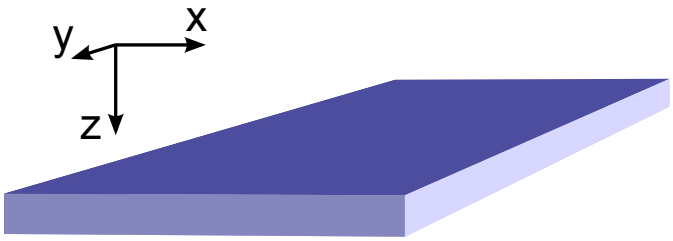

Figure 2.1.: Definition of directions in layered material.

The master equation 2.11 is not easy to solve but for materials with a periodic dielectric function the Bloch theorem can be applied [21]. In similar manner than to calculate the eigenstates of electrons in a periodic potential, we start with looking for an operator that commutes with the dielectric Hamiltonian $\hat{\mathrm{H}}$ of equation 2.11. The operator of translation is defined as:

$$\hat{\mathrm{T}}_{\mathbf{r}'} \mathbf{H}(\mathbf{r}) = \mathbf{H}(\mathbf{r} - \mathbf{r}') \tag{2.15}$$

Layered materials have a continuous periodicity in xy-plane of the layer, figure 2.1. The dielectric function is just dependent in the direction normal to the plane $\epsilon(\mathbf{r}) = \epsilon(\mathrm{z})$. A translation of the dielectric function in xy-plane has no influence: $\hat{\mathrm{T}}_{\mathbf{r}_{\mathrm{xy}}}\epsilon(\mathrm{z}) = \epsilon(\mathrm{z})$. The translation operator $\hat{\mathrm{T}}_{\mathbf{r}_{\mathrm{xy}}}$ commutes with the electromagnetic Hamiltonian $\hat{\mathrm{H}}$, equation 2.11. They share the same set of eigenstates.

$$\left[\hat{\mathrm{H}}, \hat{\mathrm{T}}_{\mathbf{r}_{\mathrm{xy}}}\right] = 0 \tag{2.16}$$

The square of the absolute value of the **H**-field has to stay constant with translation [22, p. 22].

$$|\mathbf{H}(\mathbf{r})|^2 \stackrel{!}{=} |\mathbf{H}(\mathbf{r} + \mathbf{r}_{\mathrm{xy}})|^2 \tag{2.17}$$

$\mathbf{H}(\mathbf{r})$ and $\mathbf{H}(\mathbf{r} + \mathbf{r}_{\mathrm{xy}})$ just differ in a phase factor.

$$\mathbf{H}(\mathbf{r} + \mathbf{r}_{\mathrm{xy}}) = \alpha(\mathbf{r}_{\mathrm{xy}})\mathbf{H}(\mathbf{r}) \tag{2.18}$$

$$|\alpha(\mathbf{r}_{\mathrm{xy}})|^2 = 1 \tag{2.19}$$

Additional, the phase factor should fulfill following condition:

$$\mathbf{H}(\mathbf{r} + \mathbf{r}_{\mathrm{xy}} + \mathbf{r}'_{\mathrm{xy}}) = \alpha(\mathbf{r}_{\mathrm{xy}} + \mathbf{r}'_{\mathrm{xy}})\mathbf{H}(\mathbf{r}) = \alpha(\mathbf{r}_{\mathrm{xy}})\alpha(\mathbf{r}'_{\mathrm{xy}})\mathbf{H}(\mathbf{r}) \tag{2.20}$$

$$\alpha(\mathbf{r}_{\mathrm{xy}} + \mathbf{r}'_{\mathrm{xy}}) = \alpha(\mathbf{r}_{\mathrm{xy}})\alpha(\mathbf{r}'_{\mathrm{xy}}) \tag{2.21}$$

The ansatz $\alpha(\mathbf{r}_{\mathrm{xy}}) = e^{i\mathbf{k}\mathbf{r}_{\mathrm{xy}}}$ confirms with equation 2.19 and 2.21 and is indeed an eigenstate of the translation operator. A general form of a solution for **H** is therefore:

$$\mathbf{H}_{\mathbf{k}_{\mathrm{xy}}}(\mathbf{r}) = e^{i\mathbf{k}_{\mathrm{xy}}\mathbf{r}}\mathbf{U}_{\mathrm{k}_{\mathrm{xy}}}(z) \tag{2.22}$$

2.3. Transfer Matrix Method

In this section the transfer matrix method will be introduced. A mathematical description of light propagation through an interface will be represented as a matrix. And a propagation through layered material will be therefore a matrix multiplication of several transfer matrices. The method presented, was taken out of the book *Fundamentals of Photonic Crystal Guiding* by M. Skorobogatiy and J. Yang [23]. The method was already been tested in several publication for example by M. Kolle et al. [24]. The general form of the

electromagnetic fields in dielectric non absorbing layer with $\mathbf{k}_{xy}$=k_x is:

$$\mathbf{H}_{\mathbf{k}_x}(\mathbf{r}) = e^{i\mathbf{k}_x x}\mathbf{U}^H_{\mathbf{k}_x}(z) \tag{2.23}$$

$$\mathbf{E}_{\mathbf{k}_x}(\mathbf{r}) = e^{i\mathbf{k}_x x}\mathbf{U}^E_{\mathbf{k}_x}(z) \tag{2.24}$$

We need to separate the light into a vertical to the surface polarized part and a parallel to the surface polarized part, illustrated in figure 2.2. The vertical part is literately known as transverse electric (TE) component. The parallel part is known as transverse magnetic (TM) component.

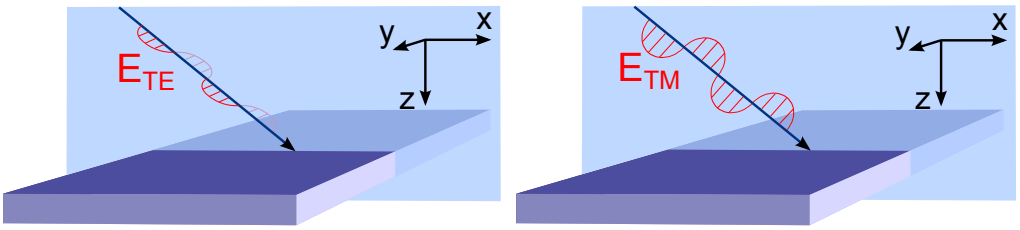

Figure 2.2.: TE: The **E**-field is parallel to the surface and points out of the (x,z)-plane. TM: **E**-field is in (x,z)-plane and the **H**-field points out of the (x,z)-plane.

2.3.1. Transverse Electric Polarization

In each layer the electric field can be described as two planar waves. One in forward direction and one in backward direction of propagation. A_j and B_j are the expansion coefficients of the electric fields, within the jth layer.

$$\mathbf{E}^j_y(x,y,z) = e^{ik_x x}\left(A_j e^{ik^j_z(z-z_j)} + B_j e^{-ik^j_z(z-z_j)}\right) \tag{2.25}$$

The magnetic field **H** is via equation 2.14 related to the electric field **E**.

$$\mathbf{H}^j_x(x,y,z) = -e^{ik_x x}\frac{k^j_z}{\omega}\left(A_j e^{ik^j_z(z-z_j)} - B_j e^{-ik^j_z(z-z_j)}\right) \tag{2.26}$$

$$\mathbf{H}^j_z(x,y,z) = e^{ik_x x}\frac{k^j_z}{\omega}\left(A_j e^{ik^j_z(z-z_j)} + B_j e^{-ik^j_z(z-z_j)}\right) \tag{2.27}$$

At the interface of one layer to another, the horizontal component of the electric field and the vertical component of the magnetic field have to be continuous.

$$\mathbf{E}_y^{j-1}(x,y,z) = \mathbf{E}_y^{j}(x,y,z) \tag{2.28}$$

$$\mathbf{H}_x^{j-1}(x,y,z) = \mathbf{H}_x^{j}(x,y,z) \tag{2.29}$$

These boundary conditions lead to following matrix equation with $M_{j-1,j}$ the so called transfer matrix.

$$M_{j-1,j} \begin{pmatrix} A_{j-1} \\ B_{j-1} \end{pmatrix} = \begin{pmatrix} A_j \\ B_j \end{pmatrix} \tag{2.30}$$

$$M_{j-1,j} = \frac{1}{2} \begin{pmatrix} \left(1 + \frac{k_z^{j-1}}{k_z^j}\right) e^{ik_z^{j-1} d_{j-1}} & \left(1 - \frac{k_z^{j-1}}{k_z^j}\right) e^{-ik_z^{j-1} d_{j-1}} \\ \left(1 - \frac{k_z^{j-1}}{k_z^j}\right) e^{ik_z^{j-1} d_{j-1}} & \left(1 + \frac{k_z^{j-1}}{k_z^j}\right) e^{-ik_z^{j-1} d_{j-1}} \end{pmatrix} \tag{2.31}$$

With the transfer matrix above, we can calculate the change of the expansion coefficients A_j and B_j of the transverse electric component from one layer to another.

2.3.2. Transverse Magnetic Polarization

We start with the same approach, but now A_j and B_j are the expansion coefficients of the magnetic field.

$$\mathbf{H}_y^j(x,y,z) = e^{ik_x x} \left(A_j e^{ik_z^j (z - z_j)} + B_j e^{-ik_z^j (z - z_j)} \right) \tag{2.32}$$

We use again equation 2.13 to relate the **E**-field to the **H**-field (with $k_x^2 + (k_z^j)^2 = \omega^2 \epsilon_j$).

$$\mathbf{E}_x^j(x,y,z) = -e^{ik_x x} \frac{k_z^j}{\omega \epsilon_j} \left(A_j e^{ik_z^j (z - z_j)} - B_j e^{-ik_z^j (z - z_j)} \right) \tag{2.33}$$

$$\mathbf{E}_z^j(x,y,z) = e^{ik_x x} \frac{k_z^j}{\omega \epsilon_j} \left(A_j e^{ik_z^j (z - z_j)} + B_j e^{-ik_z^j (z - z_j)} \right) \tag{2.34}$$

At the interfaces the horizontal component of the magnetic field and the vertical component of the electric field have to be continuous.

$$\mathbf{H}_y^{j-1}(x,y,z) = \mathbf{H}_y^{j}(x,y,z) \tag{2.35}$$

$$\mathbf{E}_x^{j-1}(x,y,z) = \mathbf{E}_x^{j}(x,y,z) \tag{2.36}$$

Again, we derive a transfer matrix $M_{j-1,j}$. For non magnetic materials the dielectric constant is equal to the square root of the refractive index: $\epsilon = n^2$.

$$M_{j-1,j} \begin{pmatrix} A_{j-1} \\ B_{j-1} \end{pmatrix} = \begin{pmatrix} A_j \\ B_j \end{pmatrix} \tag{2.37}$$

$$M_{j-1,j} = \frac{1}{2} \begin{pmatrix} \left(1 + \frac{k_z^{j-1}\epsilon_j}{k_z^j \epsilon_{j-1}}\right) e^{ik_z^{j-1} d_{j-1}} & \left(1 - \frac{k_z^{j-1}\epsilon_j}{k_z^j \epsilon_{j-1}}\right) e^{-ik_z^{j-1} d_{j-1}} \\ \left(1 - \frac{k_z^{j-1}\epsilon_j}{k_z^j \epsilon_{j-1}}\right) e^{ik_z^{j-1} d_{j-1}} & \left(1 + \frac{k_z^{j-1}\epsilon_j}{k_z^j \epsilon_{j-1}}\right) e^{-ik_z^{j-1} d_{j-1}} \end{pmatrix} \tag{2.38}$$

2.3.3. Reflection and Transmission of Layered Materials

So far, we derived for TM and for TE polarization a possibility to calculate the expansion coefficients for the fields while propagating through layered material by simply applying transfer matrices. The transfer matrices are dependent on k_x, k_z, d, and n. In figure 2.3 four layers on a substrate are plotted. A_0 is the incoming beam, B_0 the reflected beam and A_{N+1} is the transmitted beam. The $M_{\text{Air P1}}$ indicates the transfer matrix of the beam propagating through the interface between air and the polymer layer P1. The other transfer matrices are listed underneath and need to be multiplied in the correct order.

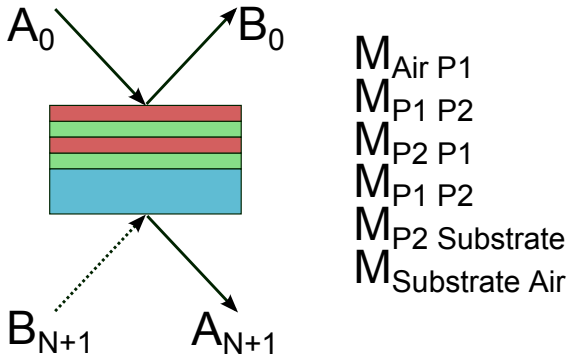

Figure 2.3.: Light propagating through layered material: A_0 is the incoming beam, B_0 the reflected beam and A_{N+1} is the transmitted beam. The transfer matrix for each interface is listed aside.

The expansion coefficient of the incoming beam is $A_0 \equiv 1$. There is no incoming beam

from the backside $\mathrm{B_{N+1}} = 0$. The equation for this setup is:

$$\begin{pmatrix} A_{N+1} \\ 0 \end{pmatrix} = M_{\mathrm{Sub,Air}} M_{\mathrm{P2,Sub}} M_{\mathrm{P1,P2}} M_{\mathrm{P2,P1}} M_{\mathrm{P1,P2}} M_{\mathrm{Air,P1}} \begin{pmatrix} 1 \\ B_0 \end{pmatrix} \tag{2.39}$$

$$\begin{pmatrix} A_{N+1} \\ 0 \end{pmatrix} = \begin{pmatrix} m_{11} & m_{12} \\ m_{21} & m_{22} \end{pmatrix} \begin{pmatrix} 1 \\ B_0 \end{pmatrix} \tag{2.40}$$

$$B_0 = -\frac{m_{21}}{m_{22}} \qquad A_{N+1} = \frac{m_{11}m_{22} - m_{12}m_{21}}{m_{22}} \tag{2.41}$$

The value $\mathrm{B_0}$ is related to the expansion coefficient of the reflected beam and A_{n+1} is related to the transmitted beam. To calculate a transmission or reflectance spectrum the parameters k_x, k_z, d, and n should be known for each layer. For each ω all the transfer matrices for each layer have to be calculated and multiplied. Than the expansion coefficient for transmission and reflection can be derived with equation 2.41. Usually the incident beam starts and finishes in air. The expansion coefficients $A_{\mathrm{n+1}}$ and B_0 are the amplitudes of the transmitted and reflected **E**-field. The intensity of the transmitted beam is $I \propto |A_{n+1}|^2$ and of the reflected beam $I \propto |B_0|^2$. Usually the incident beam is non-polarized. For the transfer matrix method, the beam need to be split into a TM and a TE polarized beam. For both polarizations the transfer matrices can be calculated and the reflection and transmission can be received. Afterward the two beams intensities have to be combined together with:

$$I_{\mathrm{Trans}} = \frac{\sqrt{(A_{\mathrm{TE}} \cdot A^*_{\mathrm{TE}})^2 + (A_{\mathrm{TM}} \cdot A^*_{\mathrm{TM}})^2}}{\sqrt{2}} \tag{2.42}$$

The reflection of a single surface can be derived with a single transfer matrix of transverse electric polarized light of equation 2.30 and transverse magnetic polarized light of equation 2.37. The components of the transfer matrix need to be plugged into equation 2.41. The results are the Fresnel coefficients (with k', the incoming wave vector and k", the transmitted wave vector):

$$B_{\mathrm{TE}} = -\frac{\left(1 + \frac{k'_z}{k''_z}\right) e^{-ik'_z d_1}}{\left(1 - \frac{k'_z}{k''_z}\right) e^{-ik'_z d_1}} = \frac{k'_z - k''_z}{k'_z + k''_z} \tag{2.43}$$

$$B_{\mathrm{TM}} = -\frac{\left(1 + \frac{k'_z \epsilon_2}{k''_z \epsilon_1}\right) e^{-ik'_z d_1}}{\left(1 - \frac{k'_z \epsilon_2}{k''_z \epsilon_1}\right) e^{-ik'_z d_1}} = \frac{k'_z \epsilon_2 - k''_z \epsilon_1}{k'_z \epsilon_1 + k''_z \epsilon_2} \tag{2.44}$$

2.4. The Infinite Periodic Multilayer

For an infinite layer stack with a periodicity in the z-direction a mathematical model for the dispersion relation for photons can be developed. The additional periodicity cause an additional eigenstate $e^{ik_z D}$ of the translation operator $\hat{T}$. The variable D is the length of the periodicity. For a system with 2 alternating layers, D is the summation of both layer thicknesses $D=d_1+d_2$. A repeat unit is defined as the layers which repetition would produce the complete stack. The dispersion relation $\omega(k)$ cannot be written in an explicit form but the inverse form is [25]:

$$k(\omega) = \pm\frac{1}{d_1+d_2} arctan\sqrt{\left(\frac{2}{\alpha}\right)^2 - 1} \tag{2.45}$$

$$\alpha = 2cos\left(\omega\frac{d_2}{c_1}\right)cos\left(\omega\frac{d_1}{c_2}\right) - \left(\frac{c_1^2+c_2^2}{c_1 c_2}\right)sin\left(\omega\frac{d_2}{c_1}\right)sin\left(\omega\frac{d_1}{c_2}\right) \tag{2.46}$$

with c_1 and c_2 the speed of light in the two media and d_1 and d_2 the two layer thicknesses. The wave vector k is real if α is smaller two. In this case the solution is wavelike and the wave with the resonance frequency ω can penetrate into the layered system. An imaginary vector k implies an exponentially damping solution for the fields. The wave gets totally reflected if α is greater than two.

In figure 2.4 the dispersion relation for three infinite repeating double layer stacks are plotted. The k-axis was scaled with the periodicity D and additional reduced to the first Brillouin zone. The parts where the **k** vector is imaginary was highlighted in red and is called bandgap. Incident electromagnetic wave within this frequency range gets reflected. The three different dispersion relations vary in the length of the periodicity and the refractive indices of the repeat unit. The density of states is plotted with the formula:

$$D(\omega) = \overbrace{D(k)}^{\frac{2}{\pi}}\frac{dk}{d\omega} \tag{2.47}$$

$$\lambda = \frac{2\pi c_0}{\omega} \tag{2.48}$$

The top and the middle dispersion relations have equal layer thicknesses but differ in the refractive index. Each layer is 150 nm thick, which gives a repeat unit of D=300 nm. The refractive index for the first layer is chosen to be n_1=1 and the second n_2=2 (top) or n_2=1.3 (middle). The top photonic dispersion relation shows broader bandgaps at lower

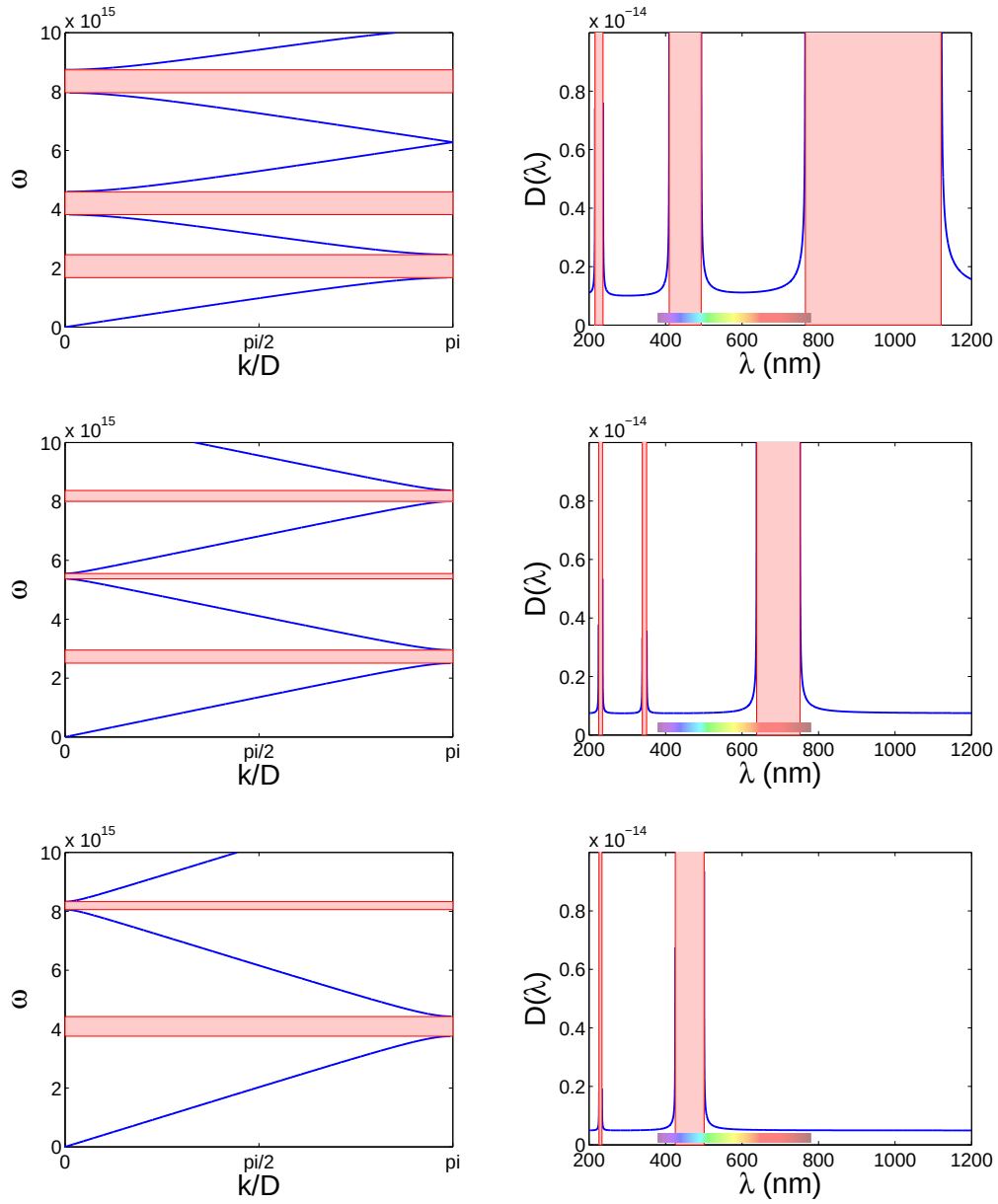

Figure 2.4.: Photonic dispersion relation (left row) and corresponding density of states (right row) of infinite repeat units with following material properties:
n_1=1, n_2=2.0, d_1+d_2=300 nm and d_2=150 nm (top)
n_1=1, n_2=1.3, d_1+d_2=300 nm and d_2=150 nm (middle)
n_1=1, n_2=1.3, d_1+d_2=200 nm and d_2=100 nm (bottom).

frequencies compared to the dispersion relation in the middle. If the layers have a great refractive index the bandgap shifts to lower λ and if the difference in the two refractive indices is large, the bandgap gets broad [26]. The full bandgap width at half maximum is [26].

$$\Delta E = \frac{4}{\pi} \frac{n_1 - n_2}{n_1 + n_2} \tag{2.49}$$

The influence of the layer thickness is demonstrated in the dispersion relation on the bottom. The refractive index of the two layers is the same as in the middle but the thickness of the repeat unit decreases from D=300 nm to D=200 nm. The single layer thickness was again chosen to be the half of D. The bandgaps move to a lower λ. In the dispersion relation on the right the first order bandgap is in the blue range at 425 nm to 500 nm. This is, in terms of the wavelength, the lowest bandgap of the three demonstrated dispersion relations.

An alternative and easy formula for the bandgap position can be derived by combining Snell's law and Bragg's law. The reflections at each repeat unit interfere. Positive interference occurs when the two waves are in phase. The path difference of Bragg's law needs to be modified with the refractive index by Snell's law. The wavelength differs with $\lambda_{\text{medium}} = \lambda_{\text{vac}}/n$. The formula to calculate the position of the bandgap under an incident angle α, measured to the lot, is [26]:

$$m \cdot \lambda_{\text{Gap}} = 2(d_1 + d_2)\sqrt{sin^2(\alpha) - n_{\text{eff}}} \tag{2.50}$$

$$n_{\text{eff}} = \frac{n_1 d_1 + n_2 d_2}{d_1 + d_2} \tag{2.51}$$

with d_1 and d_2 the two layer thicknesses and m the order of the bandgap. The refractive index n_{eff} is an averaged refractive index with the respect of the layer thickness. Under a perpendicular incident beam the formula simplifies to:

$$m \cdot \lambda_{\text{Gap}} = 2(d_1 n_1 + d_2 n_2) \tag{2.52}$$

With the bandgap position and the full width at half maximum the layer thicknesses can be simulated. This is a typical approach to determine the repeat unit within a distributed Bragg reflector [10]. With X-ray reflectivity the layer thickness can be measured and does not need to be calculated. This is a great advantage because the form of the bandgap depends also on structural defects caused by the spin casting technique [27].

2.5. Distributed Bragg Reflectors and Cavities

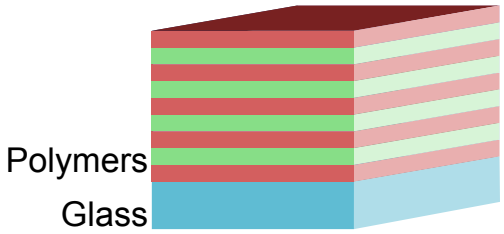

Figure 2.5.: Schematic build-up of a DBR on a glass substrate. A red and a green layer represent a repeat unit which is deposited several times. The two colors indicate two different refractive indices.

Distributed Bragg reflectors (DBR) are one dimensional photonic crystals. The DBRs in this study will be made of two alternating spin casted organic polymers on a glass substrate. Figure 2.5 illustrates a build-up, where double layers of the polymers P_1 and P_2 were assembled as a stack of four repeat units and an extra layer of P1. The polymer with the higher refractive index is applied first and last to enhance the reflectivity of the DBR. Such a structure is called $(P_1\text{-}P_2)_4P_1$ which indicates that the repeat unit $(P_1\text{-}P_2)$ is applied 4 times followed by an additional P_1 layer.

The transmission spectrum of the build-up of figure 2.5, simulated with the transfer matrix method, is plotted in figure 2.6. The layer properties were chosen to be the same as in the example of an infinite repeat unit system in figure 2.4 (top). The bandgap in the transmission spectrum is a peak directing downwards. Three large bandgaps can be seen. The first order bandgap lasts from 740 nm to 1200 nm and the second order bandgap from 400 nm to 505 nm. Comparing the simulated spectrum with the density of states of figure 2.4 (top), the bandgap position as well as the width match. The bandgap of the DBR attains a reflectance up to 98.8 %, which is impressive for such a small amount of repeat units.

Between the bandgaps the spectrum has got some fringe-like features. They can be seen as interference patterns of the first reflected beam and the reflection on the glass substrate. Above 1000 nm the line is broadened. The glass substrate itself produces an interference pattern with narrow fringes caused by the reflections at the two boundary surface. Below 1000 nm the fringes are so narrow, that the modeled spectrometer cannot resolve it. The simulation takes a spectrometer equipped with a 1 mm split width into account.

The reflectance is dependent on the difference of the refractive index, the ratio of the thicknesses and the number of repeat units of the two polymers. The example presented,

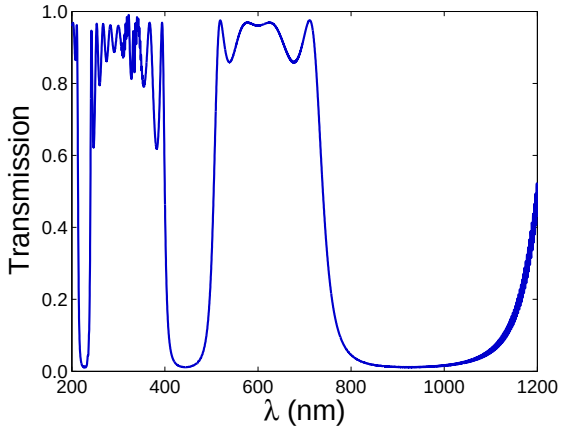

Figure 2.6.: Transmission spectrum of a simulated DBR of figure 2.6 with $n_{P1} = 2$, $n_{P2} = 1$, n_{glass} =1.33, d_1+d_2 =300 nm, d_2 =150 nm and d_{glass} =0.2 mm.

has got a difference in the refractive index of $\Delta n = 1$, which is quite high. However the refractive index of polymers are in the limit of 1.3 to 1.7.

For given reflective indices, the best reflectance is obtained, when the optical path length in each layer is equal ($n_1 d_1 = n_2 d_2$) [4]. In the example presented in figure 2.6, the ratio of thicknesses of the two layers is 1. For two materials, with a reflective index of n_1=2 and n_2=1, the optimal thicknesses would be d_1=100 nm and d_2=200 nm. With this thicknesses the reflectance would increases from 98.8 % to 99.5 % but of course the position of the bandgap shifts as well (see equation 2.52). It has been tested, that a deviation of the thickness ratio does not influence the reflectivity a lot. However for applications, which require high reflectance, the optimal thickness ratio should be adhered.

The reflectance versus the repeat unit can be calculated with [28]:

$$R = \left(\frac{n_0 n_2^{2m} - n_3 n_1^{2m}}{n_0 n_2^{2m} + n_3 n_1^{2m}} \right)^2 \tag{2.53}$$

with the refractive index of the substrate n_0, the refractive indices of the two layers n_1 and n_2 and the number of repeat units m. This easy relation is true for layer thicknesses of quarter-wavelength.

However real DBRs suffer a loss in reflection caused by thickness variation along the depth and along the footprint of the sample and by interface roughness. In this study these parameters will be determined.

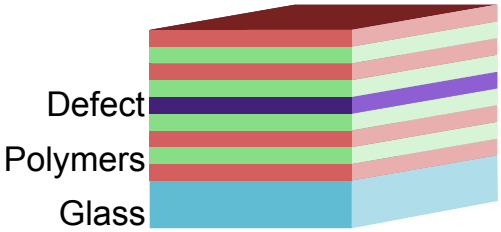

Figure 2.7.: Schematical build-up of a cavity. A defect layer is embedded between two DBRs and causes a symmetry break.

A defect layer, embedded within two DBRs, causes a symmetry break in the repeat unit. Such structure is illustrated in 2.7 and will be called cavity. The defect layer can either be a layer of different material or of a different thickness. The essential quantities are the refractive index and the thickness of the defect. With the transfer matrix method, a defect layer within repeat units can easily be simulated.

In figure 2.8 the transmission spectrum of the DBR of figure 2.6 is compared to a cavity. In the bandgap of the cavity an inverse sharp peak is located. This is an intermediate photon energy state. Photons with a wavelength in between the bandgap cannot propagate into the cavity, except in the narrow region of the intermediate state.

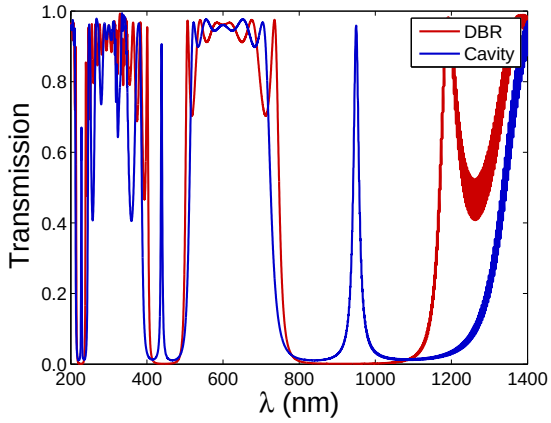

Figure 2.8.: Transmission spectrum of the DBR of figure 2.6 compared to the cavity of figure 2.7 with the defect layer: n_{def}=1 and d_{def} =150 nm.

The cavity can be used as resonator, and if the defect layer is fluorescent in the region of the intermediate photonic state, spontaneous emission can be enhanced. This is called the Purcell effect [29]. A dye embedded in a photonic crystal has already been tested in modern research with great laser-like results [6, 11, 30].

3. Methods

3.1. X-ray Reflectivity

The X-ray reflectivity (XRR) method is a surface sensitive technique to analyze the morphology of thin films. The incident X-ray beam strikes the sample surface and gets reflected in specular direction. In figure 3.1 the arrangement of the incident wave vector $\mathbf{k}_i$, the reflected wave vector $\mathbf{k}_r$, the scattering vector $\mathbf{q}$, the incident angle θ and 2θ, the angle between $\mathbf{k}_i$ and $\mathbf{k}_r$, is illustrated. Morphology examinations of organic-inorganic and organic-organic interface were already successfully performed by the XRR method [31–34]. For a more detailed description the book *X-Ray and Neutron Reflectivity* by J. Daillant and A. Gibaud is recommended [35].

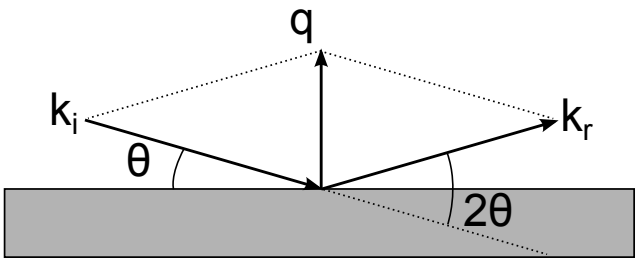

Figure 3.1.: Specular condition of the XRR scan with the incident wave vector $\mathbf{k}_i$, the reflected wave vector $\mathbf{k}_r$, the scattering vector $\mathbf{q}$, the incident angle θ and 2θ, the angle between $\mathbf{k}_i$ and $\mathbf{k}_r$.

For an explanation of a XRR curve, the optical properties of X-rays propagating through materials have to be considered. The refractive index n for an arrangement of N atoms can be assumed as an ensemble of harmonic oscillators with a resonance frequency ω_i [36].

$$n = 1 + \frac{\rho_{e^-}}{2\pi m}\frac{e^2}{4\pi\epsilon_0}\sum\frac{s_i}{\omega_i^2 - \omega^2} \tag{3.1}$$

with ρ_{e^-}, the electron density, s_i, the weighting of the oscillator and ω, the frequency of the exciting electromagnetic wave. The frequency of X-rays is far beyond the resonance

frequency of solids $\omega \gg \omega_i$, which would be in the infrared up to ultraviolet spectrum. With the classical electron radius r_{e^-} $\left(r_{e^-} = \frac{e^2}{4\pi\epsilon_0 m_{e^-} c}\right)$,the electron mass m_{e^-} and the speed of light c, the equation equals:

$$n = 1 - \frac{\overbrace{\rho_{e^-}\lambda^2 r_{e^-}}^{\equiv\delta}}{2\pi m} \tag{3.2}$$

The imaginary part of the refractive index is related to the attenuation coefficient μ via:

$$\beta = \frac{\lambda}{4\pi}\mu \tag{3.3}$$

$$n = 1 - \delta + i\beta \tag{3.4}$$

The real part of the refractive index is slightly below 1 with $\delta \approx 10^{-6}$. Under a small incident angle, the cosines in the Snell law in equation 3.5 can be simplified to $cos(\alpha) = 1 - \alpha^2/2$. If the angle of the transmitted beam α_t in equation 3.6 is imaginary, the wave cannot propagate into the material and gets totally reflected. The critical angle α_c can be linked to the real part of the refractive index. For the typical radiation of a copper Kα tube, with λ =1.54 Å, the critical angle is in the region of 0.1 °< α_c <0.4 ° [36, p. 162]. Up to the critical angle, the intensity gets completely reflected.

$$\frac{1}{n} = \frac{cos(\alpha_t)}{cos(\alpha_i)} \tag{3.5}$$

$$\alpha_t = \sqrt{\alpha_i^2 - 2\delta} \tag{3.6}$$

$$\alpha_c = \sqrt{2\delta} \tag{3.7}$$

Above the critical angle the wave can propagate into the material. The intensity of reflectance can be calculated with the Fresnel coefficients (see equation 2.43):

$$r = \frac{k_{iz} - k_{tz}}{k_{iz} + k_{tz}} \tag{3.8}$$

with k_{iz} and k_{tz} the z-component of the wave vector of incident and transmitted beam. The intensity is the absolute square root of the Fresnel coefficient $I = |r|^2$. Slightly above the critical angle $\alpha_i > \alpha_c$ the intensity drops significantly with the inverse fourth power of the scattering vector $I \propto q^{-4}$, which is called the Porod slope [37]. Nevot et al. discovered, that the surface- and interface-roughness (σ_{rms}, root mean square) cause the signal to drop

more rapidly, with **q** the scattering vector [38].

$$R_{\text{rough}} = R_{\text{ideal}} e^{-\mathbf{q}^2 \sigma_{\text{rms}}^2} \tag{3.9}$$

$$q = \frac{4\pi}{\lambda} sin(\theta) \tag{3.10}$$

In 1954 Lyman G. Parratt used the Fresnel equation iteratively for the investigation of samples consisting several layers [39]. The index j numerate the layers and the parameter z denotes the thickness.

$$r_{j,j+1} = \frac{k_{z,j} - k_{z,j+1}}{k_{z,j} + k_{z,j+1}} \tag{3.11}$$

$$X_j = \frac{R_j}{T_j} = e^{-2ik_{z,j}z_j} \frac{r_{j,j+1} + X_{j+1} e^{-2ik_{z,j}z_j}}{1 + r_{j,j+1} + X_{j+1} e^{-2ik_{z,j}z_j}} \tag{3.12}$$

The intensity of the incident wave can be normalized ($T_1 = 1$). There is no reflection from below the surface ($X_{N+1} = 0$) Each Fresnel coefficient can be calculated iteratively and multiplied with the influence of the roughness of equation 3.9. The gained intensity oscillates with the incident angle. Each interface in the sample causes reflection and all layers together produce an interference pattern, so called Kiessig fringes [40]. There is a great affinity between the Parratt formalism and the transfer matrix method, introduced in chapter 2.3.

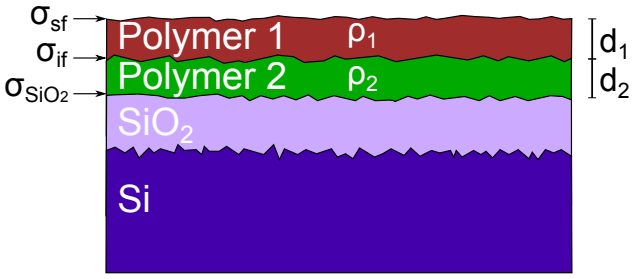

Figure 3.2.: Schematic morphology of a polymer double layer sample on a thermally oxidized silicon substrate. The parameter measurable with XRR are marked. The electron densities ρ_1 and ρ_2, the film thicknesses d_1 and d_2, the surface roughness σ_{sf} and the interface roughnesses σ_{if} and σ_{SiO2}.

In figure 3.2 a schematic morphology of a sample used in this study, is shown. Two polymer layers on top of a thermally oxidized silicon substrate are marked with all the parameters, that can be determined with XRR. The electron density ρ, the film thicknesses the surface- and interface-roughness. In figure 3.3 the influence of the parameters on a XRR

curve is illustrated. The first plot demonstrates, that large film thickness causes narrow fringes. The difference of the m^{th} and $m{+}1^{\text{th}}$ fringe in a 2θ curve is approximately λ/d [36, p. 170]. For a radiation of λ=0.154 nm and a film thickness of d=300 nm the distance of two fringes is about 0.03 °. This is about the limit of the resolution of the goniometer to determine thin film thickness. Larger film thicknesses than 300 nm is difficult to evaluate. In the second plot we see, that rough surfaces dilute the fringes. In the third plot the effect of the electron density is substantiated. A greater electron density leads to a higher critical angle. The last plot indicates, that rough interfaces cause the signal to drop faster.

It has to be mentioned, that all layer properties within a sample can be quantified simultaneously. During increasing incident angle, the beam penetrates deeper into the sample and the intensity curve becomes more and more sensitive to the underlying layers.

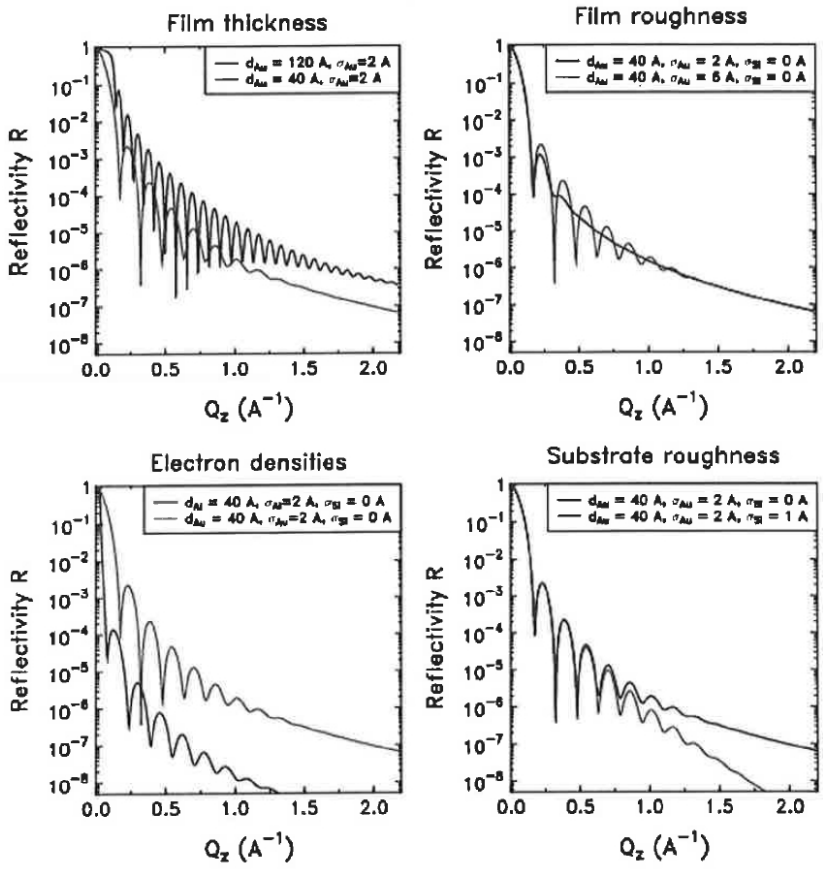

Figure 3.3.: The influence of the sample properties: a thin film broadens the fringes (top-left), a rough surface dilute the fringes (top-right), a high electron density increases the critical angle (bottom-left) and a rough interface suppresses the intensity in higher q regions (bottom-right) [41].

The goniometer used, was a *PANalytical Empyrean* system with radiation of a copper tube (λ=1.54 Å). The setup is plotted in figure 3.4. On the primary side the reflectometer is equipped with a 1/32 ° divergence slit, a 10 mm beam mask and a multilayer mirror (equatorial divergence less than 0.055 °) and a beam attenuator. On the secondary side is a receiving slit of 0.1 mm, a Soller slit of 0.02 rad and a *PANalytical PIXEL^{3D}* used as point detector. The incident angle was varied from 0 ° to 5 ° with a stepsize of 0.004 °. This divergence slit and receiving slit were chosen to get a focused beam. Otherwise the divergence cause a crucial loss in resolution of the fringes. The intensity of the totally reflected beam would cause damage to the detector. Therefore the system is equipped with an automatic beam attenuator. The values for the automatic to turn the attenuator on is above 900000 counts/s and switching it off at 600000 counts/s.

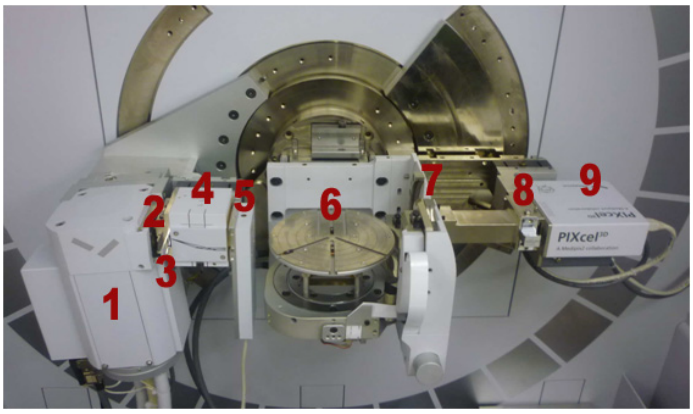

Figure 3.4.: Goniometer of XRR: (1) copper tube, (2) divergence slit, (3) beam mask, (4) multilayer mirror, (5) attenuator, (6) sample stage, (7) receiving slit, (8) Soller slit and (9) detector.

With the *X'Pert Reflectivity* software the data were fitted. The software was developed as an application together with the *PANalytical Empyrean*. The software takes the substrate length and the beam width into account. Further the intensity, the background and the beam divergence are fitting parameters. The sample is simulated with layers of different material. The software offers a great database for the absorption coefficients of elements for different typical tube radiations. Beside a graph for the reflectivity function, the software offers the plotted Fourier transform. With the input of the critical angle, the peaks in the Fourier transform are immediately the thickness of the films. The fitting parameters are the mass density, the thickness, the interface- or surface- roughness of the layers. Each fitting parameter can be chosen to stay fixed or to vary in a specified range during the fitting procedure. The fitting routine attempts to minimize the absolute square root difference of the measured to the fitted curve. The absolute square root difference is called fit

value. Additional available are a minimization of the logarithmic difference or the squared logarithmic difference.

The two fitting methods are a segmented fit and a genetic algorithm. With the segmented fit the reflectivity curve gets divided into three parts. Starting with the first segment the fitting parameters vary and remain at the best fit value till a suitable fit is obtained. The process repeats incrementally over increasingly larger segments until the full reflectivity curve is fitted. The advantage of this method is, that the first section of the reflectivity curve, containing the critical angle and the first fringes, is the most important one and gets most considered in this method. The genetic algorithm method takes a number of random fit parameters which are called population. The parameters with the best fit value is taken to generate the next population. The procedure stops when a specific fit value is reached or the change from one population to the next is under a convergence value. The fitting method chosen in this study is the segmented fit.

The starting parameters are crucially important. Easy the fitting routine can get stuck in a local minimum. It is highly recommended to choose proper starting parameters. For the fit parameter of the density of the materials the critical angle gives a clue. A higher density increase the critical angle. If the layered sample consists of layers of different electron densities, the reflectivity curve reveals two critical angle. The density of different polymers are close. It is not possible to dissolve the critical angle of the polymers used in this study. Double layer samples should not be measured till the substrate and the single layer films are examined.

The software *X'Pert Reflectivity* uses the mass density in g/cm^3 as a fitting parameter. However the critical angle α_c is with equation 3.7 and equation 3.2 linked to the electron density. The chemical formula indicates the number of electrons and the molecular weight of the unit cell. The equation to link the mass density in g/cm^3 and the electron density in e^-/cm^3 is:

$$\rho_{e^-/cm^3} = \rho_{g/cm^3} \cdot N_A \frac{A_{e^-}}{\mathrm{MM}} \tag{3.13}$$

with the Avogadro constant N_A, the number of electrons A_{e^-} and MM the molecular mass.

Table 3.1.: Chemical formula, the number of electrons and the molecular mass.

	CA	PS	PVK	oxidized silicon	silicon
Chemical formula	$C_6O_5H_{10}$	C_8H_8	$C_{14}H_{11}N$	SiO_2	Si
Number of electrons	86	56	102	30	14
Molecular weight (g/mol)	162.16	104.16	193.26	60.08	28.08

With the parameter of table 3.1 the electron density of the materials used in this study can be calculated out of the mass density.

The investigation of the change of layer morphology with temperature treatment was performed with the domed heating stage *DHS 900* of figure 3.5. A similar setup was already been tested by H. Flesch et al. with the determination of the temperature dependency of self assembled monolayers [42]. To prevent the samples from oxidation, the dome got constantly floated by helium. Starting at 60 °, with temperature steps of 10 ° up to 200 °, the sample was heated for 2 min. After each step, the sample cooled back down to room temperature and a XRR scan was taken.

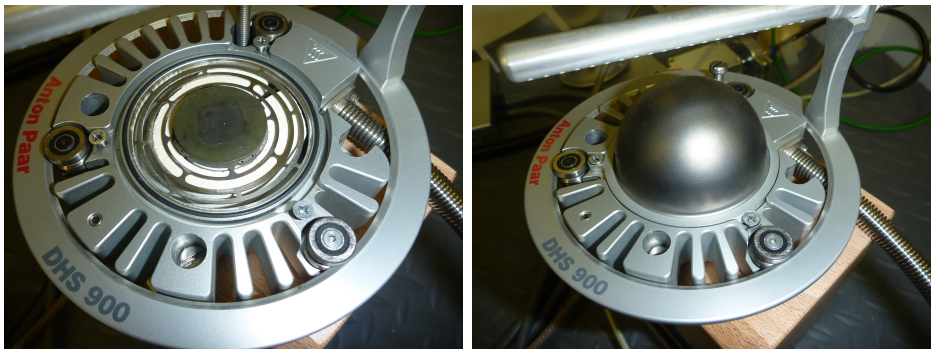

Figure 3.5.: Domed heating stage: *DHS 900*.

3.2. Atomic Force Microscopy

Atomic force microscopy (AFM) is a sub-technique of scanning force microscopy. The measurement is based on the force between a cantilever (tip) and the sample surface. It was invented in 1985 by G. Binnig, C. Quate, and Ch. Gerber [43]. The cantilever screens along the surface and measures the force to the surface. The contributing forces are the inter-atomic repulsive force, which is of short range and the long range forces (Coulomb force, dipole-dipole interaction, van der Waals force,...). Ideally the cantilever touches the surface by a single atom. AFM can map the topography of the surface down to atomic dimensions.

The attractive long range force pressures the cantilever onto the surface. If the surface is soft the cantilever scratches and destroys the material. A more gentle technique is the tapping mode. With a pieco oscillator the cantilever is driven near its resonance frequency. The topographic information is retrieved from the amplitude of the oscillating cantilever.

The cantilever does not scratch the surface since the intermittent contact eliminates lateral shear strain.

There are existing two different operating modes, the constant height and constant force mode. With the constant height mode the vertical position is kept unchanged during scanning. Therefore higher scan speeds can be achieved which can be useful to suppressed thermal drifts. This mode has to be used with caution as the cantilever might crashes into high profiles. A tip crash has to be avoided in any case. The constant force mode regulates the distance of the cantilever and the sample to a constant deflection. Because the feedback system needs time to regulate the cantilever, this mode is slower but tip crashes can be prevented.

To determine soft matter materials like polymer thin films, the mode of need is the tapping mode with constant force. The material will be neither scratched nor the cantilever crashes into high grains.

The atomic force microscope we used, was a *MFP-3D stand alone* from *Asylum Research*. We used a medium soft silicon cantilever named *OMCL-AC240TS*. With a spring constant of 2 nm, it is suitable for observing surfaces of soft or viscous materials [44]. The set point was 780 mV, the drive frequency of the piezo element was 60 kHz and the scan speed was 10 µm/s. *Gwyddion* was aquired as software to to visualize the data and analyze the surface roughness, the lateral correlation length and the Hurst parameter.

3.3. Spectroscopic Ellipsometry

Spectroscopic ellipsometry is a technique to investigate the optical properties and the thickness of thin films. The real and imaginary part of the refractive index are excess-able. The method is convenient for inorganic and organic thin films and is based on the change of the polarization and the intensity during reflection. The primary beam is usually linear polarized. The reflected beam is elliptical polarized, because of the different reflection coefficients for TM and TE polarized light of figure 2.2 (equation 2.43). The incident angle should be close to the Brewster angle [45] of the material. A fitting approach with transfer matrices is most likely, but with the difference that now we need to consider the imaginary part κ of the refractive index. According Beer-Lambert law an electromagnetic wave needs to be multiplied with a damping factor $e^{\frac{-2\pi\kappa z}{\lambda}}$ [46, 47], with the attenuation κ along the depth of penetration z.

In spectroscopic ellipsometry the measured quantities are ψ and Δ in terms of λ. The amplitude of the ratio of the reflection coefficients of the TE and the TM polarization is $tan(\psi)$ and the phase difference is Δ.

$$\frac{r_{\mathrm{TM}}}{r_{\mathrm{TE}}} = tan(\psi)e^{i\Delta} \tag{3.14}$$

Specular ellipsometry scans were performed with a *VASE Ellipsometer* including a *J.A. Woollam* HS-190 monochromator. The setup is shown in figure 3.6. Under the incident beam angles of 65 ° and 75 ° to the surface, ψ and Δ spectra between 240 nm and 1340 nm were measured and fitted with *VASE*. The fitting routine simulated a layer system where the refractive index $N = i\kappa + n$ and the layer thickness were fitting parameters. In this study double polymer layer samples on thermal oxidized silicon were investigated with spectroscopic ellipsometry. The substrate was simulated as 1 mm thick silicon layer underneath an 150.3 nm thick silicon oxide layer. The parameters of these two layers were fixed. On top, a so called simple gradient index layer, was modeled. The layer got separated into two parts of equal thickness but with a gradient in the refractive index. For con-natural polymer layers, with similar thickness, this approach is proper and has the benefit of less fitting parameters. The refractive index varies in λ by applying oscillators in the part of the energy spectrum where absorption happens. The height, width and the position of the oscillators are fitting parameters.

Spectroscopic ellipsometry has already been used in the domain of photonic crystals [11, 24, 48]. A great advantage, compared to XRR, is the access to the refractive index in addition to the layer thickness. However the mapping of the refractive index can get sophisticated in regions of absorption.

3.4. Polymers

Suitable organic polymers in the domain of one dimensional photonic crystals should fulfill several requests. Thicknesses of about 100 nm of polymer layers should be feasible. Mostly the materials need to be transparent in the visible spectrum. Further the dispersion relation n(λ) in the visible spectrum should be moderately flat. The surface needs to be smooth and the interface should be sharp to demagnify the light scattering and to ensure the periodicity.

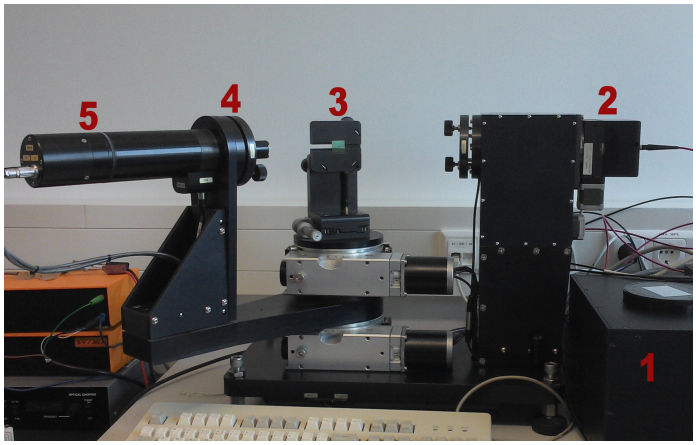

Figure 3.6.: Setup of the ellipsometer: monochromator (1), polarisator (2), sample stage (3), analysator (4), detector (5).

Cellulose Acetate (CA)

Cellulose is a structural component in the skeleton of plants. It is formed of a linear chain of up to thousands of beta-glucose unities. The hydroxylgroup is offering great derivation possibilities to change the molecule. With an esterification reaction of acetic acid cellulose acetate (CA) can be obtained. The chemical structure of the monomer is shown in figure 3.7.

CA is solvable in several polar solvents like diacetonalcohol, methylene chlorid or alcohol hydrocarbons. However it cannot be solubilized in water, ethylic alcohols nor aromatic solvents. In this work CA was solved in diacetonalcohol. The alcohol OH group provides adequate polarity to solve CA. Solutions of concentrations of about 60 g/l are accessible. The standard concentration is c_{CA}=27 g/l. Types of polymers with aromatic rings like polystyrene and polyvinylcarbazol cannot be dissolved in diacetonalcohol.

CA films are transparent in the visible and in the near infrared spectrum. The refractive index is n_{CA}=1.475 with a low dispersion relation in the visible spectrum. The CA in this study is distributed by *Sigma Aldrich* [49]. The molecular weight is M_W=63000 g/mol. It is provided in a white dusty powder form.

Polystyrene (PS)

Polystyrene (PS) is a widely-used polymer. It can be foamed which is called Styrofoam or is a rigid and amorph plastic. The glass transition temperature is about 100 °C and it is stable at temperatures up to 270 °C. PS degenerates in ultraviolet light and gets brittler.

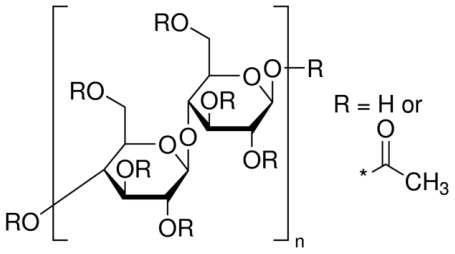

Figure 3.7.: Chemical structure of CA [49].

Because it is stable against polar solvents like water, PS is used as grocery package. Unfortunately it is not biodegradable. It dissolves in polar solvents like benzene or toluene.

Solutions with concentrations up to 60 g/l are clear and homogeneous. The standard concentration is c_{PS}=32 g/l. With spin casting the solution forms thin films of optical high quality. By varying the spin speed and the concentration a wide range of film thickness from 50 nm to 500 nm is available. Among polymers the refractive index of PS is high n_{PS}=1.59 in the region of visible light. PS is transparent in the visible spectrum.

The PS is provided by *Sigma Aldrich* [50]. It was solved in toluene. The molecular weight is M_W=192000 g/mol. It is delivered in rigid beams with the diameter of 1 mm with a weight of 30 mg each.

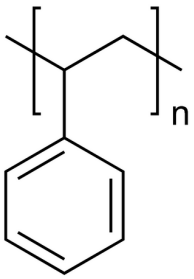

Figure 3.8.: Chemical structure of PS [50].

Polyvinylcarbazol (PVK)

Polyvinylcarbazol (PVK) is a temperature-stable commercial dielectric polymer. Against alkaline acids, water and salt solutions PVK is steady. Because of its stability, it is used in the insulation technology. The glass transition temperature is about 200 °C. The chemical structure of PVK, $C_{14}H_{11}N$, is plotted in figure 3.9.

PVK cannot be solved in polar solvents but it is soluble in alcohol, ester and toluene. In this study the solvent for PVK is toluene. Solution concentrations up to 50 g/l are clear and homogeneous. The standard concentration is c_{PVK}=24 g/l. While spin casting multistacks of PVK and CA the sample gets milky. With an extra heating procedure of the sample every three applied double layers this can be prevented. The sample needs to be heated to 80 °C for about 3 min to let all the toluene evaporate. The refractive index of PVK is one of the highest among polymers with n_{PVK}=1.696. The PVK in this work is distributed by *Polyscienc, Inc.* [51]. It is delivered as white flake-like powder.

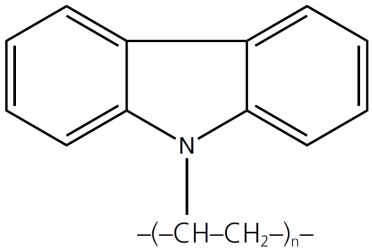

Figure 3.9.: Chemical structure of PVK [51].

Poly(3-hexylthiophen) (P3HT)

Poly(3-hexylthiophen) (P3HT) belongs to the group of tolythiophene. It is an organic p-type semiconductor. In electronic devices it is used as a photo active layer in organic photovoltaic or as a semiconducting layer in field-effect transistors. P3HT is optical active and has an absorption maximum (in toluene) at 445 nm and a fluorescence maximum at 567 nm. Furthermore it is soluble in toluene and xylol. In this thesis toluene was used as solvent. The P3HT is distributed by *American Dye Source* [52]. It is a dark and brown powder. The regioregularity is regio-random and the molecular weight is 50000 g/mol to 150000 g/mol. The structure and the absorption and fluorescence spectrum are represented in figure 3.10 and figure 3.11.

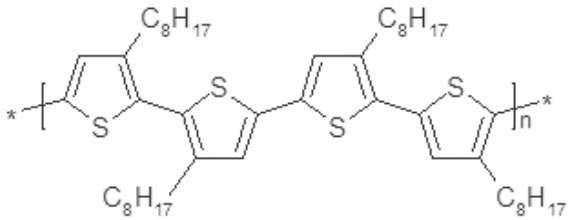

Figure 3.10.: Chemical structure of P3HT [52].

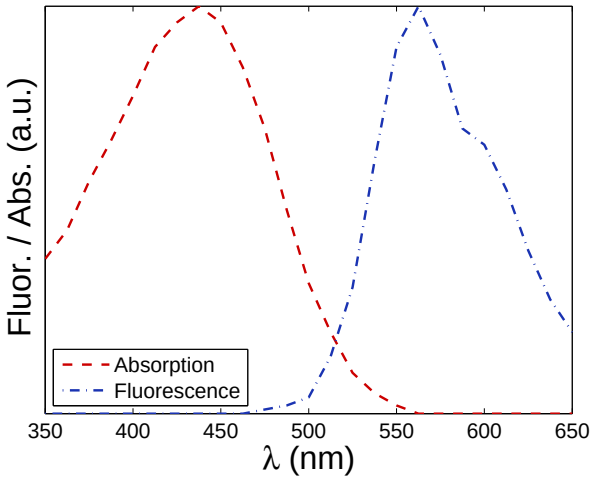

Figure 3.11.: Absorption and fluorescence spectrum of P3HT [52].

3.5. Preparation of the Polymer Layers

For the manufacturing of polymer multilayer stacks the dynamical spin coating technique is suitable and in the research field of photonic crystal well established [10, 17, 18]. The procedure is explained in figure 3.12. The spin coater was rotating permanently and the two solutions were deposited alternating one at a time.

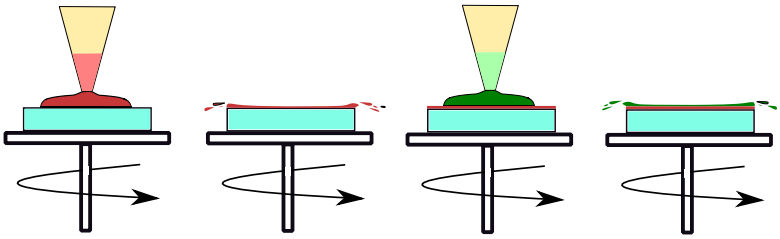

Figure 3.12.: Preparation of polymer mulitlayer stacks.

Particular attention should be paid exactly at the moment of tipping. The pipette is close to the surface or even slightly touching it. The solvent is poured out continuously so the flow does not get a break. Afterward the solvent needs to dry. If a CA layer is applied, it takes up to 45 s to get dried. If a PS or a PVK layer is deposited a duration of 30 s is sufficient. After some layers the surface provides a visual back check of the drying. While the solvent is evaporating, rainbow colored circles are spreading from the middle to

the edges of the sample. When this stops, the solvent is gone and the polymer layer is dried. The next polymer solution can be spin coated on top of it. Orthogonal solvents are required, so that the underlying layer is not dissolved by the next layer. Multistacks made of CA and PS or CA and PVK are possible and already been tested several times [10, 11, 30].

The DBRs $(PS\ CA)_{20}PS$ and $(PVK\ CA)_X$ were dynamically spin casted on glass substrates with an applied volume of 105 µl and spin velocities in the range of 90-180 rps for each layer. For the investigation with XRR, single layer samples CA, PS and PVK and double layer samples PS-CA and PVK-CA and the reverse samples CA-PS and CA-PVK were spin casted on thermally oxidized silicon substrate with a volume of 90 µl. As each polymer can react differently in its wetting behavior, it is necessary to fabricate not only a stack polymer 1 - polymer 2 but also the inverse one: polymer 2 - polymer 1. A sample, where the PS was deposited first and the CA is applied on top, will be called PS-CA. All silicon substrates in this thesis are thermally oxidized silicon wafers with an oxide layer of d_{SiO2} =150 nm and a dimension of (20×20) mm. The wafers were cleaned in aceton in an ultrasonic bath for 10 min and afterward in isopropanol in an ultrasonic bath for 10 min.

3.6. Measuring of Spectra

Directly after the preparation of the DBRs and the cavities, the devices were characterized with a *Ava-Spec-2048 XL* spectrometer from *Avantes*. The light source was a *AvaLight-Hal* also from *Avantes*. The setups for measuring reflectivity and transmission are plotted in figure 3.13.

To measure the reflectivity, the sample is placed on the black ring. The light source and the detector wire is implemented in the greyish cable above the black ring. For the transmission spectrum, the sample is placed in between the light source and the detector. In figure 3.13 the light source in the right upper corner, the sample in the middle and the detector in the left lower corner, can be seen. With a high optical reflecting mirror the spectrum of the light source was evaluated. A spectrum without light source but with the sample was taken as a background spectrum. A reflectance spectrum of a sample was calculated by:

$$R = \frac{\mathrm{I_{sample}} - \mathrm{I_{backgr.}}}{\mathrm{I_{source}} - \mathrm{I_{backgr.}}} \tag{3.15}$$

The measured area on the sample is about $1\,\mathrm{mm}^2$. Spectra at four different spots on the sample were taken to see the homogeneity of the DBR. Because all of them were not significantly different, only one spectrum of the four will be represented.

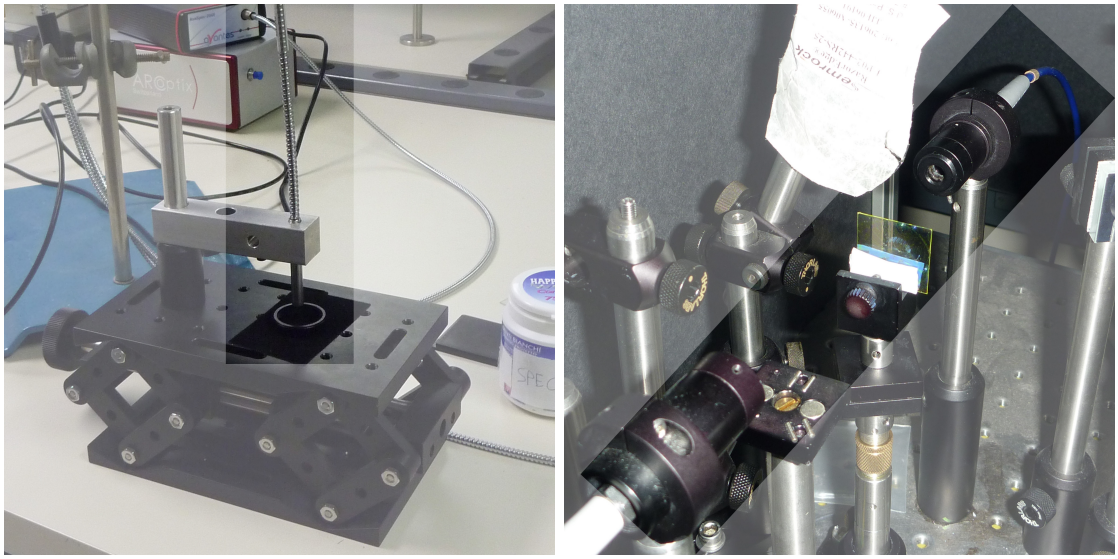

Figure 3.13.: Setup for measuring the reflectance (left) and for measuring the transmission (right).

After one month the spectra of the devices were examined with a *UV-1800* from *Shimadzu*. The sample is placed in a small chamber, see figure 3.14. The routine to normalize the spectrum to the source and the background is done automatically under the baseline menu in the *UV Probe* software. The slit of the spectrometer is 1 nm.

Figure 3.14.: Sample chamber of the *UV-1800* from *Shimadzu*.

4. Results and Discussion

4.1. Morphology of All-Polymer Layers

In the following section the results of the investigations of polymer layers of cellulose acetate (CA), polystyrene (PS) and polyvinylcarbazol (PVK) will be presented. With X-ray reflectivity the density, the layer thickness and the surface- and interface-roughness will be determined. With atomic force microscopy the surface will be revealed and with spectroscopic ellipsometry the refractive index as well as the thickness will be evaluated.

4.1.1. X-ray Reflectivity Results of Single Layer Films

Figure 4.1.: CA, PS and PVK single layers on thermally oxidized silicon substrates.

Each polymer (CA, PS and PVK) was deposited on a silicon substrate to investigate single layer films produced with the spin conditions represented in table 4.1 with XRR. Figure 4.1 depicts the sample setup. The layer was homogeneous and the coloring was highly continuous which suggest an uniform thickness over the hole substrate. No crystallization was observed.

The XRR results are plotted in figure 4.2. The reflectivity was scaled to one, and for a better view the three functions in one graph were vertically shifted. In the plot on the top the XRR curves of the three CA single layers are charted. The plot in the middle shows three PS single layers and at the bottom three PVK single layer are plotted. Each XRR has two critical angles α_{c1} =0.15 ° and α_{c2} =0.22 °. The first is caused by the polymer and the second one by the silicon substrate.

The XRR result of CA 1, which was prepared with a fast spin speed of 180 rps and a standard concentration of 27 g/l, has broad and defined fringes. This indicates a smooth surface and a thin layer. In the XRR graph of CA 3 the fringes are nearly gone. The high concentration of 54 g/l and the low spin velocity of 70 rps led to such a thick layer, that the limit of the resolution of the XRR method was reached. The results of PS 1, PS 2 and PS 3 and PVK 1, PVK 2 and PVK 3 were likewise. A high spin velocity led to broader fringes and a high solution concentration led to narrow fringes.

Table 4.1.: Preparation condition and obtained fit parameters of the XRR graphs of single layer films of CA, PS and PVK with conc., the polymer solution concentration, speed, the spin velocity, ρ the mass density, d, the film thickness and $\sigma_{sf/if}$, the surface roughness and the interface roughness between the polymer and the substrate.

	conc. (g/l)	speed (rps)	ρ (g/cm^3)	d (nm)	σ_{sf} (nm)	σ_{if} (nm)
CA 1	27	180	1.26	59	0.36	0.50
CA 2	27	70	1.20	96	0.35	0.56
CA 3	54	70	1.17	289	0.35	0.60
PS 1	32	180	1.15	112	0.27	0.40
PS 2	32	70	1.09	211	0.28	0.39
PS 3	64	70	1.07	246	0.29	0.40
PVK 1	24	180	1.35	39	0.33	0.82
PVK 2	24	70	1.34	62	0.33	0.76
PVK 3	48	70	1.25	200	0.34	0.80

The XRR graphs were fitted and the mass density, the thickness and the surface and interface roughness are listed in table 4.1. The numerical errors are not been mentioned, as they are not representative for the measurement. Apparently the concentration and the spin speed are directly linked to the thickness of the layer. With a higher speed and a lower concentration thinner films were obtained. The mass density varied for each polymer in an insignificant manner. The surface roughness for each polymer was remarkable small ($\approx$0.3 nm) under the circumstances of using such a rude technique as spin casting. The averaged interface roughness between the substrate and the polymer was the smallest for PS with σ_{if}=0.40 nm followed by CA with σ_{if}=0.55 nm and PVK with σ_{if}=0.79 nm. The fringes in the XRR vanished at above 200 nm for each polymer. For the double layer samples the preparation condition of table 4.3 were chosen to attempt similar thickness results than of CA 1, PS 1 and PVK 2.

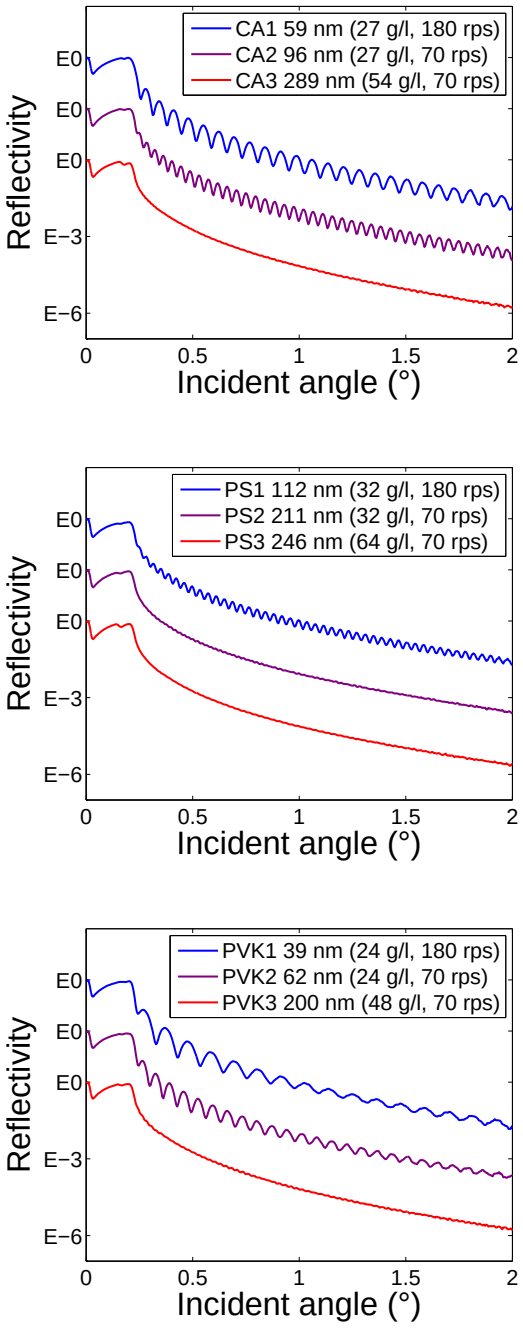

Figure 4.2.: XRR results on spin casted cellulose acetate (CA) (top), polystyrene (PS) (middle) and polyvinylcarbazol (PVK) (bottom) with the preparation conditions of table 4.1. The layer thickness is directly linked to the parameters of concentration and spin speed (see legend in the graph).

4.1.2. X-ray Reflectivity Results of Double Layer Films

The possible stack combinations CA-PS, PS-CA, CA-PVK and PVK-CA with the preparation conditions in table 4.2 were produced twice. Again thermally oxidized silicon wafers were used as substrates. The build-up is plotted in figure 4.3 and the preparation conditions are specified in table 4.2.

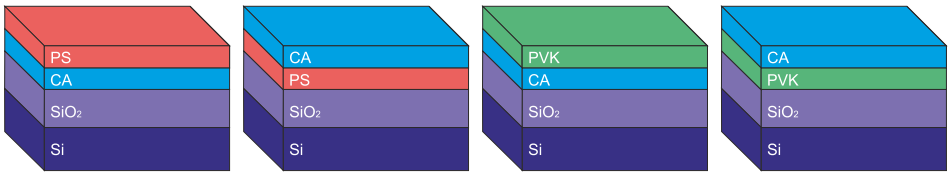

Figure 4.3.: Polymer double layer samples. CA-PS, PS-CA, CA-PVK and PVK-CA.

Table 4.2.: Spin conditions of the double layer films with conc., the polymer solution concentration and speed, the spin velocity.

	conc. (g/l)		speed (rps)	
CA-PS	PS:	32	PS:	180
	CA:	27	CA:	180
PS-CA	PS:	32	PS:	180
	CA:	27	CA:	180
CA-PVK	PVK:	24	PVK:	50
	CA:	27	CA:	180
PVK-CA	PVK:	24	PVK:	50
	CA:	27	CA:	180

The samples were of good quality and appeared homogeneous without any defects. All the samples were analyzed with XRR. The result of the sample CA-PS 1 is plotted in figure 4.4. Compared to the single layer graphs of figure 4.2, there seems to be overlaying fringes with different oscillations. The frequencies of the oscillations are related to the layer thicknesses. The Fourier transform reveals four peaks. The first peak at ≈90 nm is related to the CA layer, the second to the PS layer, the peak at 150 nm belongs to the oxidized silicon layer and the last peak is the sum of the CA and PS layer. The fitting exhibit following film thicknesses: d_{CA}=91 nm and d_{PS}=100 nm. Neglecting the peak of the oxidized silicon layer, the pattern of three peaks, with the third as a sum of the first and second, is typical for a double layer film.

The results of the fitting parameters of all samples are listed in table 4.3. The electron density fits to the single layer results of table 4.1. The thicknesses varies compared to

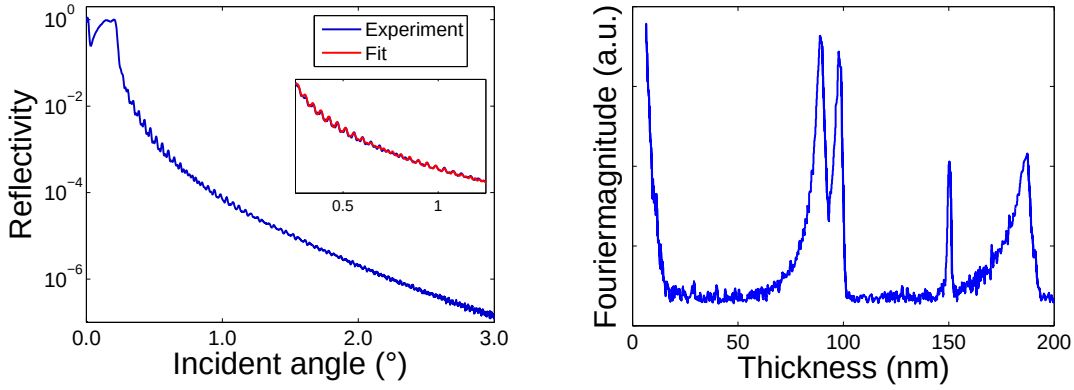

Figure 4.4.: XRR graph of CA-PS 1 (left). The fit matches with the data superior. Fourier transform of the XRR curve (right). The peaks belong to the film thicknesses within the sample.

the single layer films. For CA we would expect, under the chosen preparation conditions, a thickness of about 60 nm but obtain 90 nm. Commonly known, same polymer solution always tend to different results depending on their daily mood. The surface roughness, again, is marginal for each polymer (σ_{sf} ≈0.50 nm). The interface between the two polymers is perfectly flat (σ_{if} ≈1 nm). For photons in the visible range ((380-700) nm) the dimension of interface roughness is negligible.

Table 4.3.: XRR results on double layer films with $\rho_{bottom,top}$, the density of the first and the second applied layer, $d_{bottom,top}$, the thickness of the first and second applied layer and $\sigma_{if/sf}$ the polymer-polymer interface roughness and the surface roughness.

	ρ_{bottom} (g/cm^3)	ρ_{top} (g/cm3)	d_{bottom} (nm)	d_{top} (nm)	σ_{if} (nm)	σ_{sf} (nm)
CA-PS 1	1.33	0.96	91	100	1.05	0.41
CA-PS 2	1.33	0.96	93	101	1.04	0.41
PS-CA 1	1.10	1.30	97	86	0.99	0.45
PS-CA 2	1.08	1.24	97	92	0.82	0.47
CA-PVK 1	1.32	1.15	94	109	1.06	0.51
CA-PVK 2	1.32	1.08	94	108	1.06	0.53
PVK-CA 1	1.17	1.24	108	94	0.8	0.48
PVK-CA 2	1.21	1.23	106	91	1.12	0.52

For the samples PS-CA 1, CA-PS 1, CA-PVK 1 and PVK-CA 1 the positions of the critical angles of the materials were calculated out of the fit parameter of the electron density of

table 4.3 with equation 3.2, equation 3.7 and equation 3.13 and highlighted in the XRR plots in figure 4.5. At the first sight, the graphs consist of two critical angle at α_{c1}=0.16 ° and α_{c2}=0.22 °. The critical angel at 0.22 ° is related to the silicon substrate. The critical angle of the oxidized silicon and the pure silicon are nearly indistinguishable. The critical angle at α_{c1} =0.16 ° is a combination of both polymers. The critical angles of the polymers are so close, that they are not resolvable.

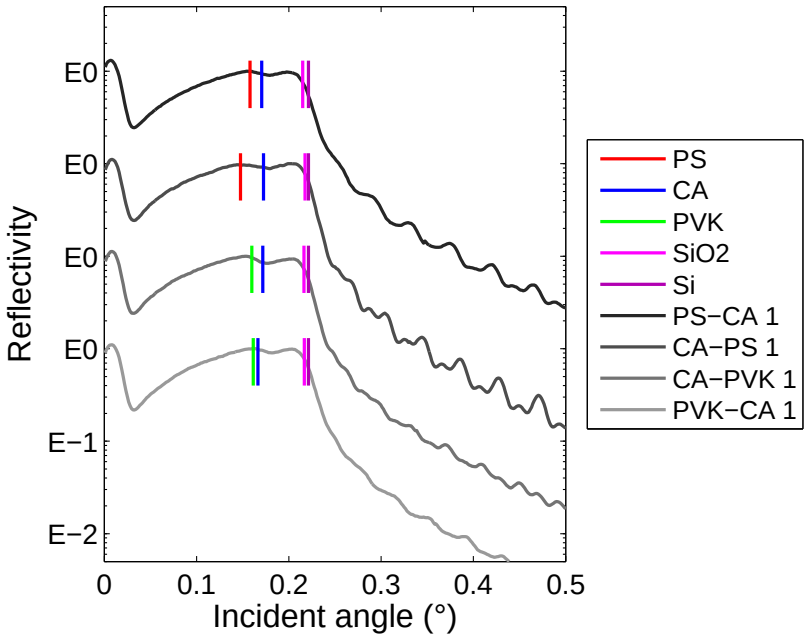

Figure 4.5.: Critical angles of the materials CA, PS, PVK, SiO_2 and Si within the XRR plot of the samples PS-CA 1, CA-PS 1, CA-PVK 1 and PVK-CA 1. The critical angles were calculated out of the electron densities of table 4.3 with 3.2, equation 3.7 and equation 3.13.

4.1.3. Heating of the Double Layer Films

The samples PS-CA 1 and CA-PS 1 were thermal treated as described in chapter 3.1. The XRR curves of the temperature cycles are plotted in figure 4.6. The reflectivity is scaled to one and for a better view all the graphs were plotted vertically shifted. At first glance there is no great change in the critical angle nor in the decline of the graphs.

In figure 4.7 on the left row the XRR plots of the sample CA-PS 1 (the sample PS-CA 1 looks the same) are zoomed in at the critical angle, the fringes and the slope. The closer

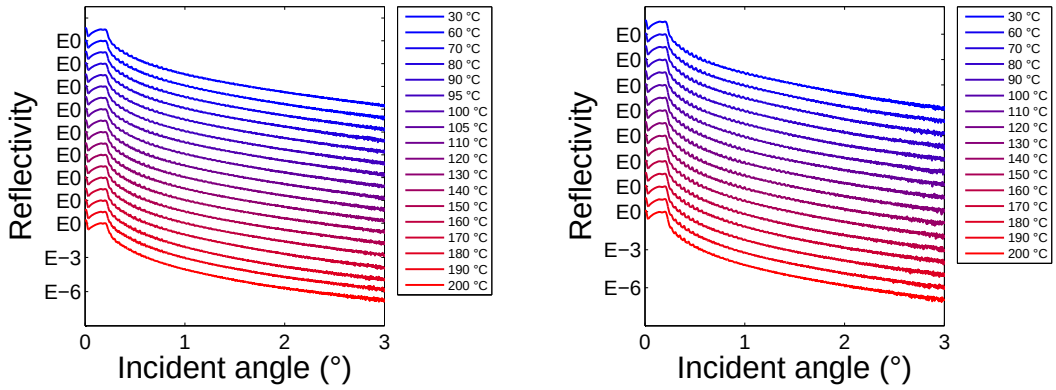

Figure 4.6.: XRR curves during thermal treatment of the samples PS-CA 1 (left) and CA-PS 1 (right).

look reveals, that the critical angle indeed stayed constant, the fringes enlarged and the slope increased during the thermal treatment. The change of the fit parameters of CA-PS 1 and PS-CA 1, that are linked to the plotted parts of the XRR scans are represented in figure 4.7 on the right row.

As proclaimed, the density, which belongs to the critical angle, did not change during the thermal treatment. The thickness, which is related to the fringes, was decreasing and the non reversible loss of the sample is mainly caused by the effect of the CA. The PS is stable up to 170 °C. O. Werzer et al. examined already, that the change of thickness of thin polymer layer due heating can be seen in the change of the Kiessig fringes [32]. The increase of the decline was caused by the expanding interface roughness. The surface roughness of CA-PS 1 and PS-CA 1 was ≈0.4 nm during the entire thermal treatment procedure. The interface roughness stayed up to 170 °C at ≈1 nm. Up to 200 °C it increased to ≈2 nm. This result is quit interesting, since even for temperatures larger than the polymers glass transition temperature (110 °C for PS and 130-190 °C for CA, respectively), the quality of interfaces and thicknesses control is retained. This result suggests that in confined structures the thermal properties of polymers are modified with respect to the bulk as recently shown for core-shell microspheres used for the preparation of polymer photonic crystals [53].

The thickness at the temperature steps in relation to the thickness without temperature treatment will be called dilatation. The dilatation of PS and CA of the samples CA-PS 1 and PS-CA 1 are plotted in figure 4.8. The CA layer thickness decreased up to 8 % especially when the CA was applied on top.

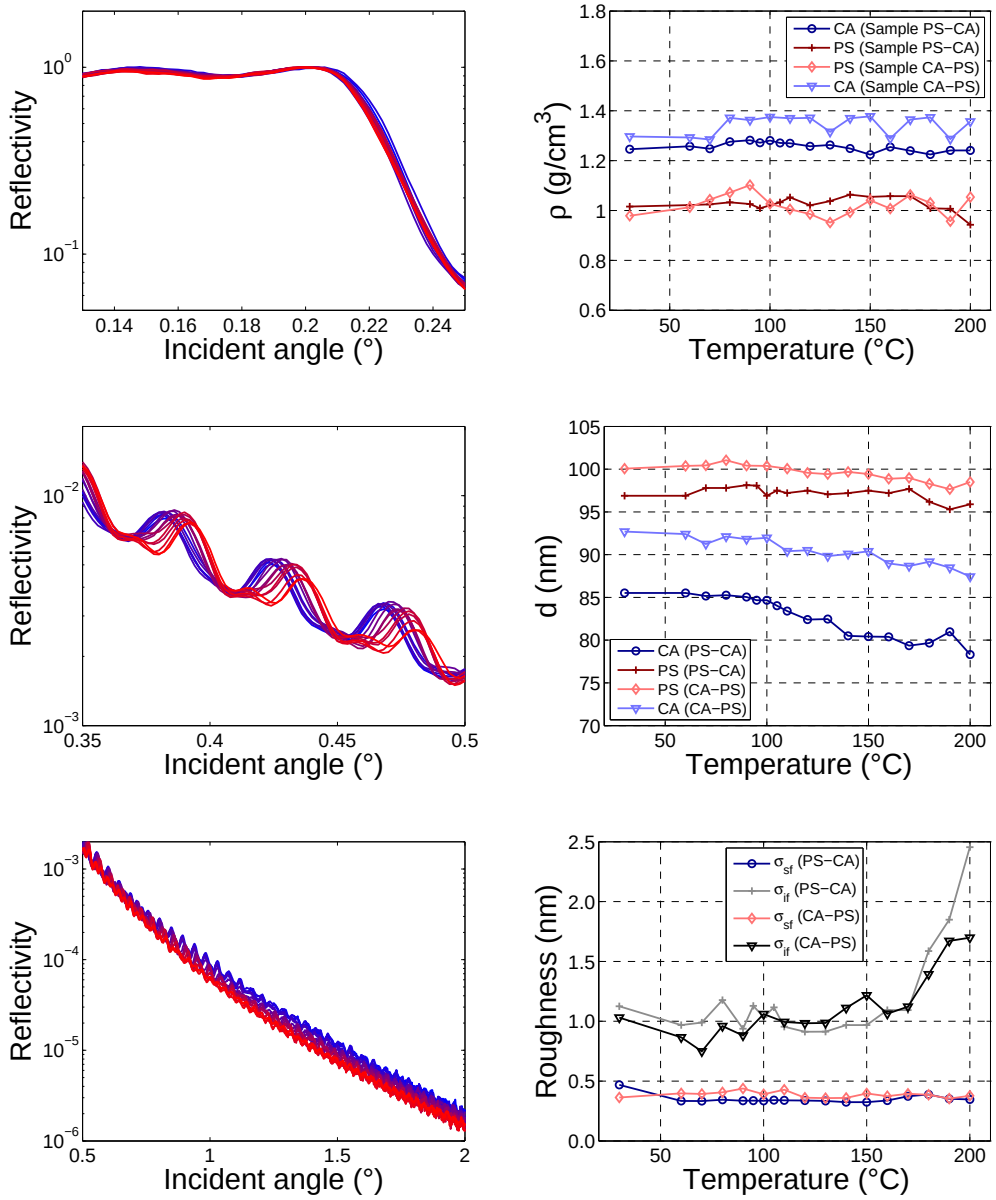

Figure 4.7.: XRR plots of the sample CA-PS 1 zoomed in at the critical angle (top-left), the fringes (middle-left) and the slope (bottom-left). The colors of the XRR curves are related to the temperature likewise in figure 4.6 with blue: 30 °C to red 200 °C.
Fitting parameters of the XRR curves of the samples CA-PS 1 and PS-CA 1. The mass density (top-right), the thickness (middle-right) and the surface and polymer-polymer interface (bottom-right).

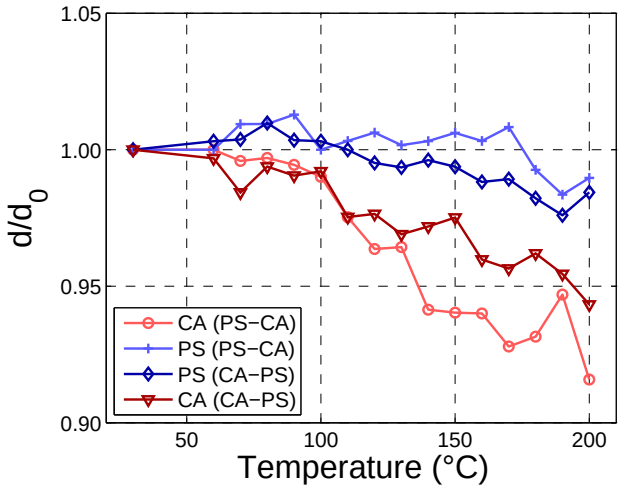

Figure 4.8.: Dilatation of CA and PS layers of the samples PS-CA 1 and CA-PS 1 after heating.

4.1.4. Spectroscopic Ellipsometry Results of Double Layer Films

The samples CA-PS 2, PS-CA 2, CA-PVK 2 and PVK-CA 2 were examined with spectroscopic ellipsometry. The phase difference Δ and the inverse tangent of the ratio of the reflection coefficients of the TE and the TM polarization Ψ of the sample CA-PS 2 are plotted in figure 4.9. The peak pattern in Ψ is a typical features of layered samples. As represented in figure 4.9 (right), the results of the angle Δ appear to be very discontinuous but this is just a method for an illustration of an angle without exceeding the range of 360 °. In fact Δ is continuous.

The fit matches with the data of Δ and Ψ well. The obtained refractive index N=n+iκ is plotted figure 4.10. In the visible spectrum the refractive index of the CA and PS layers is flat. The complex part κ of the refractive index is in the visible spectrum zero for CA and PS. The polymers do not absorb visible light. At about 230 nm κ increases slightly. The CA and PS gets optical active in the UV range of the spectrum.

The fitting routine worked well with the samples CA-PS 2 and PS-CA 2. In table 4.1.4 the fit parameters of the thickness and of the refractive index at λ =598 nm is listed. In the factsheets of CA and PS, provided by *SigmaAldrich*, the refractive index at λ =598 nm is cited [49, 50]. The refractive index of CA n_{CA}=1.482 (in the sample PS-CA 2) and n_{CA}=1.478 (in the sample CA-PS 2) are matching with the factsheet data of n_{CA}=1.475.

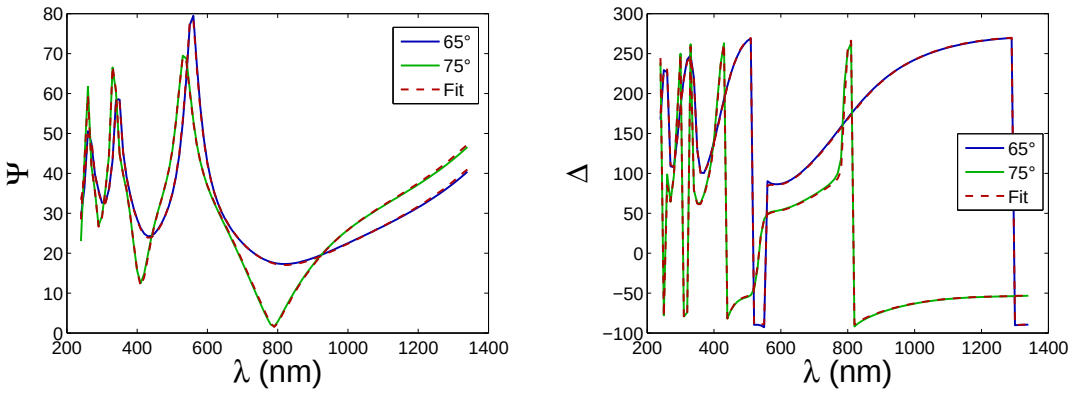

Figure 4.9.: Δ and Ψ graphs of CA-PS 2. The blue and the green line represent an incident angle of 65 ° and 75 °. The red dashed line is the fit.

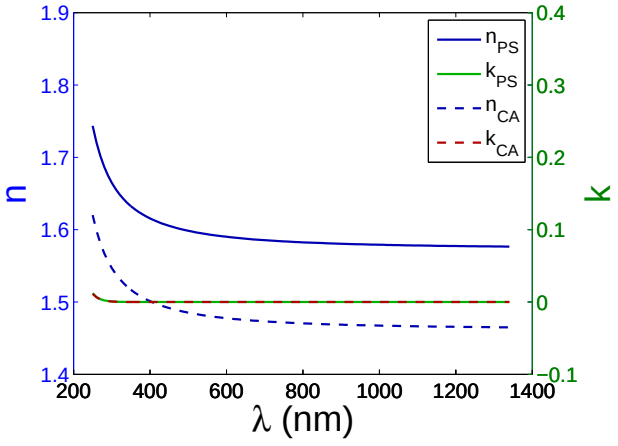

Figure 4.10.: Real and complex part of the refractive index N=n+iκ of the CA and PS layer of the sample CA-PS 2.

The refractive index of PS n_{PS}=1.589 (in the sample PS-CA 2) and n_{PS}=1.591 (in the sample CA-PS 2) is also in good accordance with the fact sheet data of n_{PS}=1.59. The refractive index in terms of λ of CA and PS of CA-PS 2 and PS-CA 2 are averaged and plotted in figure 4.11.

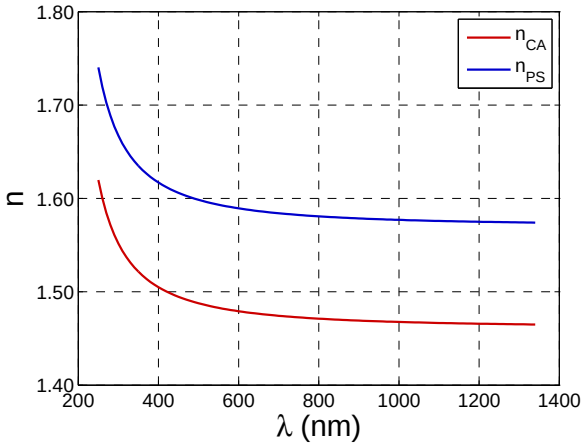

Figure 4.11.: Refractive index of CA and PS determined with spectroscopic ellipsometry.

The result of CA-PVK 2 is represented in figure 4.12. The fit has some problems with mapping the data in the UV range. PVK has a complex absorption behavior in the UV and the fitting technique described in chapter 3.3 is not sufficient. The fitting parameters of the refractive index in figure 4.12 and the double layer thickness in table 4.1.4 are non-credibly.

Summarizing, the fitting results of the CA-PS 2 and PS-CA 2 samples are satisfying but of the samples CA-PVK 2 and PVK-CA 2 just the visible region was correctly fitted.

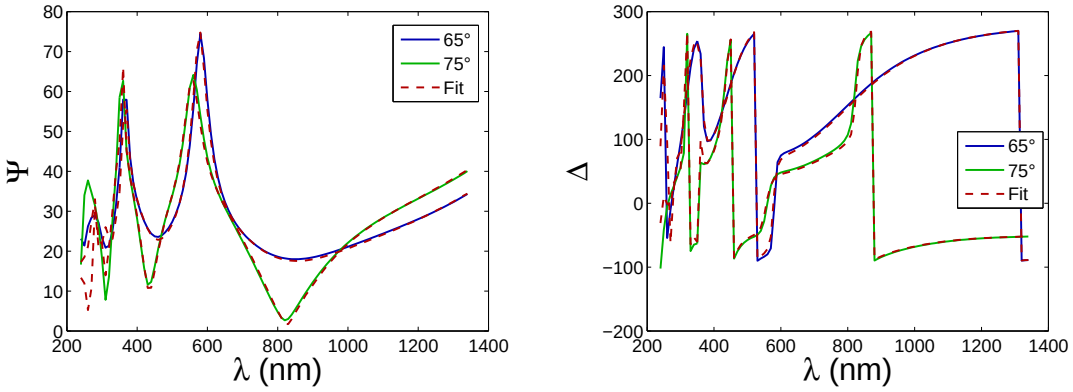

Figure 4.12.: Δ and Ψ graphs of the CA-PVK 2 sample. The blue and the green line represent an incident angle of 65 ° and 75 °. The red dashed line is the fit. In the UV range the fit does not match with the data.

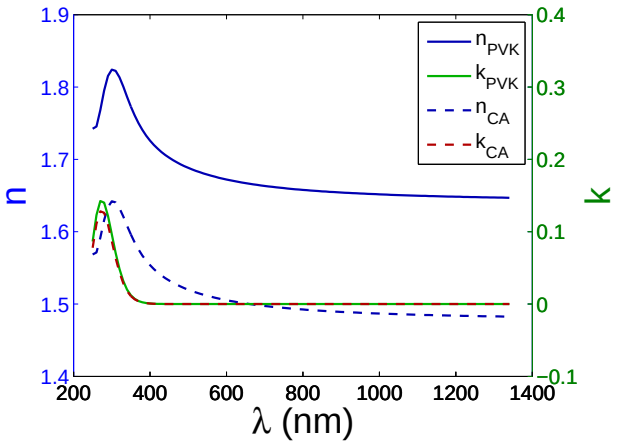

Figure 4.13.: Real and complex part of the refractive index N=n+iκ of the CA and PVK layer of the sample CA-PVK 2.

Table 4.4.: Spectroscopic ellipsoemtry results of the samples PS-CA 2, CA-PS 2, CA-PVK 2 and PVK-CA 2: measured real part of the refractive index at λ=589 nm compared to the literature data [49–51] and double layer thickness.

PS-CA 2		
	experiment	literature
n_{PS}	1.589	1.59
n_{CA}	1.482	1.475
D (nm)	190.3	

CA-PS 2		
	experiment	literature
n_{CA}	1.478	1.475
n_{PS}	1.591	1.59
D (nm)	195.9	

CA-PVK 2		
	experiment	literature
n_{CA}	1.560	1.475
n_{PVK}	1.673	1.696
D (nm)	201.5	

PVK-CA 2		
	experiment	literature
n_{PVK}	1.680	1.696
n_{CA}	1.430	1.475
D (nm)	188.6	

4.1.5. Results of Atomic Force Microscopy

AFM images of the surface of the samples PS-CA 2, CA-PS 2, CA-PVK 2 and PVK-CA 2 with the resolution of (10×10) are plotted in figure 4.14. The surface roughness, the lateral correlation length and the Hurst parameter are listed in table 4.5. The CA layer had got the highest surface roughness with (0.80±0.30) nm in the PS-CA configuration and (0.65±0.15) nm in the PVK-CA configuration. The PS had got a small surface roughness of (0.30±0.05) nm likewise the PVK with (0.35±0.05) nm.

Table 4.5.: Surface roughness σ_{rms}, lateral correlation length ξ and Hurst parameter α of the double layer samples determined by atomic force microscopy.

	σ_{rms} (nm)	ξ (nm)	α
PS-CA 2	0.80 ± 0.30	120 ± 50	0.55 ± 0.05
CA-PS 2	0.30 ± 0.05	120 ± 20	0.50 ± 0.00
CA-PVK 2	0.35 ± 0.05	130 ± 20	0.50 ± 0.00
PVK-CA 2	0.65 ± 0.15	130 ± 30	0.55 ± 0.05

The CA surface had not only some circular protrusions but also azimuthally not oriented needle-shape structures. A more detailed analysis of these structures were made by line profiles, figure 4.15. Eight needle structures and five grains were averaged:

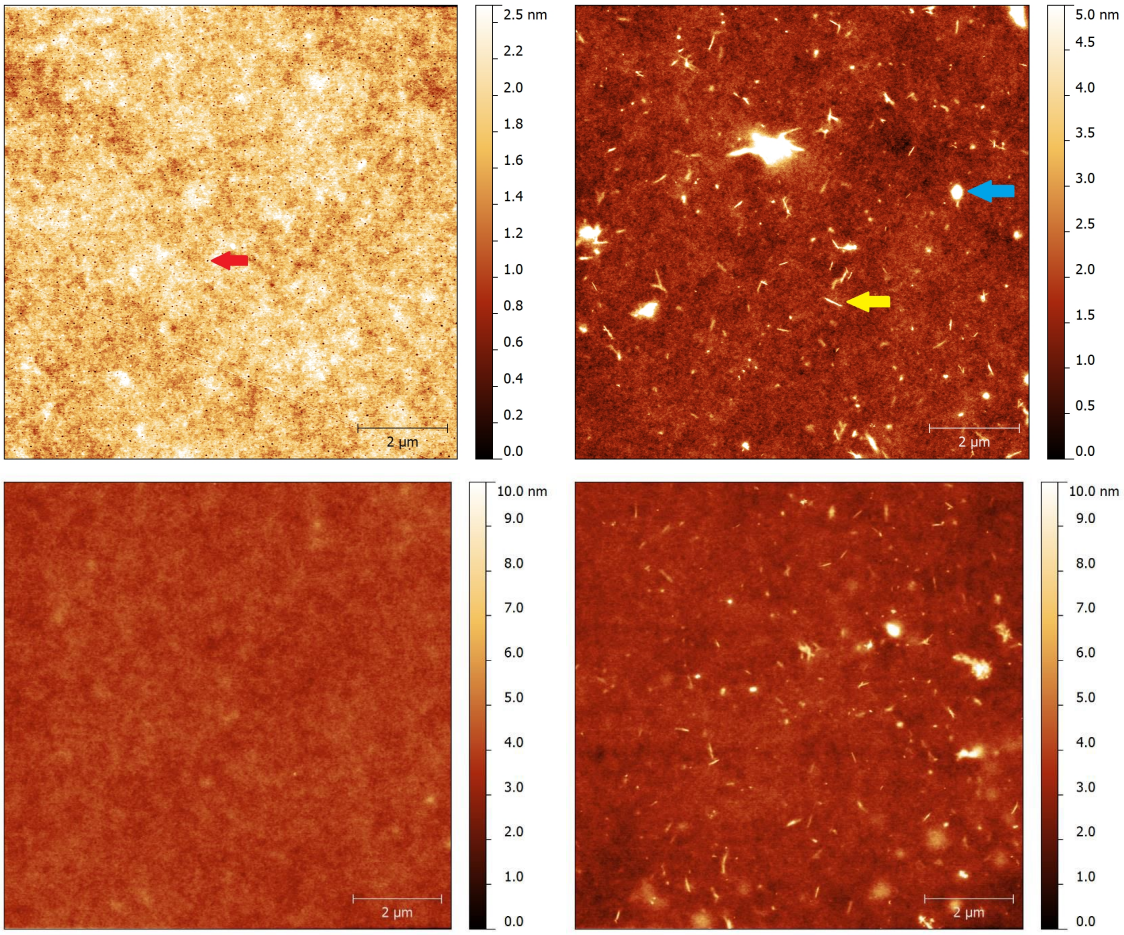

Figure 4.14.: (10×10) µm^2 AFM images of the samples CA-PS 2 (top-left), PS-CA 2 (top-right), CA-PVK 2 (bottom-left) and PVK-CA 2 (bottom-right). The arrows are marking representative surface structures (yellow - needle, blue - protrusion, red - hole).

$CA_{needles}$	length	(415±80) nm
	width	(130±60) nm
	hight	(4±3) nm
CA_{grains}	width	(185±35) nm
	hight	(8±3) nm

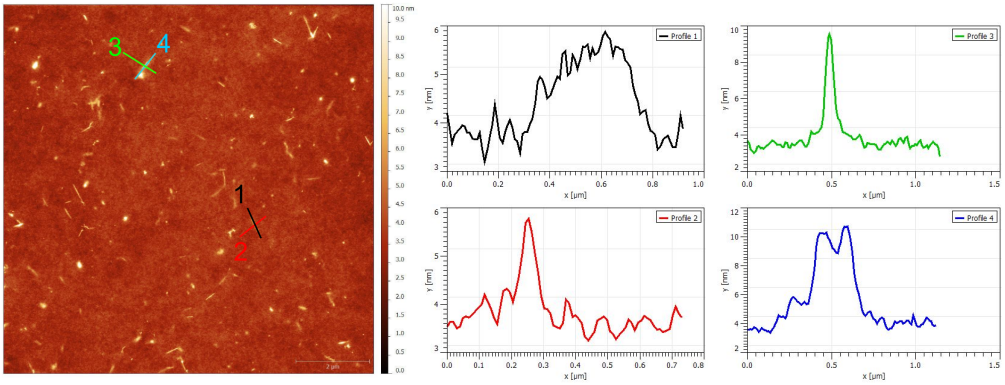

Figure 4.15.: Line profile analysis of the sample PS-CA 2.

The PS surface contained arbitrary distributed circular holes, although it is very smooth when compared to the other surfaces, see table 4.5. Thirteen line profiles were taken and averaged. In figure 4.16 some of them are shown.

PS_{holes}	width	(45±5) nm
	depth	(2±1) nm

The surface of the PVK-CA 2 looked similar to that of PS-CA 2. On both samples the CA is on top. There occurred no difference in the CA surface whether PS or PVK was applied first. Six line profiles for the needle-shapes and four line profiles for the grains were averaged:

$CA_{needles}$	length	(350±60) nm
	width	(100±25) nm
	hight	(5±2) nm
CA_{grains}	width	(265±95) nm
	hight	(4±2) nm

The surfaces are compared to the wavelength of visible light ((380-700) nm) very smooth.

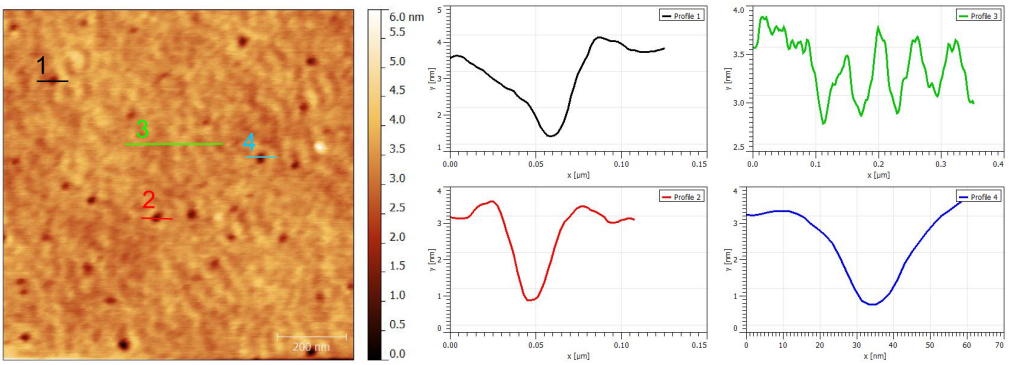

Figure 4.16.: Line profile analysis of the sample CA-PS 2.

4.1.6. Compared Results of X-ray Reflectivity, Spectroscopic Ellipsometry and Atomic Force Microscopy

With XRR and spectroscopic ellipsometry it was possible to examine the thickness of the polymer layers. With XRR the thickness of each layer was obtained. With spectroscopic ellipsometry only the sum of the two polymer layers was evaluated. Nevertheless this parameter can be compared with XRR, as shown table 4.6. For the samples PS-CA 2 and CA-PS 2 the results correspond well with deviations as low as 0.6 % (for PS-CA 2) and 1 % (for CA-PS 2).

As described in chapter 3.3, samples which contains PVK, are not fit-able, but for the sample CA-PVK 2 we only get a dissimilarity of 0.1 %. The accurateness could lead to the deceptive assumption, that the fit of the spectroscopic ellipsometry data is valid. But looking at table 4.1.4 you can see, that the refractive index of the sample CA-PVK 2 that was gained out of spectroscopic ellipsometry differ from those in the literature [49–51]. The deviation in the fitting parameters, the refractive index and the thickness, is so big, that you cannot rely on those results. For the sample PVK-CA 2 the thickness difference between the XRR and spectroscopic ellipsometry is (with 4 %) an insufficient result.

XRR and AFM provide the surface roughness (see table 4.3 and table 4.5). The results are listed in table 4.6. For the sample CA-PS 2 (with PS on top) the roughness is in good accordance. For PS-CA, the values are in the same order of magnitude. Because the grains and needles do not provide a normally distributed height function, we expect, that the AFM is more accurate. For the samples CA-PS 2 and CA-PVK 2 the surface roughness of the AFM is less than that of XRR. The position for each (10x10) µm spot was chosen to be without huge defects and grains so the expected surface roughness of these spots is smaller than the overall surface roughness.

Table 4.6.: Surface roughness σ_{sf} (gained out of AFM and XRR), and overall polymer thickness D (examined with spectroscopic ellipsometry and XRR).

	PS-CA 2		CA-PS 2		CA-PVK 2		PVK-CA 2	
	σ_{sf} (nm)	D (nm)	σ_{sf} (nm)	D (nm)	$\sigma_s$sf (nm)	D (nm)	σ_{sf} (nm)	D (nm)
AFM	0.80		0.35		0.30		0.65	
Ellispometry		190.3		195.9		201.5		188.6
XRR	0.47	189.2	0.41	193.8	0.51	201.2	0.52	196.9

4.2. Distributed Bragg Reflectors

In this section the optical response of a distributed Bragg reflector with increasing layer numbers will be investigated. Further the dependence of the spin preparation conditions on the bandgap will be evaluated. Transmission and reflection spectra will be presented.

4.2.1. Reflectance Versus Repeat Units

A multilayer sample based on a repeating PVK-CA double layer was prepared as described in chapter 3.5. For 1, 2, 5, 10 and 15 repeat units reflectance spectra were recorded, figure 4.17. Morandi et al. showed, that with increasing numbers of repeat units a bandgap arise [54]. The result agrees with the measured spectra. The $(\text{PVK-CA})_{15}$ DBR developed a bandgap at 580 nm with a reflectance of 94 %. This was the first produced DBR by me and, although the preparation needs to be practiced, the reflectance is impressively high. This indicates, that the spin casting technique provide good reproducible thicknesses. A photograph of $(\text{PVK-CA})_{15}$ is on the right side of figure 4.17. The DBR is not homogeneous and has lots of radial defects, which are called comet structures. The sample had to be taken out of the spin coater each time it had to be annealed and most likely it was exposed to a dusty air. It is a typical spin casting artifact, that dust particles or small impurities of the solution stick onto the surface and cause comet-like structures [55].

The color changes excessively from the middle to the outside. In the center a little defect cannot be avoided. When applying the solution of a new layer, the tip of the pipette slightly touch the center and cause the defect. The defects on the edges are also common known spin coating side effects. But the defects of especially samples which contain PVK cause a too high inaccuracy. For further DBRs PS was used instead of PVK to get rid of the annealing procedure and protect the sample from dust. With equation 2.53 the increase

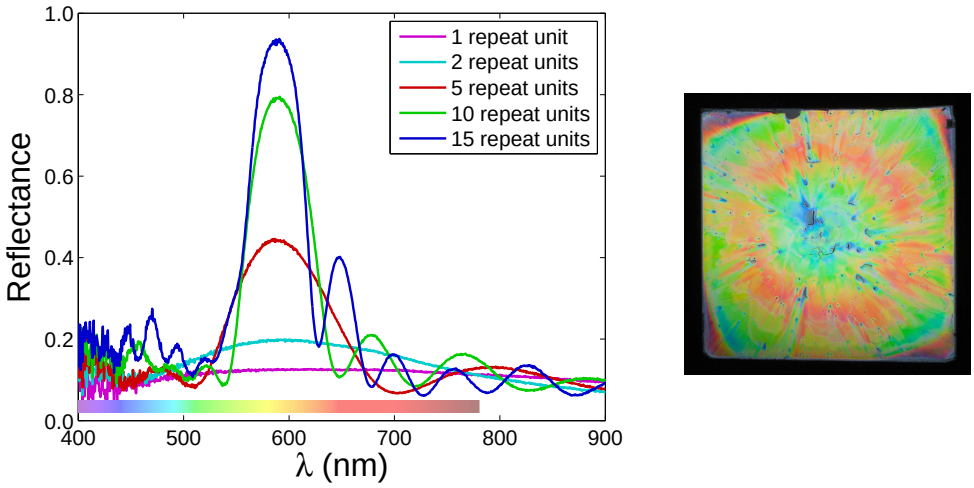

Figure 4.17.: Reflectance of $(PVK\text{-}CA)_X$ with 1, 2, 5, 10 and 15 repeat units (left) and photograph of $(PVK\text{-}CA)_{15}$ (right).

of the reflectance with the layer numbers can be calculated. The experimental and the calculated reflectance are in good agreement (figure 4.18).

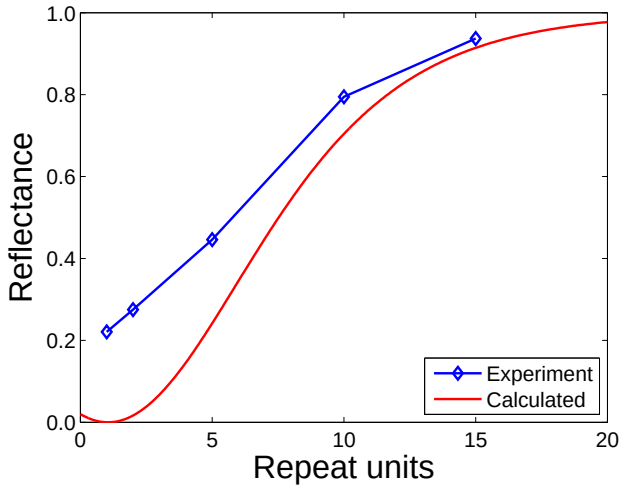

Figure 4.18.: Measured and calculated (equation 2.53) reflectance at the bandgap of $(PVK\text{-}CA)_X$ versus the repeat units.

4.2.2. Distributed Bragg Reflector Made of (PS-CA) Repeat Units

With the preparation conditions described in table 4.7 three (PS-CA)$_{20}$PS DBRs were produced as described in chapter 3.5. In figure 4.19 the reflectance spectra of the three DBRs, DBR1 DBR2 and DBR3, are plotted. By use of different preparation conditions for each DBR, the bandgap could be produced at a different wavelength λ. The bandgaps are at λ_{DBR1}=480 nm, λ_{DBR2}=598 nm and λ_{DBR3}=780 nm. The reflectance is approximately 70 %, which is less compared to (CA-PVK)$_{15}$ in figure 4.17. The difference between the refraction index of CA and PVK is higher than the difference between CA and PS. Larger difference of refraction index enhance the reflection [26].

The DBRs look satisfying. Each has a small center defect and just few comet structures. The homogeneous area between the center and the boarder is large and sufficient for further measurements.

Table 4.7.: Preparation condition of the three (PS-CA)$_{20}$PS DBRs.

	Material	concentration (g/l)	spin speed (rps)
DBR1	CA	20	110
	PS	22	110
DBR2	CA	27	150
	PS	32	150
DBR3	CA	27	90
	PS	32	90

With higher spin velocity and lower polymer solution concentration thinner layers were obtained. The layer thickness is -via equation 2.52- related to the bandgap. DBR1 was produced with a low concentration and an intermediate spin speed. The resulting bandgap admits the assumption, that the thickness of the repeat unit is the smallest for the three DBRs. DBR2 was produced with standard concentration and a high spin velocity. The bandgap is placed in between the gap of DBR1 and DBR2. DBR3 has its first order bandgap at the beginning of the infrared spectrum. It was produced with a low spin velocity and with standard concentration.

In the spectrum of DBR3 at λ=398 nm a second peak arise. This is the second order bandgap. It is easy to determine the order of a bandgap. If the refractive index of the materials is flat in the visible spectrum, the ratio of the bandgap positions follows the series: 1, $\frac{1}{2}$, $\frac{1}{3}$, $\frac{1}{4}$,... . DBR3's gaps are at λ=780 nm and λ=398 nm. The peaks can be identified as first and second order bandgap. The ratio of $\frac{1}{2}$ is not completely fulfilled but as we have

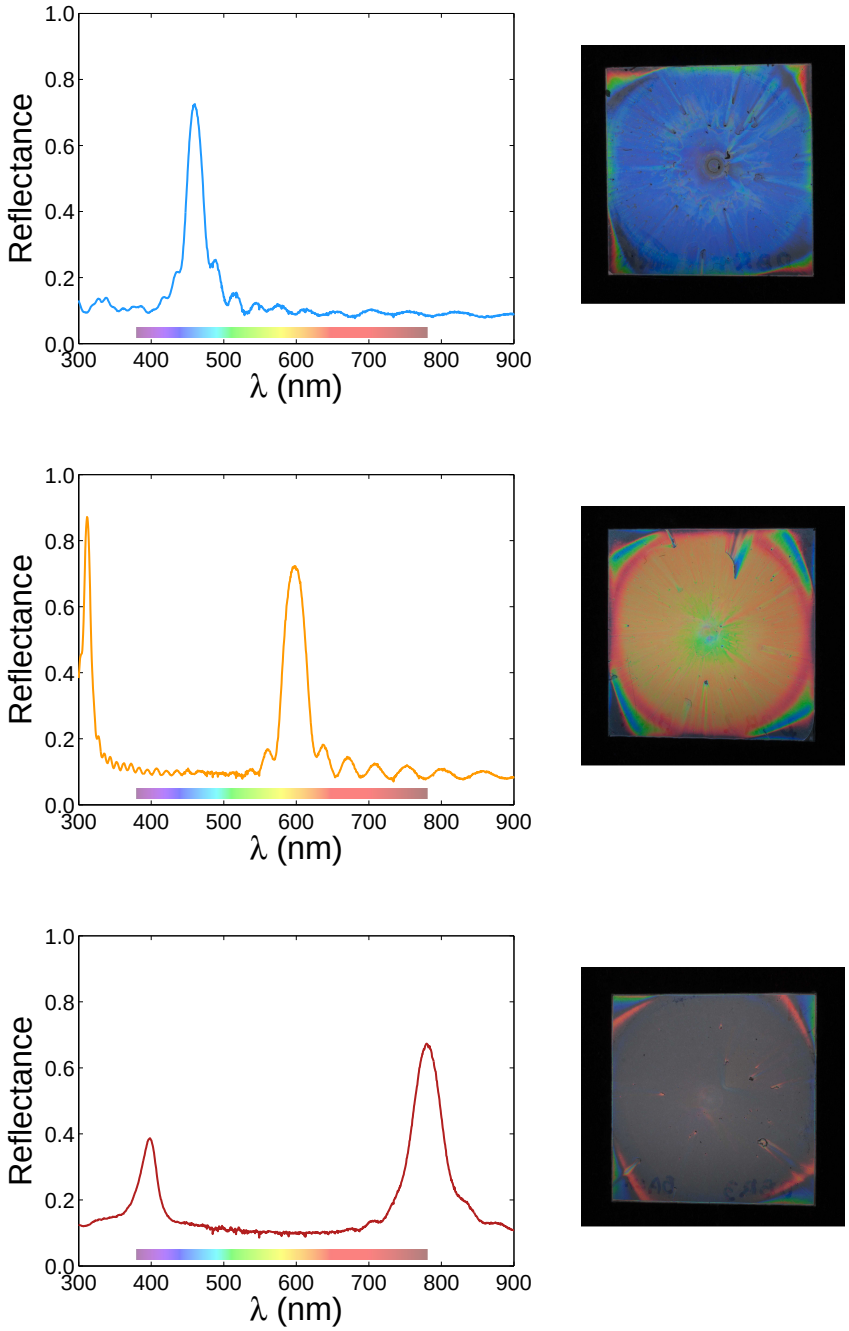

Figure 4.19.: Reflectance spectra and photographs of DBR1 (top), DBR2 (middle) and DBR3 (bottom), each a $(PS\text{-}CA)_{20}PS$, produced with different preparation conditions listed in table 4.7.

already seen in chapter 4.1.4, the refractive index of CA and PS is not completely constant in the visible region.

The transmission spectra of DBR1, DBR2 and DBR3 are plotted in figure 4.20. The photographs on the right show the same DBRs as in figure 4.19 but this time in transmission. The DBRs have been illuminated from behind, allowing us to see their transmission color. The sum of the reflection and transmission spectra has to be 100 % if the material is not active. Therefor the color of the photographs of reflection is the additive complementary color to the color of the photographs of transmission. For DBR1 the color of reflection is c_r=blue and the color of transmission is c_t=yellow. These are additive complementary colors. The same is true for DBR2: c_r=orange c_t=cyan and for DBR3: c_r=red/infrared c_t=transparent.

In equation 2.52 the therm effective refractive index is needed to calculate the thicknesses of the layers. Also the ratio between the thickness of CA and the PS layer is necessary. But there is no direct access to this parameter. In the chapter 4.3.1 it will be explained, how to solve this issue.

After a time period of one month the spectra of DBR1, DBR2 and DBR3 was recorded again. For each DBR the bandgap moved to lower λ. The shift of $\lambda_{Gap}$was most likely caused by a shrinking of the layers. The gap of the DBR1 shifted from 456 nm to 447 nm, the gap of DBR2 from 608 nm to 581 nm and for DBR3 from 804 nm to 760 nm. This shift is shown in figure 4.21.

Summarizing, the three DBRs were of good quality and have nice bandgaps. The concentration of the solution had an huge impact on the position of the bandgap, likewise the spin velocity. With changing these parameter, bandgaps in a wide range can be produced.

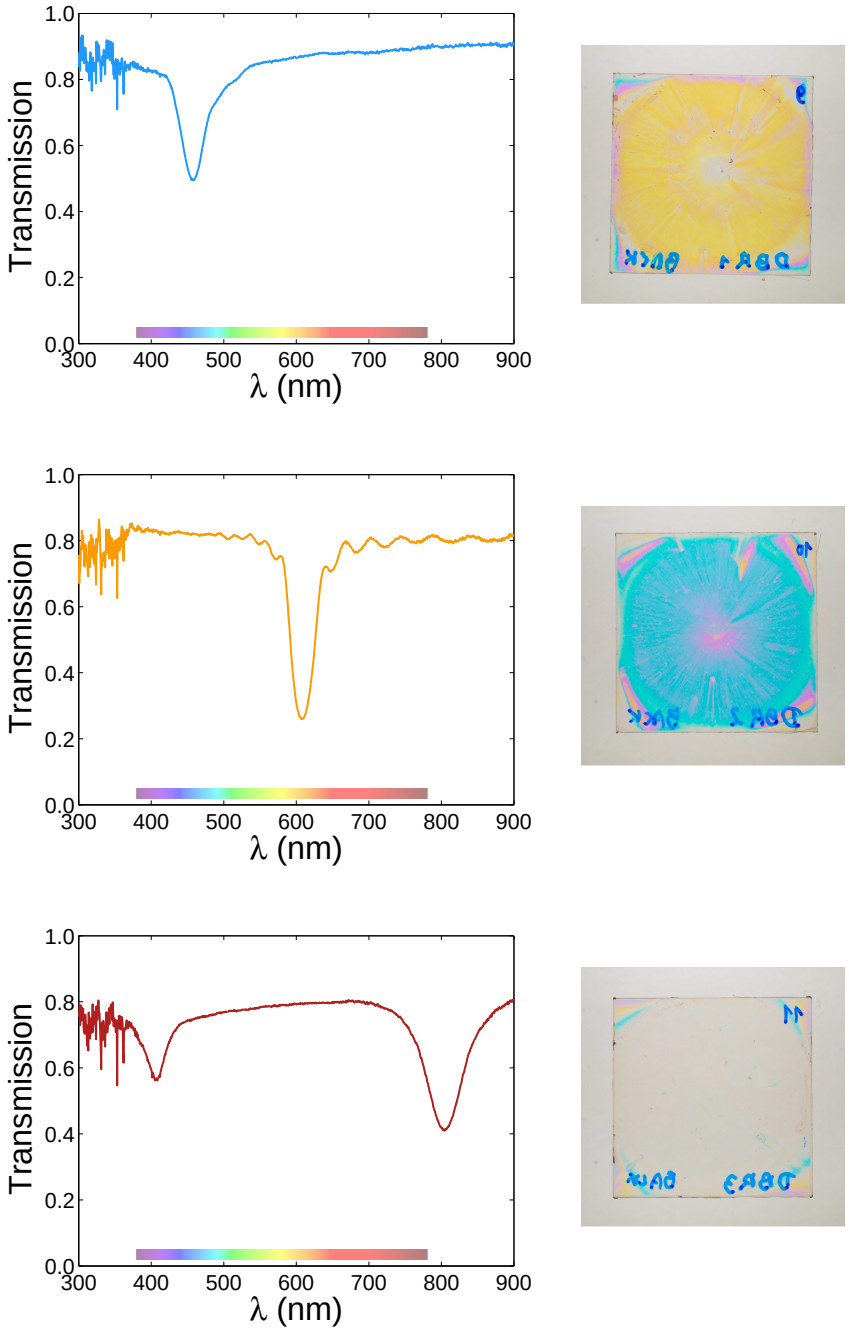

Figure 4.20.: Transmission spectra and photographs of DBR1 (top), DBR2 (middle) and DBR3 (bottom), each a $(PS\text{-}CA)_{20}PS$, produced with different preparation conditions listed in table 4.7.

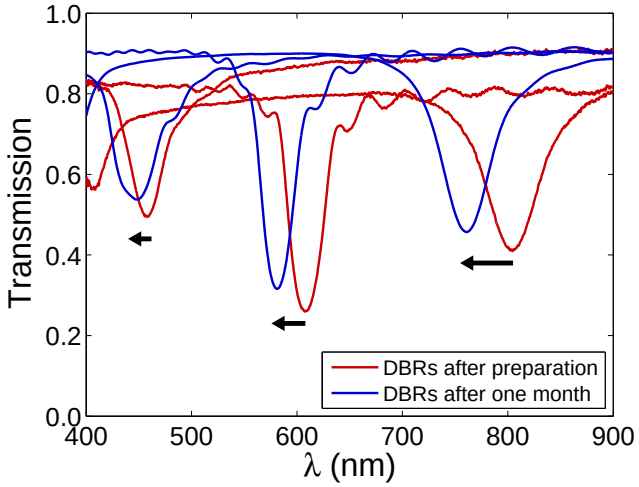

Figure 4.21.: Transmission spectra of DBR1, DBR2 and DBR3 taken after preparation and one month later.

4.3. Simulation of spectra

In the following the layer thickness of the presented distributed Bragg reflectors will be determined. With the obtained parameters simulated spectra will be introduced and compared to the experiment. Further the standard deviation of the layer thickness will be evaluated as an additional parameter for the simulation.

4.3.1. X-ray Reflectivity to Access the Layer Thickness of Distributed Bragg Reflectors

The layer thickness of DBR1, DBR2 and DBR3 cannot be determined out of the spectra. Therefore double layer samples D1, D2 and D3 on silicon substrates with the same solution concentration and the same spin conditions were produced. The samples were examined with XRR and the obtained thicknesses are listed in table 4.8.

If the PS is applied first the thickness is 4 % lower compared to the thickness when PS is applied secondly. This also occurs for CA but only with a difference of 2 % In the last column of the table the sum of CA and PS thickness (when secondly applied) and the ratio of thickness is listed. The PS layer is for all samples twice as thick as the CA layer. The overall thickness from D1 to D3 is increasing, confirming our measurements from chapter 4.2.2. The thicknesses, gained by the second applied layer, will be used as

Table 4.8.: Thicknesses of the double layer samples DL1, DL2 and DL3 measured with XRR.

	PS-CA		CA-PS			
	d_{PS} (nm)	d_{CA} (nm)	d_{CA} (nm)	d_{PS} (nm)	D (nm)	CA:PS
DL1	88.0	46.0	45.8	95.0	141.0	1:2.07
DL2	124.8	62.1	65.7	126.4	188.5	1:2.04
DL3	170.5	83.9	85.0	174.9	258.8	1:2.08

a repeat unit to simulate DBR1, DBR2 and DBR3 by use of the transfer matrix method explained in chapter 2.3.3. A visualization of the repeat units is presented in figure 4.22. For the simulation the refractive index of PS and CA is taken out of the data of figure 4.11. The glass substrate has a thickness of 0.2 mm and a refractive index of n=1.33.

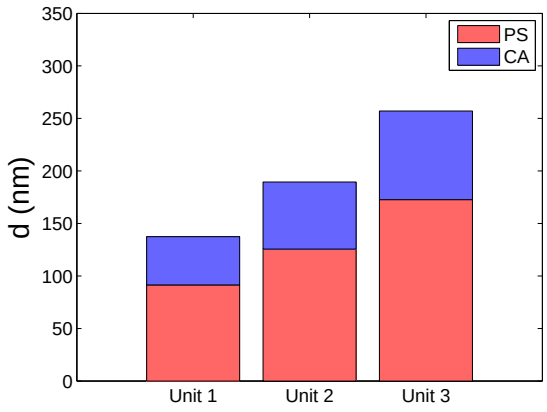

Figure 4.22.: Measured layer thicknesses of the repeat units of DBR1, DBR2 and DBR3.

The results of the simulation of DBR1, DBR2 and DBR3 are plotted to the experimental spectra in figure 4.23. The bandgap position of the simulated DBR1 (top) and DBR2 (middle) is comparable to the measured spectra. The gap positions of DBR1 matches with a high accuracy ($\Delta\lambda$=0.6 nm). For DBR2 it is slightly off ($\Delta\lambda$=6 nm) but still in good accordance. For DBR3 the simulation is not in good agreement with the experiment ($\Delta\lambda$ =40 nm). The effective refractive index of DBR3 (equation 2.52) is at at the wavelength of 763 nm equals 1.546(requiring, that at least the ratio of thickness CA:PS (see table 4.8) is preserved). The thickness of the repeat unit of DBR3 -calculated out of the bandgap position with equation 2.52- is 246.8 nm. But the thickness of the DL3 sample is 258.8 nm (see table 4.8). The reason of this offset of 13 nm is undefined. The DL3 sample is not representing a repeat unit of DBR3.

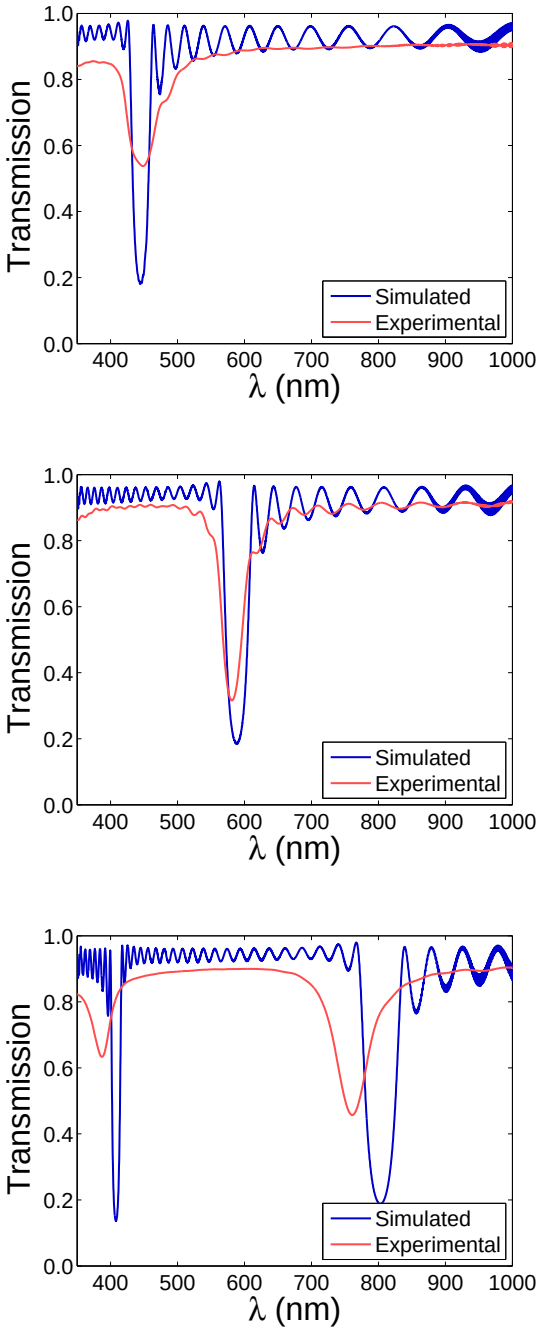

Figure 4.23.: Simulated an experimental spectra of DBR1 (top), DBR2 (middle) and DBR3 (bottom). The position of the bandgap of the simulation is correct for DBR1 and DBR2.

All simulated spectra contain additional fringes. The fringes beside the bandgaps are due the reflection on the surface and on the glass substrate. The small fringes in the infrared region are caused by the thick glass substrate. In the experimental spectrum the fringes are smeared out. Only in the spectrum of DBR2 fringes are slightly observable. The loss of the fringes may be caused by a variation of layer thickness along the depth. Likewise the light spot of the spectrometer ((4×4) mm) screens areas of different over-all DBR thickness. The pronounced gap and the fringes get less. In the next chapter we will examine the effect of the variation of thickness on DBR spectra.

4.3.2. Variation of Layer Thickness in a Distributed Bragg Reflector

A spectrum of a DBR does not match accurate with a simulated one. The gap and the fringes in the spectrum of a DBR gets diluted. It has already been examined, that scattering processes due defects decrease the intensity of the signal and a variation in the thickness lead to diluted fringes [27]. This chapter will examine the deviation of thickness in order to explain the cause of the loss of the efficiency and the fringes. The thickness can variate randomly, as illustrated in figure 4.24 on the left. The thickness can also tend to increase monotonic shown in figure 4.24 on the right. The spin casting technique induce the assumption of a radial dependency of the thickness.

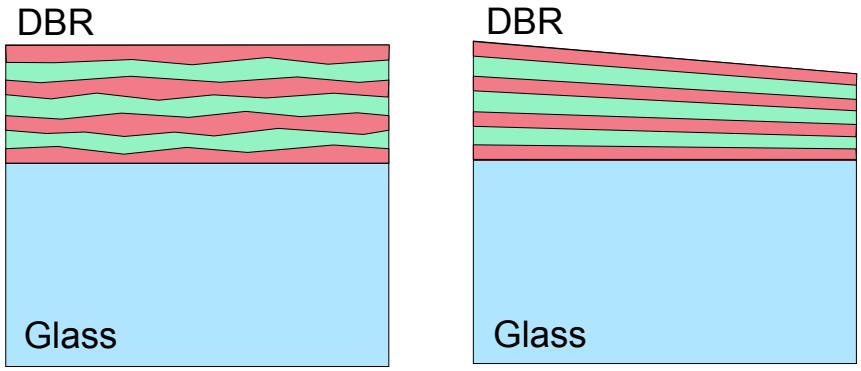

Figure 4.24.: DBR with a random variation of layer thickness (left) and a monotone decrease of layer thickness (right).

To measure the variation of thickness, 9 double layer samples PS-CA and CA-PS were produced with dynamical spin casting technique on thermally oxidized silicon. The reason for producing double layer samples was to exclude the wetting behavior of the substrate and to measure the second layer thickness of several samples. The polymers standard

concentrations were used (c_{CA}=27 g/l and c_{PS}=34 g/l). The spinspeed for each layer was 100 rps and the applied volume was 100 µl. Each of these samples were analyzed with XRR to obtain the thickness of each layer. The averages and the standard deviations (for the second applied layer) are:

$$d_{CA} = (131 \pm 2)\,\text{nm}$$
$$d_{PS} = (72 \pm 1)\,\text{nm}$$

The mean thickness is similar to the thickness of DBR2. The variation of thickness observed is presumably the same for DBR2. The relative standard deviation therefore is s_{CA}= 1.9 % and s_{PS}= 1.6 %. Additional the thickness variation is caused by the interface roughness. The average interface roughness between a PS and CA layer (gained out of table 4.3) is (1±0.1) nm. For DBR2 the standard deviation of thickness is:

$$\text{SD}_{CA} = 2.3\,\text{nm}$$
$$\text{SD}_{PS} = 3.0\,\text{nm}$$

DBR2 was simulated with a Gaussian distributed random thickness with the mean thicknesses of DL2 (see table table 4.8) and the evaluated standard deviation. 100 spectra were averaged and plotted in figure 4.25 compared to a simulation without thickness variation and with the experimental spectrum. The influence of a random thickness variation is marginal. The intensity of the fringes drops just a little. The random thickness variation cannot explain the loss of intensity of the bandgap.

DBR2 with a monotone increase of thickness was modeled as 15 spectra of increasing CA and PS layer thicknesses within the region of doubled standard deviation weighted with the Gaussian distribution function and averaged. The simulation is plotted in figure 4.26. Apparently the model with a monotone increase of thickness lead to good results. The intensity of the bandgap and the side fringes in the region above 600 nm are in good agreement with the experimental data. The loss of efficiency of DBR2 can be explained by a monotone increase of thickness of the sample.

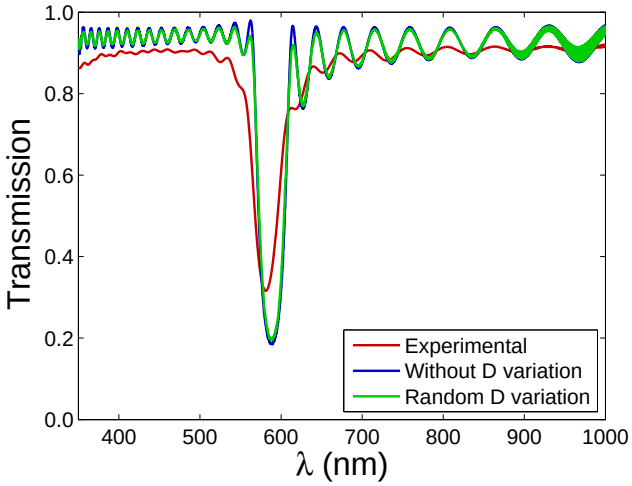

Figure 4.25.: Simulation of a DBR with a random variation of thickness (green). There is no significant change compared to a simulation without thickness variation (blue).

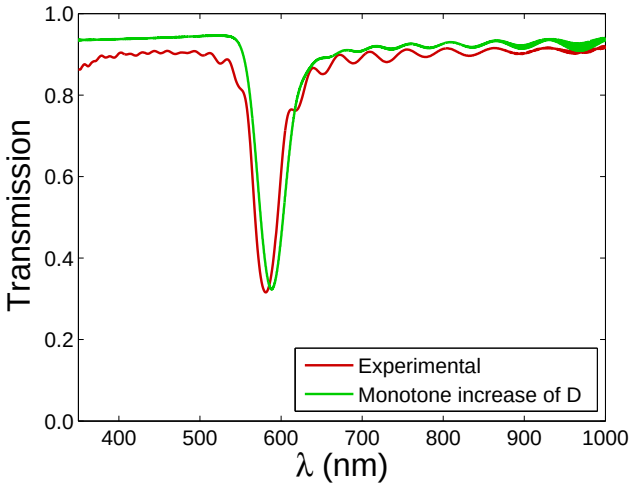

Figure 4.26.: Simulation of a DBR with a monotone increase of thickness. The simulation and the experiment match well.

4.4. Heat Treatment of Distributed Bragg Reflectors

In this section the optical response of a heat treated distributed Bragg reflector will be evaluated. The change of the bandgap will be explained with a thickness loss of CA.

The three DBRs were heat treated with the same routine as the double layer samples in chapter 4.1.3. For two minutes they were heated under a domed heating stage and after they cooled back down to room temperature, a transmission spectrum was taken. The heating temperatures were from 60 °C to 200 °C with 20 °C steps. The transmission spectra for every second heating cycle is plotted in figure 4.27. The bandgaps move to lower λ with increasing temperature. At the temperature of 200 °C (red line) the bandgap efficiency has diminished.

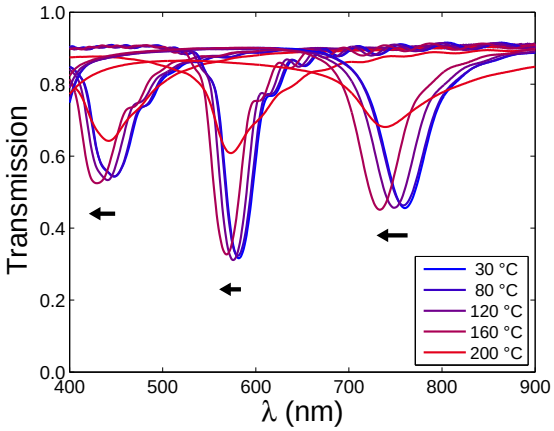

Figure 4.27.: Spectra of DBR1, DBR2 and DBR3 during temperature cycles.

The investigation on the heat treated double layer samples with XRR (see chapter 4.1.3) indicates, that the interface roughness increase from 1 nm to 2 nm from 170 °C to 200 °C (figure 4.7). The loss in the defined interface causes the bandgaps to vanish. Fleischhaker et al. showed a PAZO/PDAC DBR build-up, where the bandgap shifts reversible due heating cycles up to 80 °C[56]. Our results indicates, that heating of an PS/CA DBR up to 80 °C is also a reversible process. The change of gap position starts at 100 °C. The spectrum is not reversible above this temperature any more.

In chapter 4.3.1 the ratio of the thickness of the CA layer and the PS layer was determined with approximately d_{CA}:d_{PS}=1:2 for the three DBRs (table 4.8). With the shrinkage of the layers shown in figure 4.8, the effective reflective index n_{eff} of equation 2.52 can be calculated

versus the temperature. The change of n_{eff} is outermost small. For the wavelength of 600 nm the n_{eff} is plotted versus the temperature (figure 4.28).

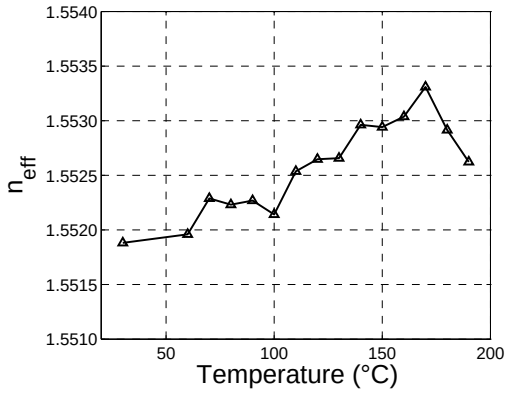

Figure 4.28.: Effective refractive index n_{eff} of DBR2 versus temperature.

The positions of the bandgaps in the temperature cycles were examined. With 2.52 the thickness of the repeat unit can be calculated and the dilatation of the three DBRs can be obtained. In figure 4.29 the dilatation of the three DBRs and the dilatation of the double layer samples PS-CA 1 and CA-PS 1 are plotted. The DBRs are colored in respect to their bandgap position in the visible spectrum. As already seen, the non reversible dilatation start at 100 °C. DBR1 and DBR3 shrink up to the temperature of 190 °C about 4 % and DBR2 2.5 %. The double layer samples PS-CA 1 and CA-PS 1 shrink as well and are in excellent agreement with the DBR dilatation.

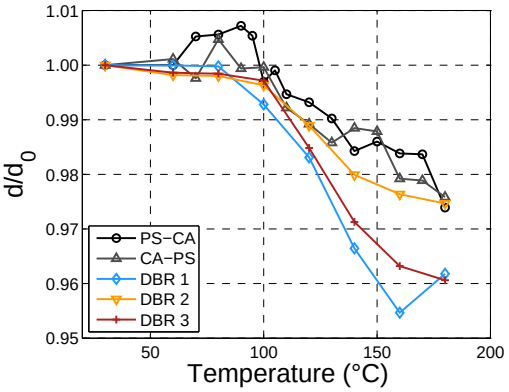

Figure 4.29.: Dilatation of the double layer samples PS-CA 1 and CA-PS 1 due heating. Measured with XRR (see figure 4.8). Estimated dilatation of DBR1, DBR2 and DBR3 based on the shift of the bandgap in figure 4.27.

4.5. Cavities

In the following the optical response of a layer system with an embedded defect layer will be examined. The thickness of the defect layer will be examined and the spectrum will be simulated and compared to the experiment.

The P3HT was embedded into two $(CA\text{-}PS)_{10}$ DBRs. The configuration of the cavity is as followed: $(PS\text{-}CA)_{10}$ P3HT $(CA\text{-}PS)_{10}$. Three cavities were produced: C1, C2 and C3. The spin velocity and solution concentration of CA and PS were the same as for the three DBRs (see table 4.7). The P3HT defect layer was spin casted with a speed of 110 rps for C1 and 90 rps for C2 and C3. The volume of the applied P3HT was 105 µl for each cavity. Transmission spectra and photographs of the three cavities are plotted in figure 4.30.

In the spectra a bandgap appears but with a slightly intermediate photonic energy state. The position of the bandgap of the cavities are the same as for the DBRs (see figure 4.20). The photographs of the cavity look similar to the photographs of the DBR but a lightly sprinkled reddish film is added. P3HT absorbs in the blue region of the spectrum and the transmission appear reddish. The spectra of the cavities are slightly less transparent in the region from 400 nm to 600 nm.

In chapter 2.5 the enhancement of spontaneous emission of active defect layers within a cavity is mentioned. If the intermediate photon energy state (within the bandgap) fits the fluorescence spectrum of the defect layer, a laser can be obtained. In figure 4.31 the fluorescence spectrum of P3HT and the spectrum of C2 is shown. Unfortunately the intermediate photon energy state is not sharp and the position is not exactly at the maximum of the fluorescence of P3HT. The reflectance spectrum of C2 does not show any tendency to enhanced spontaneous light emission (figure 4.31 right).

The thickness of a defect layer is important to modify the position of the intermediate photon energy state. To determine the thickness of the P3HT layer a XRR scan was used. P3HT was spin casted on thermally oxidized silicon substrate with a spin speed of 90 rps and a volume of 105 µl. The P3HT was diluted with PS to avoid the wetting problems. The XRR curve and its Fourier transform are plotted in figure 4.32.

The Fourier transform in figure 4.32 (right) persists of two large peaks at 38 nm and 61 nm and a small peak at 25 nm. Clearly this pattern belongs to a double layer sample where the first peak (25 nm) and the second peak (38 nm) belong to the two layer thicknesses and the third peak is caused by the sum of the two layers. Most likely the P3HT and the PS in the solution gets phase separated. In the book *Conjugated Polymer and Molecular*

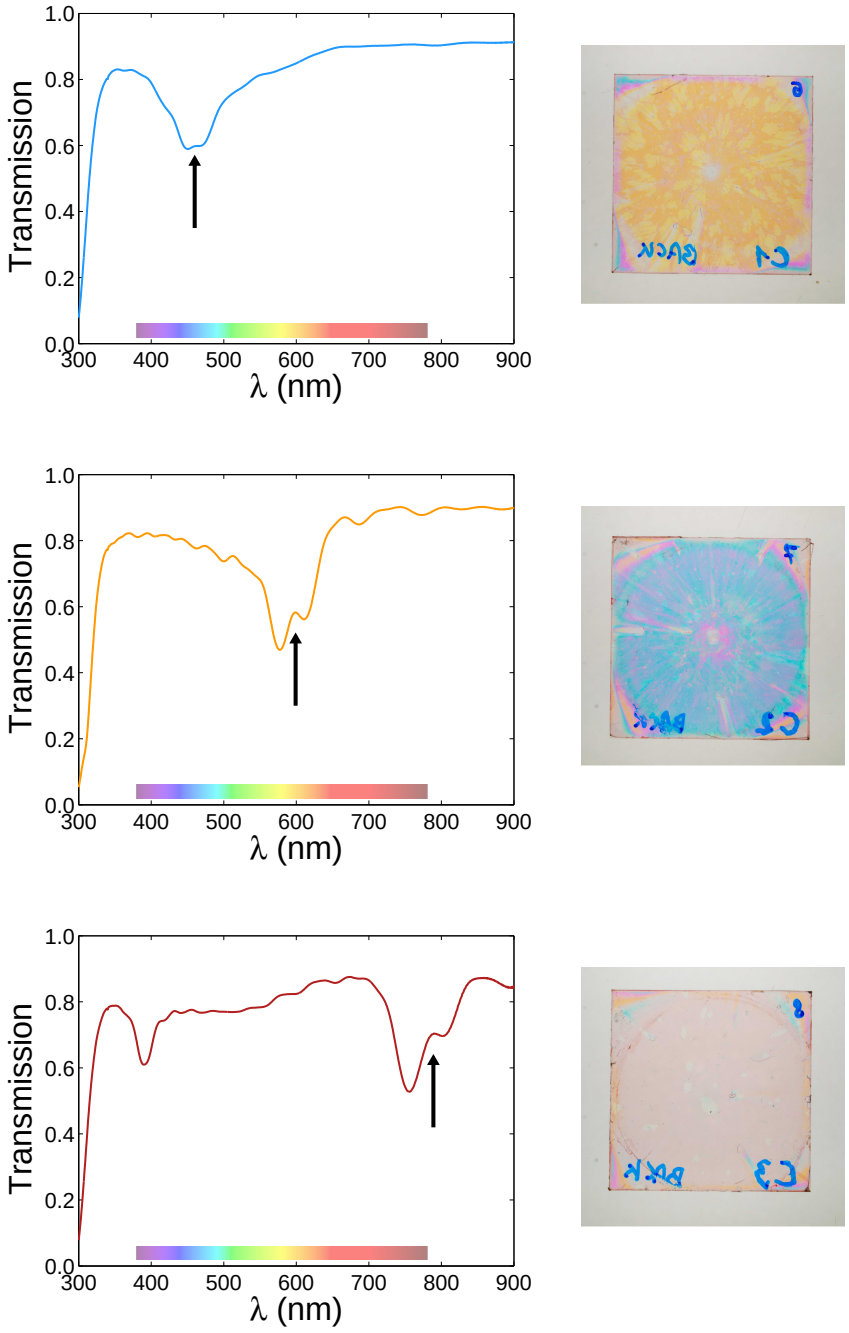

Figure 4.30.: Transmission spectra and photographs of C1 (top), C2 (middle) and C3 (bottom), each a $(PS\text{-}CA)_{10}$ P3HT $(CA\text{-}PS)_{10}$. The bandgap of the cavities slightly exhibits an intermediate photon energy state.

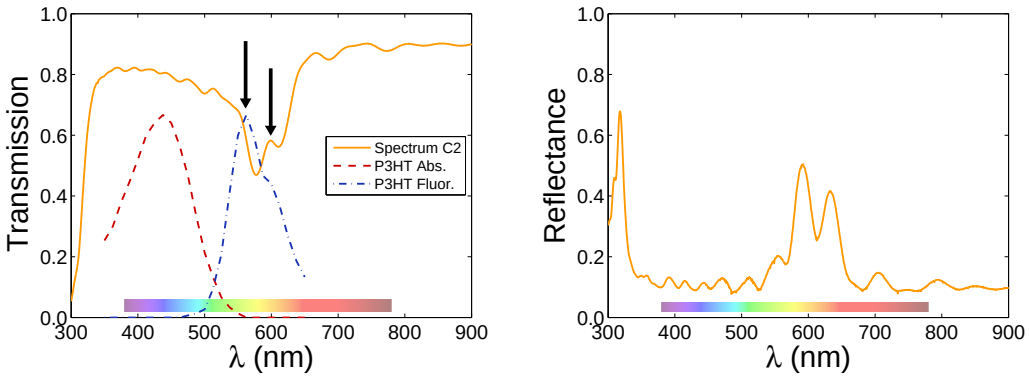

Figure 4.31.: Transmission spectrum of C2, fluorescence and absorption spectra (not scaled to the y-axis) of P3HT (literature data [57]) (left). Reflectance spectrum of C2 (right). The fluorescence of P3HT does not match the intermediate photon state in the bandgap. Therefore the spontaneous emission is not enhanced.

Interfaces by Salaneck W. R. the author describes the possible structures of two-phase films [58, p. 119]. He recommends to measure the density profile by means of reflectivity techniques to determine the phase separation in direction normal to the surface. The result of the P3HT/PS blend suggests a film structure of an interdigitating double layer. A clear determination of the polymer-polymer miscibility of P3HT and PS would go beyond the scope of this section. For further information on this topic, the book *Polymer-Polymer Miscibility* by O. Olabisi et al. is recommended [59].

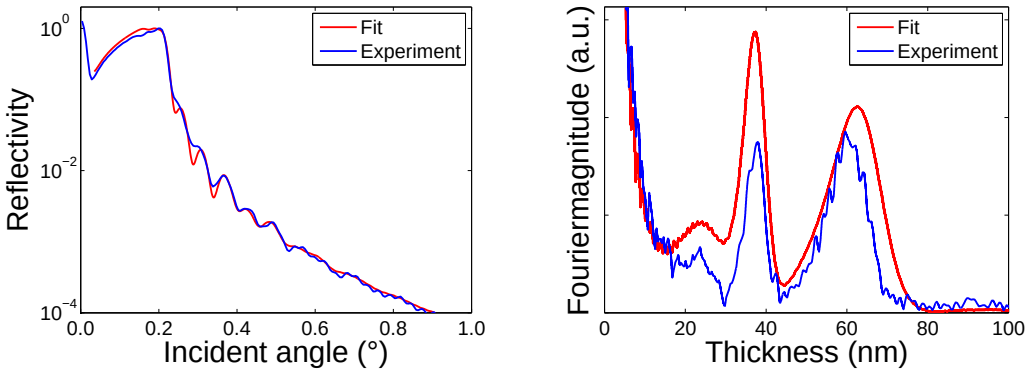

Figure 4.32.: XRR graph of the P3HT (left) and its Fourier transform (right). The fit of a P3HT-PS double layer system matches the data.

The fit models a double layer sample P3HT-PS on thermally oxidized silicon substrate. It suits to the data as well as to the three peaks in the Fourier transform. A fit with a single polymer layer is not able to map the peaks in the Fourier transform. The P3HT layer was evaluated with a thickness of 28.4 nm and an interface roughness to the substrate of 3 nm. The thickness of the PS layer was examined with 39.0 nm. The interface roughness between the P3HT and the PS was 1.5 nm. The surface of the PS layer was impressively smooth with only 0.35 nm roughness. The refractive index, in terms of the wavelength of P3HT was taken out of the literature [57]. The calculation of a cavity spectrum needs additional transfer matrices at the position of the defect layer. The sprinkled features in the layer suggests a great thickness variation of the defect layer. The simulation neglect all thickness variations and absorption behavior. The comparing of the experimental and the simulated spectrum of C2 is plotted in figure 4.33. The magnitudes of the bandgap and the fringes cannot be represented accordingly without thickness variation. Nevertheless the position of the intermediate photon energy state matches excellent.

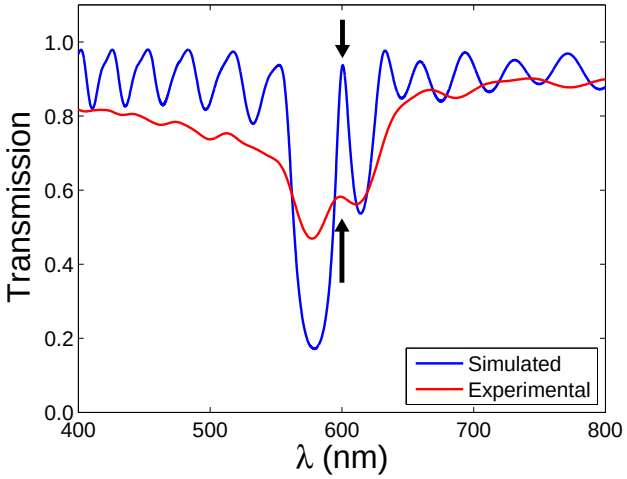

Figure 4.33.: Simulated cavity of a configuration of $(\text{PS-CA})_{10}$ PS-P3HT $(\text{CA-PS})_{10}$ compared to the experimental data of C2. The intermediate photon energy state in the gap fits superior.

5. Conclusion

The determination of the thickness, the surface roughness and the interface roughness as well as the refractive index of all-polymer distributed Bragg reflectors in the field of optical devices was successfully performed by multiple experimental approaches.

Double layer samples, spin coated on silicon wafers, suit the resolution profile of the X-ray reflectivity method. The measured surface roughness of CA, PS and PVK spin casted double layers is σ_{CA}=0.48 nm, σ_{PS}=0.41 nm and σ_{CPVK}=0.52 nm. The interface roughness of CA and PS and the interface roughness of CA and PVK is surprisingly small ≈1 nm. During thermal treatment of the samples PS-CA and CA-PS the surface roughness stays constant and the electron density does not change likewise. The interface roughness stays up to 170 °C at ≈1 nm and increases from 170 °C to 200 °C to ≈2 nm. The CA layer constantly shrinks during the thermal treatment (up to 7 % at 200 °C). The PS layer thickness stays constant up to 170 °C and diminished ≈1 % up to 200 °C.

The surface roughness was additionally determined by investigation with atomic force microscopy. The CA layer has circular protrusions and azimuthal not oriented needle-shape structures. The surface roughness of the CA layer is (0.80±0.30) nm for the PS-CA sample and (0.65±0.15) nm for the PVK-CA sample. The surface of the PS layer contains arbitrary distributed circular holes and the surface roughness is (0.30±0.04) nm. The PVK layer has no features and the surface roughness is (0.35±0.05) nm. The surface roughnesses measured with atomic force microscopy and with X-ray reflectivity are in good agreement.

With spectroscopic ellipsometry the optical properties and the double layer thickness were determined. The double layer sample PS-CA has a thicknesses of 190.3 nm and CA-PS a thickness of 195.9 nm. Compared to the X-ray reflectivity measured thickness of PS-CA (189.2 nm) and of CA-PS (193.8 nm), the results match perfectly. In the optical spectrum the refractive index of CA and PS is flat do not absorb. The fitting of the data of PVK-CA and CA-PVK was not satisfying.

The intensity of the reflectance increased with the number of the repeat units of a (PVK-CA)$_X$ DBR. The more layers applied, the larger the badgap gets. At 15 PVK-CA repeat units we were able to get a bandgap reflectivity as high as 94 %.

The transmission and reflectance spectra of three (PS-CA)$_{20}$PS evidence, that changing the spinspeed and the polymer solution concentration shifts the bandgap position. A high spinspeed produces thin layers and a highly concentrated solution causes thick layers. The bandgaps were located at λ_{DBR1}=480 nm, λ_{DBR2}=598 nm and λ_{DBR3}=780 nm.

The examination of double layer samples on silicon wafers (with the same preparation condition as the (PS-CA)$_{20}$PS DBRs) with X-ray reflectivity determined the thickness of the PS and the CA layer. With the transfer matrix method a theoretical spectrum was simulated using the layer thickness of CA and PS (gained out of X-ray reflectivity) and the refractive index of CA and PS (examined by spectroscopic ellipsometry). Although the simulated spectra of DBR1 and DBR2 have a more reflective bandgap and more distinctive side fringes, the calculated positions of the gaps match excellent. The simulation of DBR3 is not in good accordance with the experiment. For further use of this method it is recommended to have more double layer samples to minimize the statistical error. The standard deviation of thickness of PS and CA layers of DBR2 was determined with SD_{CA}=2.3 nm and SD_{PS}=3.0 nm. The simulation was modified to include either a random variation of thickness or a monotone increase of thickness. Only a monotone increase of thickness was able to represent the loss of efficiency of the gap and the side fringes of an experimental spectrum satisfyingly.

After thermal treatment above 80 °C the bandgap of the three DBRs shifts to lower λ which indicates a non reversible loss of thickness. At 190 °C the DBRs thickness reduction is between 2.5 % and 4 %. That matches excellent with the shrinkage of the double layer samples PS-CA 1 and CA-PS 1 determined with X-ray reflectivity. Between 180 °C and 200 °C the efficiency of the bandgap of the three DBRs drops to <50 %. The reason can be ascribable to the increasing interface roughness above 170 °C.

A cavity made of a P3HT/PS blend defect layer embedded between two (PS-CA)$_{10}$ DBRs, creates a discrete photon energy state within the bandgap. X-ray reflectivity on a single P3HT/PS layer suggest a phase separation of the two polymers. A fit with a PH3T layer (d_{P3HT}=28.4 nm) underneath a PS layer (d_{PS}=39.0 nm) is able to represent the data. The surface roughness of the PS is 0.35 nm and the interface roughness between the PS and the P3HT layer is 1.5 nm. The position of the discrete intermediate photon energy state of a simulated spectrum is accurate to the experiment.

The combined approach of X-ray reflectivity, spectroscopic ellipsometry and atomic force microscopy has proven to be an excellent method for the investigation of all-polymer distributed Bragg reflectors.

A. Appendix

A.1. Paper Submitted for the International Conference on Transparent Optical Networks 2014 Proceedings

Conference:

16th International Conference on Transparent Optical Networks

Convention Center Graz (Grazer Messe), Graz, Austria

6th-10th July, 2014

Abstract (submitted) [60]:

Distributed Bragg Reflectors:

Morphology of Cellulose Acetate and Polystyrene Multilayers

by

Katrin Unger, Roland Resel, Caterina Czibula, Christian Ganser, Christian Teichert, Georg Jakopic, Giancarlo Canazza, Serena Gazzo, Davide Comoretto

Oral contribution:

10th July, 2014 between 10:50 and 12:40

Distributed Bragg Reflectors: Morphology of Cellulose Acetate and Polystyrene Multilayers

Katrin Unger,[1] Roland Resel,[1] Caterina Czibula,[2,3] Christian Ganser,[2,3] Christian Teichert,[2] Georg Jakopic,[4] Giancarlo Canazza,[5] Serena Gazzo,[5] Davide Comoretto[5]

[1] *Institute of Solid State Physics, Graz University of Technology, Petersgasse 16, 8010 Graz, Austria*

[2] *Institute of Physics, University Leoben, Franz-Josef-Straße 18, 8700 Leoben, Austria*

[3] *Christian Doppler-Laboratory for Surface Chemical and Physical Fundamentals Of Paper Strength, Graz University of Technology, 8010 Graz, Austria*

[4] *Institute of Surface Technology and Photonics, Joanneum Research, 8160 Weiz, Austria*

[5] *Department of Chemistry and Industrial Chemistry, University of Genua, 16146 Genua, Italy*

e-mail: roland.resel@tugraz.at

ABSTRACT

The optical quality and photonic properties of all-polymer distributed Bragg reflectors are related to the morphology of the layers and the optical responses of the materials. We introduce the X-ray reflectivity method to determine the thickness, the interface- and surface-roughness of cellulose acetate and polystyrene layers which are two polymers often used in the domain of spin casted multilayer systems. Atomic force microscopy and spectroscopic ellipsometry were used as complementary techniques for investigating the surface roughness and the film thickness. The shrinkage and the change of interface roughness of the polymers were investigated up to temperatures of 200 °C. Up to 170 °C the interface roughness stays constant at about 1 nm while it increases up to 2 nm at 200 °C. The thickness of the polystyrene layer remains constant up to 170 °C, well above its glass transition temperature T_g. For cellulose acetate a monothonic decrease is observed with increasing temperature. It could be shown, that the change in the optical response of a thermally treated distributed Bragg reflector is related to the change of the layer thickness of cellulose acetate. Spectra of (PS CA)$_{20}$PS distributed Bragg reflectors (DBR) are in a good agreement with calculated spectra with parameters optained from of the X-ray reflectivity measurements.

Keywords: X-ray reflectivity, organic polymer film, thin film morphology, heat treatment

1 INTRODUCTION

Spin casting is a powerful technique for the production of all-polymer multilayer stacks. Systems of 20 double layers can be produced in an easy and fast way [1, 2]. The layer thickness can be tuned by varying spin speed and concentration of the polymer solutions. The bandgap λ_{Gap} is dependent on the thickness (d_1, d_2) and the refractive index (n_1, n_2) of the two polymers in a very simple way[1, 2]: $\lambda_{Gap} = 2\,(d_1 n_1 + d_2 n_2)$. Different pairs of thicknesses can lead to the same bandgap λ_{Gap}. The properties of such structures critically depends on the transparency of materials, the reproducibility of layer properties and quality of interfaces. Therefore it is of huge interest to determine the layer morphology in combination with the optical response of DBRs.

Here, we propose the use of X-ray reflectivity as a technique to determine layer thickness and interface roughness. The methode is based on the optical properties (reflection and transmission) of X-rays at surfaces and interfaces. The refractive indices $n_{\text{X-ray}}$ just slightly vary for different materials $n_{\text{X-ray}} = 1 - \delta + i\beta$, with $\delta \approx 10^{-6}$ [3]. Each interface within the sample causes reflection and totally produce an interference pattern, so called Kissing fringes [4]. Surface- and interface-roughness cause the signal to drop [5]. While the fringes are related to the thicknesses of the polymer layers, the slope is related to the involved roughnesses.

2 EXPERIMENTAL

2.1 Material and preparation

The cellulose acetate (CA) used in this study is distributed by *Sigma Aldrich*. The M_W is 63000 g/mol and the refractive index n_{CA} is 1.475. Dissolved in diaceton alcohol it forms a suitable solution for spin casting. The standard concentration is c_{CA}=27 g/l. The polystyrene (PS) is also provided by *Sigma Aldrich*, with M_W=192000 g/mol. The refractive index in the visible region is n_{PS}=1.59. PS was dissolved in filtered toluene. The standard concentration is c_{PS}=32 g/l. Both polymers are not optical active in the visible spectrum.

We used dynamical spin casting to build-up multistacks. The spin coater rotates permanently and the two solutions were deposited alternating one at a time. CA and PS are solved in orthogonal solvents to assure, that the underlying layer is not dissolved by the next layer. For the distributed Bragg reflectors (DBR) (PS CA)$_{20}$PS systems were dynamically spin casted on glass substrates with an applied volume of 105 µl and spin velocity in the range of 90-180 rps for each layer. For the investigation with X-ray reflectivity, double layer samples PS-CA and the reverse samples CA-PS were spin casted on thermally oxidized silicon substrate with a volume of 90 µl. A sample, where the PS is applied first and the CA is applied on top, will be called PS-CA.

2.2 X-ray reflectivity

The measurements were performed with a *PANalytical Empyrean* system with radiation of a copper tube (λ=1.54 Å). On the primary side the reflectometer is equipped with a 1/32 ° slit, a 10 mm beam mask and a multilayer mirror. On the secondary side is a receiving slit of 0.1 mm, a Soller slit of 0.02 rad and a *PANalytical PIXEL^{3D}* used as point detector. The data was fitted with *X'Pert Reflectivity 1.3*, which uses the Parratt formalism [6].

Four PS-CA and CA-PS samples were prepared with standard concentration and a spin speed of 180 rps. A typical X-ray reflectivity curve is plotted in figure 1. The fringes are related to the film thicknesses. For the sample CA-PS 1 following film thicknesses were determined: d_{PS}=100 nm and d_{CA}=91 nm. The results for all four samples are listed in table 1. The thickness of CA and PS varies between 86 nm<d_{CA}<93 nm and 97 nm<d_{PS}<101 nm. The surface of the samples shows a roughness between 0.41 nm<σ_{sf}<0.47 nm. The interface is also of high quality with a roughness of $\sigma_{if}\approx$1 nm.

Thermal treatment was performed with a domed heating stage *DHS 900* under constant helium flow. Starting at 60 °C, with temperature steps of 10 °C up to 200 °C, the sample was heated for 2 min. After each step, the sample cooled back down to room temperature and a X-ray reflectivity scan was taken. In figure 2 the change of thickness of CA and PS and the roughness change is plotted. The thickness-loss of the sample is mainly caused by CA. The PS is stable up to 170 °C. The surface roughness for both samples is σ_{sf}=0.4 nm during the entire thermal treatment procedure. The interface roughness stays up to 170 °C at $\sigma_{if}\approx$1 nm. Up to 200 °C it increase to $\sigma_{if}\approx$2 nm. This result is quit interesting, since even for temperatures larger than the polymer T_g (110 °C for PS and 130-190 °C for CA, respectively), the quality of interfaces and thicknesses control is retained. This result suggests that in confined structures polymer thermal properties are modified with respect to the bulk as recently shown for core-shell microspheres used for the preparation of polymer photonic crystals [7].

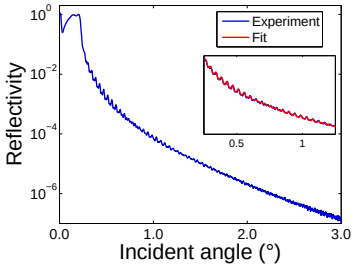

Figure 1: X-ray reflectivity curve of CA-PS 1 sample. The fringes are related to film thicknesses.

Table 1: CA thickness d_{CA}, PS thickness d_{PS}, interface roughness σ_{if} between CA and PS and surface roughness σ_{sf} in (nm).

Samples	d_{PS}	d_{CA}	σ_{if}	σ_{sf}
CA-PS 1	100	91	1.05	0.41
CA-PS 2	101	93	1.04	0.41
PS-CA 1	97	86	0.99	0.45
PS-CA 2	97	92	0.82	0.47

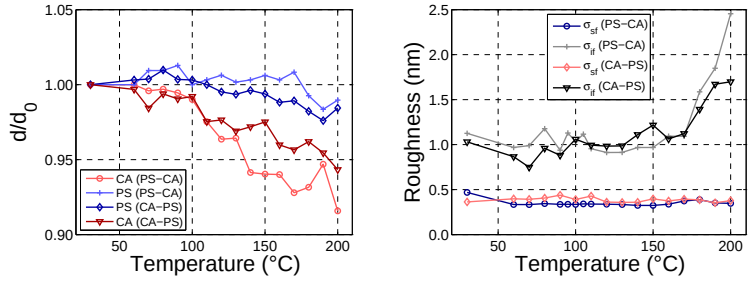

Figure 2: left: shrinkage of CA and PS versus temperature, with d, the thickness of the polymer film during thermal treatment and d_0, the thickness of the film before thermal treatment
right: surface roughness σ_{sf} and interface roughness σ_{if} between CA and PS versus temperature.

2.3 Atomic force microscopy and spectroscopic ellipsometry

The atomic force microscope used, was a *MFP-3D* from *Asylum Research*. A medium soft silicon cantilever *OMCL-AC240TS* was used in tapping mode. With a spring constant of 2 nm it is suitable for observing surfaces of soft or viscous materials. The set point was 780 mV, the drive frequency of the piezo element was 60 kHz and the scan speed was 10 µm/s. The *Gwyddion* software was used to visualize the data and analyze the surface roughness. The atomic force images of the samples PS-CA 2 and CA-PS 2 are shown in figure 3. The CA has a surface roughness of σ_{rms}=0.80 nm, figure 3 (left). There are some grain-like protrusions with circular cross-sections as well as azimuthally not oriented, needle-shaped structures. A more detailed analysis of these structures was made by line profiles. Eight needle structures and five grains were averaged. $CA_{needles}$: length=(415±80) nm, width=(130±60) nm, height=(4±3) nm; CA_{grains}: width=(185±35) nm, height=(8±3) nm. The PS surface reveals some arbitrary distributed circular holes. The PS surface has a roughness of σ_{rms}=0.35 nm. To examine the

holes, thirteen line profiles were analyzed. PS_{holes}: width=(45±5) nm, depth=(2±1) nm.

The surface roughness gained by atomic force microscopy can be compared to X-ray reflectivity (cf. table 2). For the sample CA-PS (with PS on top) the roughness is in good accordance. For PS-CA, the values are in the same order of magnitude. The grains and needles do not provide a normally distributed height function. We expect, that the atomic force microscopy is more accurate. The dimensions of the surfaces defects are compared to the wavelength of visible light ((380-780) nm) very smooth.

Specular ellipsometry scans were performed with a *VASE Ellipsometer* with a *J.A. Woollam* HS-190 monochromator. Under an incident beam angle of 65 ° and 75 ° to the surface, reflection spectra between 240 nm and 1340 nm were measured and fitted with *VASE*. The summation of both polymer thicknesses was compared with the X-ray reflectivity (cf. table 2). The values match excellent with a deviance of 0.6 % for PS-CA and 1 % for CA-PS. Further the refractive index n(λ) was examined with spectroscopic ellipsometry. The refractive index of CA and PS is nearly constant in the visible spectrum with n_{CA}=1.48 and n_{PS}=1.59. This confirms quit well with the data from literature [2].

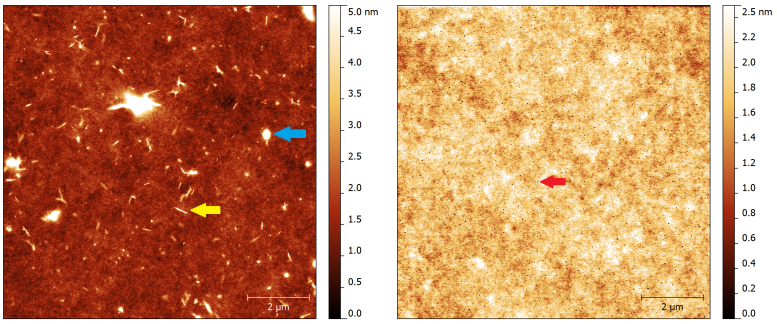

Figure 3: (10×10) μm^2 Atomic force microscopy images of the samples PS-CA 2 (left) and CA-PS 2 (right). The arrows are marking representative surfaces structures (yellow - needle, blue - protrusion, red - hole).

Table 2: Surface roughness σ_{sf} and thickness of the CA (d_{CA}) and PS (d_{PS}) films measured with different techniques.

Technique	PS-CA 2		CA-PS 2	
	σ_{sf} (nm)	d_{PS}+d_{CA} (nm)	σ_{sf} (nm)	d_{CA}+d_{PS} (nm)
Atomic force microscopy	0.80		0.35	
Spectroscopic ellipsometry		190.3		195.9
X-ray reflectivity	0.47	189.2	0.41	193.8

2.4 Spectra of distributed Bragg reflectors

Three DBRs, $(PS\ CA)_{20}PS$ systems, were produced with following preparation parameters. DBR1: c_{CA}=20 g/l, c_{PS}=22 g/l, spin speed=110 rps; DBR2: standard concentration, spin speed=150 rps; DBR3: standard concentration, spin speed=90 rps. The layer thicknesses were investigated with X-ray reflectivity on equal produced double layer samples. DBR1: d_{CA}=46 nm and d_{PS}=95 nm, DBR2: d_{CA}=62 nm and d_{PS}=126 nm, DBR3: d_{CA}=84 nm and d_{PS}=175 nm. The transmission spectra, taken with an *UV-1800 Shimadzu* spectrometer, are plotted in figure 4 (left). The position of the bandgaps are: λ_{DBR1}=442 nm, λ_{DBR2}=568 nm and λ_{DBR3}=733 nm. The DBRs were thermally treated, in agreement with X-ray reflectivity data reported in figure 2 (left). The transmittance was recorded after each step, figure 4 (middle). The gap of each DBR shifts to lower λ which is related to a loss of thickness. At 200 °C no bandgap can be further observed. Using the layer thickness, the shrinkage of CA and PS and the refractive index, the shrinkage of the three DBRs can be calculated. In figure 4 (right) the results and the shrinkage of the double layer samples PS-CA 1 and CA-PS 1 are plotted. The observed shrinkage of the double layer samples and the DBRs are in good agreement. The diminution optained from DBRs is quite high with (2.5-4) % and is mainly caused by the CA layers. From data reported in figure 4 (middle), we notice again, that the photonic crystal structure is surprisingly retained for all samples up to 180 °C indicating that the confined polymer layers retains their structural properties even at temperature larger than T_g.

A mathematical model for the optical response of layered $(PS\text{-}CA)_{20}PS$ systems was developed [8]. The layer thicknesses of DBR2 and the refractive index of spectroscopic ellipsometry were used to calculate the transmission, see figure 5 (left, blue curve). Compared to the experimental result of DBR2 (red curve), the model has a slightly higher bandgap and more pronounced side fringes. The gap position of the calculated spectrum is just slightly off to the measured spectrum (Δλ=6 nm). The efficiency and fringes loss is presumably caused by scattering on defects or variation of thickness either along the depth or along the plane. The relative standard deviation of thickness was examined by X-ray reflectivity, σ_{CA}=2.0 % and σ_{PS}=1.6 %. The model was modified with a Gaussian distributed thickness with the standard deviation of thickness added to the interface roughness (see figure 5 (right)). The gap height is now almost equal and the fringes above 750 nm are in better agreement. Below 550 nm the real DBR

might scatters and is therefore less transparent than simulated in the model. Summarizing, the bandgap efficiency loss was mainly caused by the thickness variation together with the interface roughness.

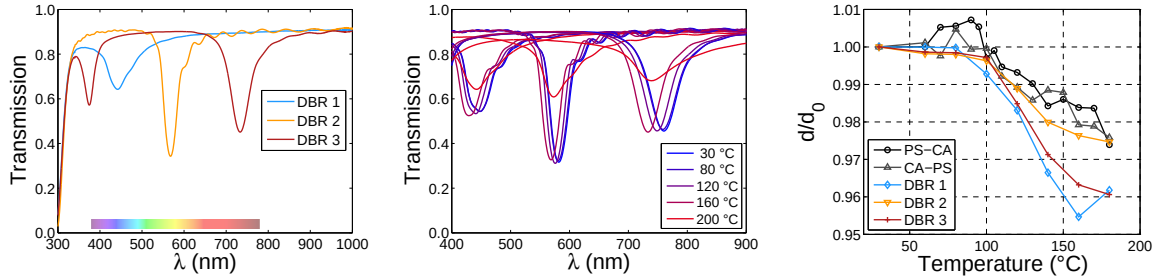

Figure 4: left: transmission spectra of the three DBRs; middle: change of the bandgap during thermal treatment; right: shrinkage of the DBRs calculated from the optical data (blue, red and orange) and from X-ray reflectivity (black and grey)

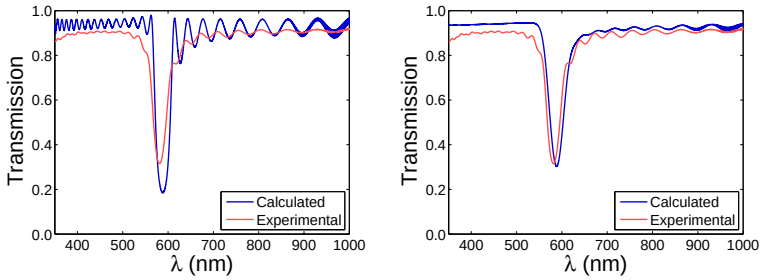

Figure 5: left: transmission spectra of a DBR and calculated spectra with the measured thicknesses and refractive indices; right: improving the calculated spectra with the measured thickness variation.

3 CONCLUSIONS

The determination of the thickness, the surface roughness and the interface roughness of all-polymer layers and DBRs in the field of optical devices was successfully performed by X-ray reflectivity. The surface roughness of CA and PS spin casted layers is σ_{CA}=0.46 nm and σ_{PS}=0.41 nm. The surface roughness stays constant during thermal treatment. The interface roughness stays at ≈1 nm and increases from 170 °C to 200 °C to ≈2 nm. The CA layer shrinks constantly during the thermal treatment. PS shows constant film thickness up to 170 °C. X-ray reflectivity data were compared to the data gained by atomic force microscopy and spectrospopic ellipsometry. The results of the techniques are in excellent agreement.

The thickness of CA and PS layers of three (PS CA)$_{20}$PS DBRs were examined by X-ray reflectivity. DBR1: d_{CA}=46 nm d_{PS}=95 nm, DBR2: d_{CA}=62 nm d_{PS}=126 nm, DBR3: d_{CA}=84 nm d_{PS}=175 nm.The positions of the bandgaps in the spectrum are: λ_{DBR1}=442 nm, λ_{DBR2}=568 nm and λ_{DBR3}=733 nm. The DBRs were thermally treated and the bandgaps shift to lower λ. The DBRs shrink mainly due to the loss of CA thickness.

With the thickness measured with X-ray reflectivity and the refractive index gained by spectroscopic ellipsometry a model was calculated and compared to the experimental spectrum. The examined deviation of thickness and the interface roughness helped the model to improve the consistency with the DBR spectrum.

References

[1] G. Canazza, F. Scotognella, G. Lanzani, S. De Silvestri, M. Zavelani-Rossi, D. Comoretto: Lasing from all-polymer microcavities, *Laser Phys. Lett.*, vol. 11 035804, 2014.

[2] L. Frezza, M. Patrini, M. Liscidini, D. Comoretto: Directional Enhancement of Spontaneous Emission in Polymer Flexible Microcavities, *J. Phys. Chem. C*, vol. 115. pp. 19939-19946, 2011.

[3] J. Daillant, G. Jean, X-ray and Neutron Reflectivity, Springer-Verlag GmbH, 2008.

[4] H. Kiessig: Interferenzen von Röntgenstrahlen an dünnen Schichten, *Ann. Phys.*, vol. 10. pp. 769-789, 1931.

[5] L. Nevot and P. Croce, *Rev. Phys. Appl.*, vol. 15. pp. 761-779, 1980.

[6] L. Parratt, *Phys. Rev.*, vol. 95. pp. 359-369, 1954.

[7] K. Sparnacci, D. Antonioli, S. Deregibus, M. Laus, G. Zuccheri, L. Boarino, N. De Leo, and D. Comoretto: Preparation, Properties, and Self-Assembly Behavior of PTFE-Based Core-Shell Nanospheres, *J. of Nanomat.*, vol. 2012 980541, 2012.

[8] M. Skorobogatiy and J. Yang, Fundamentals of Photonic Crystal Guiding, Cambridge University Press, 2009.

A.2. Spectroscopic Ellipsometry Datas and Fits

In figure A.1, figure A.2, figure A.3 and figure A.4 the spectroscopic ellipsometry data Ψ and Δ and the resulting refracting indices N=n+iκ of the samples PS-CA 2 and PVK-CA 2 are plotted. The fit of the PS-CA 2 sample matches with the experiment. The experimental data of PVK-CA 2 cannot be represented by the fit. Especially in the UV range the fit deviates from the data.

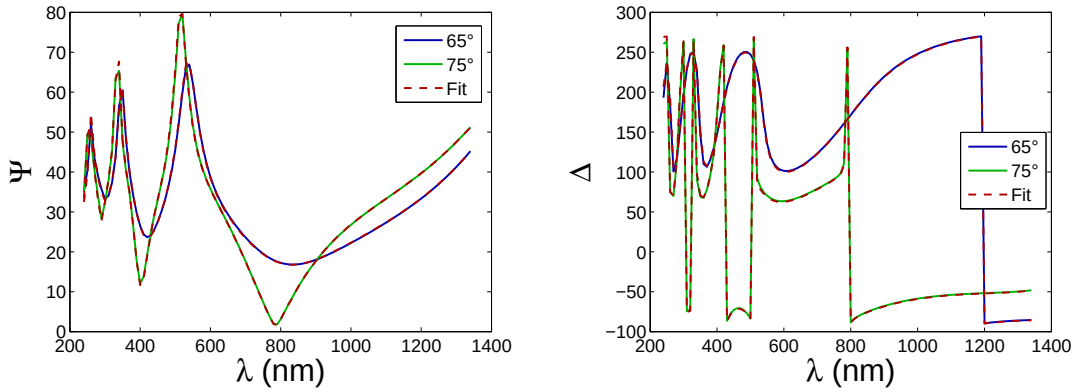

Figure A.1.: Δ and Ψ curves of the PS-CA 2 sample. The blue and the green line belong to the incident angles of 65 ° and 75 °. The red dashed line is the fit.

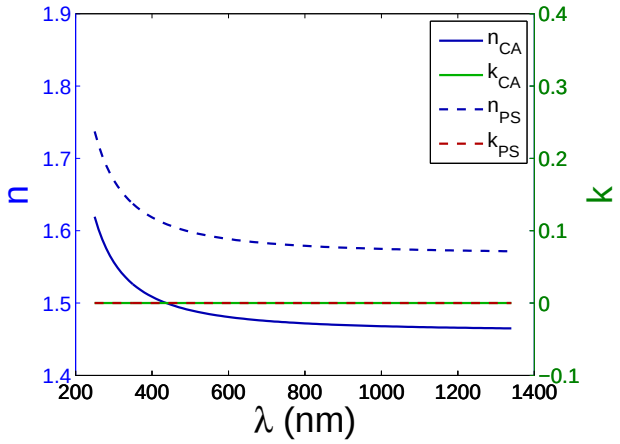

Figure A.2.: Real and complex part of the refractive index N=n+iκ of the CA and PS layer of the sample PS-CA 2.

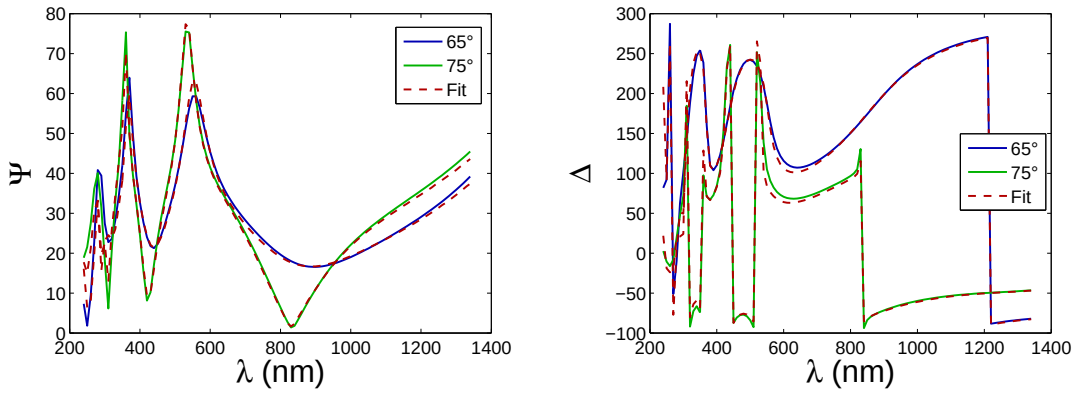

Figure A.3.: Δ and Ψ curves of the PVK-CA 2 sample. The blue and the green line belong to the incident angles of 65 ° and 75 °. The red dashed line is the fit.

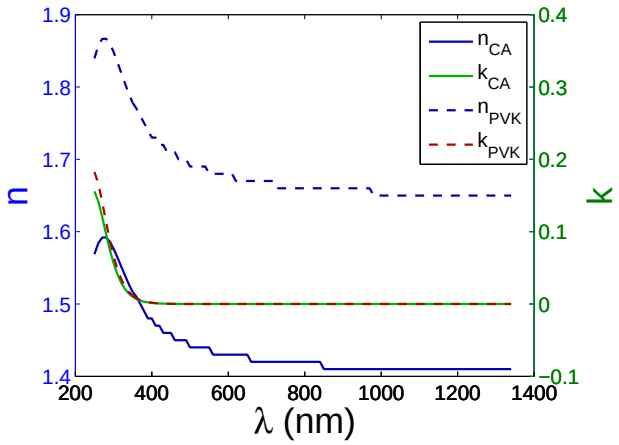

Figure A.4.: Real and complex part of the refractive index N=n+iκ of the CA and PVK layer of the sample PVK-CA 2.

A.3. Attenuator of the Empyrean PANalytical

The Empyrean PANalytical is equipped with an automatic beam attenuator. The standard attenuation factor for our attenuator (id = 26010001 $name$ = Programmable beam attenuator Ni 0.125 mm) is 144. Typical values for the automatic to turn the attenuator on is above 900000 counts/s and switching it off at 600000 counts/s. In the measured xrdml-files the intensities and the corresponding attenuation (on or off, 144 or 1) is saved. Further programs, like *Data Viewer* or *X'Pert Reflectivity* multiply the intensity with the factor and generate a continuously data series.
During XRR measurements the data exhibit a kink when the attenuator switches off (see figure A.5). This indicates, that the attenuation factor of 144 is not correct. To calculate the correct factor two methods were used.

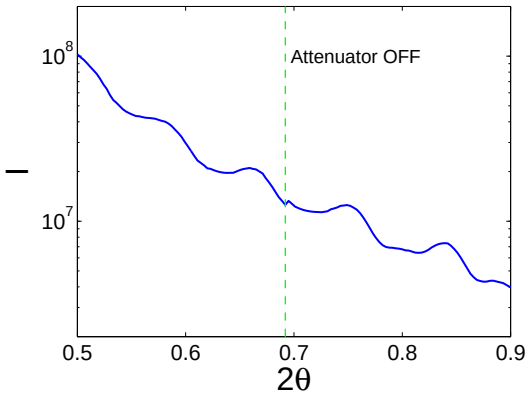

Figure A.5.: XRR curve with a kink at where the attenuator is switched on.

Method: continuously slope

Asimple calculation of the average of the slope before and after the kink exhibits the information, where the data before the attenuator was switched off, should lie. In figure A.6 the red curve has no kink anymore and lies above the measured curve. We have a higher attenuation than 144. Four data sets were investigated and all of them show the same behavior. The calculated correct attenuation factor is 157 ± 6. This is a high standard deviation but we should keep in mind, that we are calculating average slopes of a data series which drops with a power of -4 and provide fringes. Other methods are required.

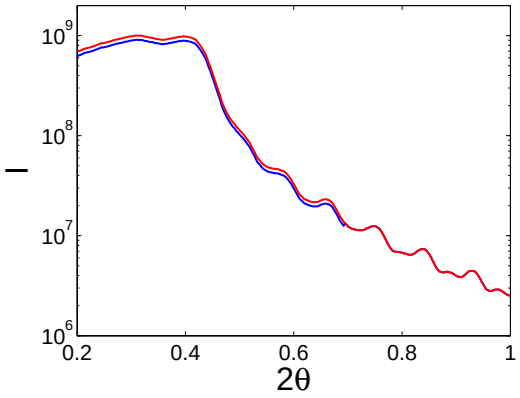

Figure A.6.: X-ray reflectivity data (blue), corrected attenuation factor (red).

Method: additional attenuator

The best method to determine the attenuation factor is to measure the same data with and without attenuator. To do so we measured the direct beam with the attenuator once switched on and once switched off. To not destroy the detector an additional attenuator is required. This is a small plate that can be put into the slit of the beam mask. To get a optical back check a z-scan was performed where the intensity drops to zero when the stage blocks the beam. Both measurements are plotted in figure A.7. The red curve was measured with the attenuator switched on and for the plot multiplied with the attenuation factor of 144. Clearly the red data are not multiplied with the correct factor as the red and the blue data should lie at the same intensity. The correct factor is 155.6 ± 0.4. Additional we see a worse signal to noise ratio for the red curve but this is natural for a measurement with attenuators.

Results

Both methods lead to similar results. The attenuation factor is not 144 but a higher value. The method with the additional attenuator is a more fail-safe method and leads to a result with less deviation. So we need to change the attenuation factor in the program *Data Collector* from 144 to 155.6.

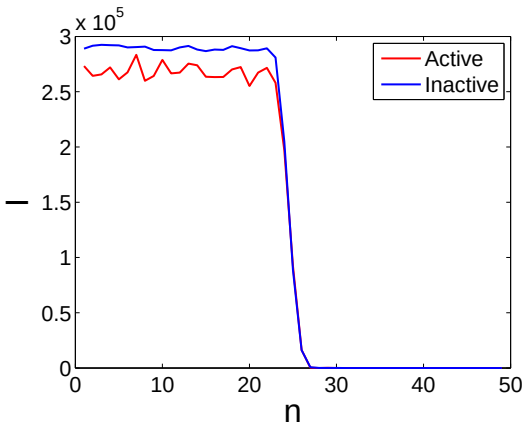

Figure A.7.: blue: measured intensity with the attenuator switched on, red: with the attenuator switched off.

A.4. Simulation Routine in Matlab

In this chapter the Matlab code of a simulation of a DBR spectrum will be presented. The used mathematical method a transfer matrix, described in chapter 2.3. Each transmission of the light beam through an interface can be represented with a matrix. With a simple matrix by matrix multiplication a propagation of light through layered material is accomplished. The transmission and the reflection can be calculated with the elements of the final matrix, see equation 2.30 and 2.37. For each ω in the spectrum, the transfer matrices, and the transmission and reflection, have to be calculated separately.

The simulation consists of:

- the program called DBR_Simulation. The range of the spectrum, the layer thickness and substrate properties get initialized. The spectrum gets calculated, smoothed and plotted.
- the function fun_spectrum_DBR. It gets called by DBR_Simulation. The output is a transmission spectrum.
- the function fun_transfer_matrix, which is the heart of the program. It gets called from fun_spectrum_DBR to calculate the transfer matrix.
- and the function fun_spectrometer_smoothing, which smooths the spectrum.

  By compiling DBR_Simulation the spectrum received should look the same as in figure A.8. On the following pages the four parts are explained.

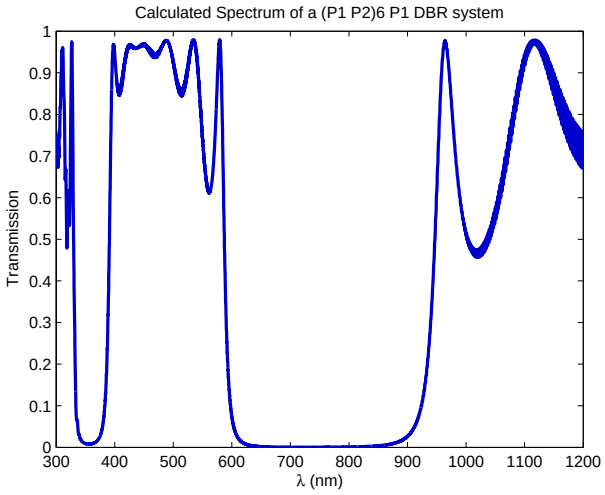

Figure A.8.: Simulated spectrum of a DBR

DBR_Simulation

The first main block is the initialization of the parameters. The range of λ should be a bit larger and the stepsize 5 times smaller than needed. Cause of the glass substrate the spectrum will get quit messy with narrow fringes throughout the complete spectrum. Real spectrometer have resolutions of about 1 nm and are not able to distinguish the fringes. The spectrum needs to be smoothed and therefor the stepsize should be small. The rest of the parameters are well explained within the code. In the next block the functions fun_spectrum_DBR and fun_spectrometer_smoothing are calculating the spectrum and in the third block the result gets visualized.

```
% DBR_Simulation: Calculation and visualization of a Distributed Bragg Reflector
% Katrin Unger
clear all; close all; clc

global c0 W n_Glas d_Glas Cpl
%c0: Speed of light
%W: Vector of the angular frequencies of the incomming beam
%n_Glas: Refractive index of the glass substrate
%d_Glas: Thickness of the glass substrate
%Cpl: Number of double layers of P1 and P2

%Parameters
%~~~~~~~~~~~~~~~~~~~~~~~~~~~~~~~~
```

```
14 c0=2.9979*10^8; %Speed of light in vacuum
15 lambda=(296:0.2:1206)*10^-9; % Wavelength range of the spectrum, Cause of the
       smoothing-routine, the lambda should be larger than needed
16 W=2*pi*c0./(lambda); % Vector of the angular frequencies of the incomming beam
17 n_Glas=1.33; % Refractiveindex and thickness of the glass substrate
18 d_Glas=2e-4;
19 Cpl=6; % Number of double layers of P1 and P2
20 d_P1=110*10^-9; % Thickness of the Polymer layers P1 and P2, of a (P1 P2)Cpl P1
       system on a glass substrate
21 d_P2=140*10^-9;
22 %~~~~~~~~~~~~~~~~~~~~~~~~~~~~~~~~
23
24 %Calculation of the spectrum
25 %~~~~~~~~~~~~~~~~~~~~~~~~~~~~~~~~
26 E_Trans=fun_spectrum_DBR(d_P1,d_P2);
27 E_Trans=fun_spectrometer_smoothing(E_Trans,lambda);
28 %~~~~~~~~~~~~~~~~~~~~~~~~~~~~~~~~
29
30 %Visualization of the spectrum
31 %~~~~~~~~~~~~~~~~~~~~~~~~~~~~~~~~
32 figure(1)
33 hold on
34     box on
35     plot(lambda*10^9,E_Trans,'color',[0 0 0.8],'linewidth',2)
36     axis([300 1200 0 1])
37     ylabel('Transmission')
38     xlabel('\lambda (nm)')
39     title(['Calculated spectrum of a (P1 P2)',num2str(Cpl),' P1 DBR system']);
40 hold off
41 set(gcf, 'PaperUnits', 'centimeters');
42 set(gcf, 'PaperSize', [15 12]);
43 print('-dpdf','Spectrum');
44 %~~~~~~~~~~~~~~~~~~~~~~~~~~~~~~~~
```

fun_spectrum_DBR

The function calculates a scaled transmission spectrum to the input parameter of layer thicknesses. At line 16 a for-loop starts to calculate the transfer matrix and the transmission for each ω. The refractive index for the two materials is implemented next. In the example the dispersion relation n(ω) is a constant, but in this study the dispersion relation is taken out of the ellipsometry data. The transfer matrices differs for TM and TE polarized light.

At line 23 we indicate to calculate a spectrum for both. From line 30 to 40 the transfer matrices are calculated and assembled. *MairP1* is the transfer matrix from the surface between air and the polymer *P1*. The matrix *MP2P1* is the transfer matrix for light propagating from polymer *P2* into polymer *P1*. The multiplication of all matrices needs to be done with caution. From line 43 till 54 the electric field of reflected and transmitted beam is calculated with equation 2.30 and 2.37. The Intensity of the combined TE and TM polarized transmission is calculated in line 61. This is the spectrum.

```
1  function spectrum=fun_spectrum_DBR(dP1,dP2)
2  % Calculation of a transmission spectrum of a Distributed Bragg Reflector
3
4  % Input: dP1 and dP2: thickness of the Polymer1 and the Polymer2 of a
5  % (Polymer1 Polymer2)Cpl Polymer1 - system on a glass substrate
6  % Output: scaled transmission spectrum
7
8  global c0 W n_Glas d_Glas Cpl
9  %Global Parameters:
10 %c0: Speed of light
11 %W: Vector of the angular frequencies of the incomming beam
12 %n_Glas: Refractive index of the glass substrate
13 %d_Glas: Thickness of the glass substrate
14 %Cpl: Number of double layers of P1 and P2
15
16 for g=1:length(W)
17     w=W(g);
18     nP1=2; % nPS_lambda(w_lambda(w)*10^9); %If the Dispersion relation n(w) is
           available, implement it here
19     nP2=1; % nCA_lambda(w_lambda(w)*10^9);
20
21     %We have an unpolarized light: we need to calc a spectrum for both
22     %polarities and combine them later
23     for pol=1:2
24         if pol==1
25             Polarisation='TM';
26         else
27             Polarisation='TE';
28         end
29
30         %Calculation and assembling the transfer matrix
31         %~~~~~~~~~~~~~~~~~~~~~~~~~~~~~~~~
32         MairP1 = fun_transfer_matrix(w,1,nP1,1e-8,Polarisation);
```

```
        MON = MairP1;
        MP2P1= fun_transfer_matrix(w,nP2,nP1,dP2,Polarisation);
        MP1P2= fun_transfer_matrix(w,nP1,nP2,dP1,Polarisation);
        MON  = (MP2P1*MP1P2)^(Cpl)*MON;
        MP1glas = fun_transfer_matrix(w,nP1,n_Glas,dP1,Polarisation);
        Mglasair= fun_transfer_matrix(w,n_Glas,1,d_Glas,Polarisation);
        MON = Mglasair*MP1glas*MON;
        %~~~~~~~~~~~~~~~~~~~~~~~~~~~~~~~~

        if pol==1
            MON_TM = MON;
            %Calculation of the Refl. and Trans. of 'TM'
            %~~~~~~~~~~~~~~~~~~~~~~~~~~~~~~~~
            Refl_TM(g) = -MON_TM(2,1)/MON_TM(2,2);
            Trans_TM(g)= ((MON_TM(1,1)*MON_TM(2,2)-MON_TM(1,2)*MON_TM(2,1))/MON_TM
                (2,2));
            %~~~~~~~~~~~~~~~~~~~~~~~~~~~~~~~~
        else
            %Calculation of the Refl. and Trans. of 'TE'
            %~~~~~~~~~~~~~~~~~~~~~~~~~~~~~~~~
            MON_TE = MON;
            Refl_TE(g) = -MON_TE(2,1)/MON_TE(2,2);
            Trans_TE(g)= ((MON_TE(1,1)*MON_TE(2,2)-MON_TE(1,2)*MON_TE(2,1))/MON_TE
                (2,2));
            %~~~~~~~~~~~~~~~~~~~~~~~~~~~~~~~~
        end
    end
end
% Combining the 'TM' and the 'TE' polarisation
%~~~~~~~~~~~~~~~~~~~~~~~~~~~~~~~~
E_Trans = sqrt((Trans_TE.*conj(Trans_TE)).^2 + (Trans_TM.*conj(Trans_TM)).^2)/sqrt
    (2);
E_Refl  = sqrt((Refl_TE.*conj(Refl_TE)).^2 + (Refl_TM.*conj(Refl_TM)).^2)/sqrt(2);
%~~~~~~~~~~~~~~~~~~~~~~~~~~~~~~~~

spectrum=E_Trans; %The output is the transmission spectrum, the reflection
    spectrum can be chosen likewise
```

fun_transfer_matrix

The fun_transfer_matrix calculates the transfer matrix (see 2.30 and 2.37) for the transverse electric or the transverse magnetic polarized beam striking at interface of two different media. The parameters are described within the code.

```
function Mj1j2=fun_transfer_matrix(w,n1,n2,d,Polarisation,alpha)
% Calculation of the transfer maxtrix Mj1j2
% j1 indicates the layer the beam comes from, and j2 the layer the beam
% penetrates into
% Parameters:
% w: angular frequency of the incomming beam
% n1,n2: reflective index of the two layers
% d: thickness of the layer the beam comes from
% Polarisation: 'TE': transverse electric or 'TM': transverse magnetic
% oriented beam
% alpha: angle of incident (not tested yet)

global c0

%Implementation of an angle dependency (not yet tested)
%~~~~~~~~~~~~~~~~~~~~~~~~~~~~~~~~
if nargin<6
    kx=0;
else
    kx=sin(alpha*pi/180)*w;
end
%~~~~~~~~~~~~~~~~~~~~~~~~~~~~~~~~

%Dielectricfunction: e1, e2
%Speed of light in the Materials: c1, c2
%kz-component of k-vector of the beam
%~~~~~~~~~~~~~~~~~~~~~~~~~~~~~~~~
e1=n1.^2; % n(lambda)^2=chi(lambda)*epsilon(lambda); chi=0
e2=n2.^2;
c1=c0/n1;
c2=c0/n2;
k1=sqrt(w^2*e1-kx.^2)/c0; % w^2*e-vec(k)^2=0 -> kz=sqrt(w^2 e-kx^2) and /c0
k2=sqrt(w^2*e2-kx.^2)/c0;
%~~~~~~~~~~~~~~~~~~~~~~~~~~~~~~~~

%Calculation of the transfer matrix
```

```
%~~~~~~~~~~~~~~~~~~~~~~~~~~~~~~~~
 if Polarisation == 'TE'
    Mj1j2=1/2*[...
        (1+k1./k2).*exp(i*k1*d) , (1-k1./k2).*exp(-i*k1*d) ;...
        (1-k1./k2).*exp(i*k1*d) , (1+k1./k2).*exp(-i*k1*d)]; %#ok<IJCL>
 elseif Polarisation == 'TM'
     Mj1j2=1/2*[...
        (1+k1./k2*e2/e1).*exp(i*k1*d) , (1-k1./k2*e2/e1).*exp(-i*k1*d) ;...
        (1-k1./k2*e2/e1).*exp(i*k1*d) , (1+k1./k2*e2/e1).*exp(-i*k1*d)]; %#ok<IJCL
            >
 end
 %Calculation of the transfer matrix
```

fun_spectrometer_smoothing

The function smooths a spectrum. The intensity at a wavelength gets modified with its neighbors intensities weighted with a Gaussian distribution function.

```
function Out=fun_spectrometer_smoothing(Spectrum,lambda)
% Smoothing of a calculated spectrum

% A point in the spectrum-vector gets smoothened by the neighbours in the
% double sigma region weighted with a Gaussian distribution function with
% a sigma of 1nm (can be changed in the parameter: Spectrometer_Error_half)

%Parameters:
%~~~~~~~~~~~~~~~~~~~~~~~~~~~~~~~~
Spectrometer_Error=1; %Sigma of the Gaussian function, or error of the
    spectrometer (nm)
Sigma_Double=2; %Region of the implemented neighbours
Stepwidth=(lambda(2)-lambda(1))*10^9;
%~~~~~~~~~~~~~~~~~~~~~~~~~~~~~~~~

x=0:Stepwidth:Spectrometer_Error/2*Sigma_Double;
Gauss=exp(-1/2*(x./Spectrometer_Error/2).^2);
Faktor=Gauss./(sum(Gauss)+sum(Gauss(2:end)));
Out=Spectrum.*Faktor(1);
Steps=length(x)-1;

for step=1:Steps
    Out(1+step:end-step)=...
        Out(1+step:end-step)+...
```

```
24          Faktor(step+1)*Spectrum(1:end-2*step)+...
25          Faktor(step+1)*Spectrum(1+2*step:end);
26  end
```

Bibliography

[1] L. Rayleigh: XVII. On the maintenance of vibrations by forces of double frequency, and on the propagation of waves through a medium endowed with a periodic structure. *Philosophical Magazine Series 5* **24**(147) (1887), 145–159.

[2] E. Yablonovitch: Inhibited Spontaneous Emission in Solid-State Physics and Electronics. *Phys. Rev. Lett.* **58** (20 1987), 2059–2062. DOI: 10.1103/PhysRevLett.58.2059.

[3] S. John: Strong localization of photons in certain disordered dielectric superlattices. *Physical Review Letters* **58**(23) (1987), 2486–2489.

[4] J. D. Joannopoulos: *Photonic crystals: Molding the flow of light*. 2nd ed. Princeton and NJ: Princeton Univ. Press, 2008, p. 51.

[5] L. Berti et al.: Spectroscopic Investigation of Artificial Opals Infiltrated with a Heteroaromatic Quadrupolar Dye. *The Journal of Physical Chemistry C* **114**(6) (2010), 2403–2413.

[6] M. Barth, A. Gruber, and F. Cichos: Spectral and angular redistribution of photoluminescence near a photonic stop band. *Physical Review B* **72**(8) (2005).

[7] G. Lozano, S. Colodrero, O. Caulier, M. E. Calvo, and H. Miguez: Theoretical Analysis of the Performance of One-Dimensional Photonic Crystal-Based Dye-Sensitized Solar Cells. *The Journal of Physical Chemistry C* **114**(8) (2010), 3681–3687.

[8] A. S. Marko Lončar and Y. Qiu: Photonic crystal laser sources for chemical detection. *Applied Physics Letters*(82) (2003), 4648.

[9] J. J. Wierer, A. David, and M. M. Megens: III-nitride photonic-crystal light-emitting diodes with high extraction efficiency. *Nature Photonics* **3**(3) (2009), 163–169.

[10] Scotognella F. et al.: One Dimensional Polymeric Organic Photonic Crystals for DFB Lasers (2008).

[11] L. Frezza, M. Patrini, M. Liscidini, and D. Comoretto: Directional Enhancement of Spontaneous Emission in Polymer Flexible Microcavities. *The Journal of Physical Chemistry C* **115**(40) (2011), 19939–19946.

[12] A. Urbas, M. Maldovan, P. DeRege, and E. Thomas: Bicontinuous Cubic Block Copolymer Photonic Crystals. *Advanced Materials* **14**(24) (2002), 1850–1853.

[13] A. A. Zakhidov: Carbon Structures with Three-Dimensional Periodicity at Optical Wavelengths. *Science* **282**(5390) (1998), 897–901.

[14] F. Quaranta, A. Valentini, F. R. Rizzi, and G. Casamassima: Dual-ion-beam sputter deposition of ZnO films. *Journal of Applied Physics* **74**(1) (1993), 244.

[15] J. W. Perry et al. *Nature* **398**(6722) (1999), 51–54.

[16] M. Sandrock et al.: A widely tunable refractive index in a nanolayered photonic material. *Applied Physics Letters* **84**(18) (2004), 3621.

[17] M. Kimura, K. Okahara, and T. Miyamoto: Tunable multilayer-film distributed-Bragg-reflector filter. *Journal of Applied Physics* **50**(3) (1979), 1222.

[18] O. Sánchez-Sobrado, M. E. Calvo, and H. Míguez: Versatility and multifunctionality of highly reflecting Bragg mirrors based on nanoparticle multilayers. *Journal of Materials Chemistry* **20**(38) (2010), 8240.

[19] J. Israelachvili: Thin film studies using multiple-beam interferometry. *Journal of Colloid and Interface Science* **44**(2) (1973), 259–272.

[20] H. Arwin and D. Aspnes: Unambiguous determination of thickness and dielectric function of thin films by spectroscopic ellipsometry. *Thin Solid Films* **113**(2) (1984), 101–113.

[21] F. Bloch: Über die Quantenmechanik der Elektronen in Kristallgittern. German. *Zeitschrift fuer Physik* **52**(7-8) (1929), 555–600. DOI: 10.1007/BF01339455.

[22] Sormann, H. and Schachinger, E.: Theoretische Festkörperphysik 515.468. 2009.

[23] M. Skorobogatiy and J. Yang: *Fundamentals of photonic crystal guiding*. Cambridge, UK, and New York: Cambridge University Press, 2009.

[24] M. Kolle, B. Zheng, N. Gibbons, J. Baumberg, and U. Steiner: Stretch-tuneable dielectric mirrors and optical microcavities. *Optics Express*(18) (2010), 4356–4364.

[25] Dorda, A.: 1-D photonische Kristalle. Graz, 2009.

[26] A. Ciferri and A. Perico: *Ionic interactions in natural and synthetic macromolecules*. Hoboken and NJ: Wiley, 2012.

[27] P. Florian, F. Fayon, and D. Massiot: 2J Si−O−Si Scalar Spin−Spin Coupling in the Solid State: Crystalline and Glassy Wollastonite CaSiO 3. *The Journal of Physical Chemistry C* **113**(6) (2009), 2562–2572.

[28] C. J. R. Sheppard: Approximate calculation of the reflection coefficient from a stratified medium. *Pure and Applied Optics: Journal of the European Optical Society Part A* **4**(5) (1995), 665–669.

[29] E. M. Purcell: Spontaneous Emission Probabilities at Radio Frequenties. *Physical Review*(69) (1946).

[30] G. Canazza et al.: Lasing from all-polymer microcavities. *Laser Physics Letters* **11**(3) (2014), 035804.

[31] A. Neuhold et al.: X-ray based tools for the investigation of buried interfaces in organic electronic devices. *Organic Electronics* **14**(2) (2013), 479–487.

[32] O. Werzer, K. Matoy, P. Strohriegl, and R. Resel: Temperature treatment of semiconducting polymers: An X-ray reflectivity study. *Thin Solid Films* **515**(14) (2007), 5601–5605.

[33] S. Fladischer et al.: Diffusion of Ag into Organic Semiconducting Materials: A Combined Analytical Study Using Transmission Electron Microscopy and X-ray Reflectivity. *ACS Applied Materials & Interfaces* **4**(10) (2012), 5608–5612.

[34] A. Neuhold et al.: Structure and morphology of an organic/inorganic multilayer stack: An x-ray reflectivity study. *Journal of Applied Physics* **110**(11) (2011), 114911.

[35] J. Daillant and A. Gibaud: *X-ray and neutron reflectivity: Principles and applications.* 2nd ed. Vol. 770. Lecture notes in physics. Berlin and London: Springer, 2009.

[36] M. Birkholz, P. F. Fewster, and C. Genzel: *Thin film analysis by X-ray scattering.* Weinheim and [Chichester: Wiley-VCH and John Wiley, distributor], 2006.

[37] G. Porod: Die Röntgenkleinwinkelstreuung von dichtgepackten kolloiden Systemen. German. *Kolloid-Zeitschrift* **124**(2) (1951), 83–114. DOI: 10.1007/BF01512792.

[38] L. Névot and P. Croce: Caractérisation des surfaces par réflexion rasante de rayons X. Application à l'étude du polissage de quelques verres silicates. *Revue de Physique Appliquée* **15**(3) (1980), 761–779.

[39] L. Parratt: Surface Studies of Solids by Total Reflection of X-Rays. *Physical Review* **95**(2) (1954), 359–369.

[40] H. Kiessig: Interferenz von Röntgenstrahlen an dünnen Schichten. *Annalen der Physik* **402**(7) (1931), 769–788.

[41] A. G. Frank Schreiber: X-Ray and Neutron Reflectivity forthe Investigation of Thin Films.

[42] H. Flesch, S. Mathijssen, F. Gholamrezaie, A. Moser, and A. Neuhold: Microstructure and Phase Behavior of a Quinquethiophene-Based Self-Assembled Monolayer as a Function of Temperature (2011).

[43] G. Binnig, C. F. Quate, and C. Gerber: Atomic Force Microscope. *Phys. Rev. Lett.* **56** (9 1986), 930–933. DOI: 10.1103/PhysRevLett.56.930.

[44] Olympus: Micro Cantilever OMCL/BL Series.

[45] D. Brewster: On the Laws Which Regulate the Polarisation of Light by Reflexion from Transparent Bodies. *Philosophical Transactions of the Royal Society of London* **105** (1815), 125–59.

[46] E. Klett: Photometria sive de mensura et gradibus luminis, colorum et umbrae. sumptibus viduae Eberhardi Klett (1760).

[47] F. Melde: Über Absorption des Lichts bei farbigen Flüssigkeiten. *Annalen der Physik und Chemie* **202**(10) (1865), 264–285.

[48] D.-H. Ko et al.: Photonic Crystal Geometry for Organic Solar Cells. *Nano Letters* **9**(7) (2009), 2742–2746.

[49] Sigma-Aldrich: Sicherheitsdatenblatt: Polystyrene. *Produktnummer: 430102* (2012).

[50] Sigma-Aldrich: Sicherheitsdatenblatt: Cellulose acetate. *Produktnummer: 22194* (2012).

[51] I. Polyscience: Technical Data Sheet 263: Poly(N-vinylcarbazole) (PVK) (2007).

[52] I. A. D. Source: Conjugated Polymer for Organic Solar Cells and Sensors: ADS508PT (2007).

[53] K. Sparnacci et al.: Preparation, Properties, and Self-Assembly Behavior of PTFE-Based Core-Shell Nanospheres. *Journal of Nanomaterials* **2012**(3) (2012), 1–15.

[54] V. Morandi, F. Marabelli, V. Amendola, M. Meneghetti, and D. Comoretto: Colloidal Photonic Crystals Doped with Gold Nanoparticles: Spectroscopy and Optical Switching Properties. *Advanced Functional Materials* **17**(15) (2007), 2779–2786.

[55] D. P. Puzzo et al.: Color from colorless nanomaterials: Bragg reflectors made of nanoparticles. *Journal of Materials Chemistry* **19**(21) (2009), 3500.

[56] F. Fleischhaker et al.: Photochemically and Thermally Tunable Planar Defects in Colloidal Photonic Crystals. *Journal of the American Chemical Society* **127**(26) (2005), 9318–9319.

[57] W.-Y. Wong et al.: Metallated conjugated polymers as a new avenue towards high-efficiency polymer solar cells. *Nature Materials* **6**(7) (2007), 521–527.

[58] W. R. Salaneck: *Conjugated polymer and molecular interfaces: Science and technology for photonic and optoelectronic applications*. New York: M. Dekker, 2002.

[59] O. Olabisi, L. M. Robeson, and M. T. Shaw: *Polymer-polymer miscibility*. New York: Academic Press, 1979.

[60] K. Unger et al.: Distributed Bragg Reflectors: Morphology of Cellulose Acetate and Polystyrene Multilayers. *Proceedings of ICTON 2014* (forthcoming).